NANYANG TECHNOLOGICAL UNIVERSITY

METALLIC GLASSES: THERMAL, MECHANICAL PROPERTIES AND THEIR CORRELATION

PANG JIANJUN

SCHOOL OF MECHANICAL AND AEROSPACE ENGINEERING

2012

METALLIC GLASSES: THERMAL, MECHANICAL PROPERTIES AND THEIR CORRELATION

Pang Jianjun

School of Mechanical and Aerospace Engineering

A thesis submitted to the Nanyang Technological University
in fulfilment of the requirement for the degree of
Doctor of Philosophy

2012

Acknowledgements

First and foremost, I would like to express deep gratitude to my supervisor, Associate Professor Tan Ming Jen, for offering me the opportunity to work with him, for giving me the freedom to explore the present research field, for recommending me the people from different scientific areas, and, most of all, for constantly understanding and encouraging me through the years. Deep gratitude also goes to Professor Liew Kim Meow from the City University of Hong Kong, who has provided me the opportunity to visit his group and the guidance in the computational part of the thesis.

I gratefully thank Associate Professor Christopher Shearwood for his help in showing me the facilities of the clean room and his advice on part of my thesis work. Great thanks also go to Associate Professor Sridhar Idapalapati and Assistant Professor Wong Chee How for their useful discussion on my initial work.

I am thankful for the collaboration with Ms. Liu Yuchan from the Singapore Institute of Manufacturing Technology, who has provided me the access to the high-temperature nanoindentation instrument.

Many thanks go to the technical staff of the School who have lent their hands in technical supports, especially Mr. Lew Sui Leung, Ms. Yong Mei Yoke, Mr. Leong Kwok Phui, Mr. Chang Set Chiang, Ms. Yeong Peng Neo, Ms. Chow Shiau Kee, and Ms. Koh Joo Luang from Materials Lab; Mr. Pek Soo Siong, Mr. Hoong Sin Poh, Mr. Nordin Bin Abdul Kassim, and Mr. Ho Kar Kiat from Micromachines Lab 1; Mr. Tan Boon Hwee, and Mr. Lim Kean Chye from Precision Engineering Lab.

I sincerely appreciate the moments, the help and the friendship from the many past and present members of the Tan Research Group, especially Dr. Wang Yongsheng, Dr. Yang Hongwang, Dr. Fu xiaoling, Dr. Zhang Jie, Yahya Motemani Sharabiani, Liao Jinzhi, and Liu Jun.

Last but not least, very special thanks go to my parents, my sister, and my wife for their constant support, love and encouragement.

Table of Contents

Summary

To understand the physical factors determining the material properties is of essential importance for the synthesis of new compositions with favorable characteristics. So far the relationship between the electronic structure and the physical properties of metallic glasses (MGs) has not been adequately studied. This project aims to understand and demonstrate the correlation between thermal and mechanical properties of MGs from the viewpoint of valence electron density (VED) in order to provide guidelines for the future design of new systems with desired plasticity. Initially, the thermal and mechanical properties of MGs are explored.

A number of MGs were prepared and their amorphous structures were verified by experimental and computational methods. The X-ray diffraction (XRD) and electron diffraction both indicate that there indeed exist short-to-medium-range orders in the amorphous structure. Molecular dynamics simulation confirms the existence of such orders, and also suggests that the amorphous structure consists of diverse polyhedral types, among which some types are dominant (e.g., icosahedral and bcc clusters in $Ti_{50}Cu_{50}$). These clusters form a five-fold symmetry in the medium range distance. The thermal properties of MGs were studied by continuous differential scanning calorimetry (DSC). For each glassy alloy, the glass transition temperature, and the width of the glass transition region exhibit dependence on heating rate, i.e., they increase with an increase in heating rate; in contrast, the heat enthalpy at crystallization appears to be independent of heating rate, except for the Zr-based sample likely due to its unique crystallization processes. Nevertheless, the larger glass transition temperatures generally correspond to the larger heat enthalpy and the wider glass transition region.

Instrumented nanoindentation was performed on MGs to characterize the mechanical properties, in particular at various loading rates and indent sizes. For the La- and Zr-based specimens, the pile-up height and the shear band zone size imaged by atomic force microscopy (AFM) were found to be independent of loading rates, in good agreement with the absence of loading rate dependence of mechanical properties.

However, they both show the indentation size effect (ISE), specifically, the hardness is enhanced at smaller indents. In contrast, for $Cu_{49.3}Zr_{50.7}$, the mechanical properties are influenced by the loading rate, i.e., they increase as the loading rate increases up to a critical value. However, it does not have an ISE. The degree of structural relaxation, which can be represented by the relaxation time spectrum, accounts for the mechanical response of MGs to the loading rates. This spectrum was derived from the nanoindentation creep, and reveals that the Zr-based specimen is in a more relaxed state than $Cu_{49.3}Zr_{50.7}$ because the former has lower peak intensity than the latter. In other words, the Zr-based specimen is less viscoelastic than $Cu_{49.3}Zr_{50.7}$.

Based on the experimental work, a proportional relationship between thermal and mechanical properties has been identified, which can be determined by the valence electron density—the number of valence electrons per atomic volume. Furthermore, the plasticity or the Poisson’s ratio is found to be dependent on VED as well. For each type of MGs, the Poisson’s ratio commonly decreases as VED increases. From the energy dissipation viewpoint, the lower shear-transformation-zone (STZ) activation energy implies the higher ductility because STZs with lower activation energy are able to convert deformation work more efficiently into the configurational energy rather than heat. The smaller VED implies a weaker atomic bonding and also easier atomic motion for STZ activation and crystallization. Therefore, the VED-related plasticity suggests a simple method for designing ductile MGs.

List of Figures

List of Tables

List of Abbreviations

AFM	Atomic force microscopy
BMG	Bulk metallic glass
BP	Bipolar plate
CN	Coordination number
CSM	Continuous stiffness measurement
CSRO	Chemical short range order
DMS	Dynamic mechanical spectroscopy
DRP	Dense random packing
DSC	Differential scanning calorimetry
ECP	Efficient cluster packing
EDS/EDX	Energy dispersive X-ray spectrometry
fcc	Face-centered cubic
FVM	Free volume model
GEAM	General embedded-atom method
GFA	Glass forming ability
GSRO	Geometrical short range order
hcp	Hexagonal close-packed
ISE	Indentation size effect
MCT	Mode-coupling theory
MDS	Molecular dynamics simulation
MG	Metallic glass
NM	normal method
PEL	Potential energy landscape
PSR	Proportional specimen resistance
RDF	Radial distribution function
RF	Radio-frequency
SAED	Selected-area electron diffraction
SB	Shear band
SEM	Scanning electron microscopy
SGP	Strain gradient plasticity
SLR	Supercooled liquid region

SR	Structural relaxation
SRO	Short range order
STZ	Shear transformation zone
TEM	Transmission electron microscopy
VED	Valence electron density
VFT	Vogel–Fulcher–Tamman equation
VTA	Voronoi tessellation analysis
XRD	X-ray diffraction

List of Symbols

A_p	Projected contact area
B	Bulk modulus
C_e	Eutectic composition
C_er	Reduced eutectic composition
C_s	Minimum hypoeutectic compistion
d	Valence electron density
e_i	Number of valence electrons
E	Young’s modulus for test material
E_a	Activation energy
E_i	Young’s modulus for diamond
E_r	Reduced Young’s modulus
E_tot	Total energy
f	Atomic scattering factor
f_i	Interatomic force acted on atom i
f_ij	Two body force between atoms i and j
F_i	Embedding energy
g	Radial distribution function
G	Gibbs free energy or shear modulus
G_{0T}	Shear modulus at zero stress
h	Indentation depth
h^*	Characteristic material length scale
h_c	Indentation contact depth
h_m	Maximum indentation depth
h_s	Displacement of surface deflection during indentation
H	Hardness
H_0	Hardness in the absence of strain gradient
I_hom	Homogeneous nucleation rate
I_heter	Heterogeneous nucleation rate
I_r	X-ray scattered intensity due to a particular interatomic distance r
$\mathbf{k}$	Scattering vector
k_B	Boltzman constant

L	Relaxation time spectrum
m	Atomic weight or fragility index
m_{cs}	Fragility index at the onset of glass transition
m_{ce}	Fragility index at the end of glass transition
m_H	Strain rate sensitivity
n	Average number density
n_i	Number of *i*-edged faces of a Voronoi cell
N	Number of particles
N_r	Number of atoms at a space separation r
p_i	Local pressure of atom i
p_i^α	α component of momentum of atom i
P	External pressure or indentation load
q	Scattering factor
Q	Configurational partition function or activation energy for anelastic recovery
$\vec{\mathrm{r}}$	Unit displacement vector
r_e	Equilibrium spacing between nearest atoms
r_i	Position of atom i
$\dot{r}_\mathrm{i}$	Velocity of atom i
$\ddot{r}_\mathrm{i}$	Acceleration of atom i
r_ij	Space interval between atoms i and j
r_i^α	α component of position of atom i
R	Ideal gas constant
R_Bragg	Radius of the first coordination shell calculated with Bragg equation
R_c	Critical cooling rate or covalent bonding length
R_h	Heating rate
R_m	Metallic bonding length
R_s	Average radius of the first coordination shell
S	Structure factor, Surface area or contact stiffness upon removal of indenation load
S_c	Configurational entropy
t	Time
T	Temperature

T_0	Temperature where the two phases of the same composition have an equal free energy
$T_0(C_e)$	Temperature T_0 at the composition C_e
T_{0r}	A parameter determining glass-forming ability
T_e	Eutectic temperature
T_{eff}	Effective disorder temperature
T_g	Glass transition temperature
T_{gs}	Glass transition temperature at onset point
T_{ge}	Glass transition temperature at end point
T_x	Crystallization temperature at onset point
T_p	Crystallization temperature at peak
T_L	Liquidus temperature
T_m	Melting temperature
T_{gr}	Reduced glass transition temperature
T_{Lr}	Reduced liquidus temperature
T_L^0	Ideal solution liquidus temperature
T_L^{mix}	Melting point of mixtures
T_m^A, T_m^B	Melting points of pure elements A and B
V	Volume of N particles or indentation volume
W	Activation energy of an STZ
W_{0Z}	Activation energy of an STZ at an unsheared state
W_T	Debye-Waller factor
x_i	Concentration of element i
Z_i, Z_j	Total coordination number of atom i or j
Z_{ij}, Z_{ji}	Coordination number of atom j or i around atom i or j
Z_{ij}^*	Partial coordination number in the limit of complete chemical disorder
$<Z>$	Average coordination number
ΔC_p	Heat capacity difference
ΔG_{xL}	Molar free energy difference between the liquid and equilibrium crystalline alloy
ΔH_f^A	Heat of fusion of element A
ΔH_m	Molar heat of fusion
ΔH_v	Molar heat of vaporization

ΔS_{m}	Entropy of fusion
Δt	Time step
ΔT	Supercooling temperature increment
ΔT_g	Width of glass transition region
ΔT_x	Supercooled liquid region
ΔT^*	Departure of the alloy liquidus temperature from that of mixtures liquidus temperature
α, β	Cartesian components
ε	Strain or geometrical correction factor
ε_p	Pure plastic strain
$\dot{\varepsilon}$	Strain rate
ϕ	Potential energy
φ_{j}	Electron density of atom *i* due to atom *j*
γ_c	Critical shear strain
γ_{s}	Interface energy
η_{ij}	Short range order coefficient
υ	Viscosity
ν	Poisson’s ratio for test material
ν_i	Poisson’s ratio for diamond
ν_Z	Number of molecules in an STZ
ω	Composition departure in the nearest neighbor shell from the average
θ	Scattering angle
ρ_{i}	Electron density of atom *i*
σ	Stress
σ_y	Yield strength
ξ	Temperature-dependent correction factor
Θ	Debye temperature
Ω	Total Voronoi volume
Ω_i	Voronoi volume of atom *i* or atomic volume of pure element *i*
Ω_m	Volume per molecule
Ω_Z	Volume of an STZ
$\hbar$	Reduced Planck constant

τ	Relaxation time or shear stress
τ_c	Critical shear stress
δ	Shear band zone size or plastic zone size in Johnson’s cavity model
ϑ	Total energy dissipation rate per unit STZ volume
ϑ_S	Energy dissipation rate for configurational disorder of STZs

Chapter 1 Introduction

1.1 Background

Metallic glasses (MGs), also named as amorphous alloys, are a member of glass family mainly composed of metallic elements and contain a random structure entirely different from crystalline periodicity. Such unique structrue is where they are the most attractive and gives rise to the distinct structural and functional properties.

MGs were discovered first by physicists who were into the condensation of thin films at low temperatures [1]. Naturally, coming with the discovery was a discussion whether they are amorphous or microcrystalline. Many efforts have been devoted to understanding the structure by experimental and computational techniques during the past years. It is realized now that although they exhibit a random structural feature in a long range distance, MGs exactly possess short-to-medium range order which determine their unique properties. This short-to-medium range order differs from one material system to another and ignites the worldwide research interest.

Besides the fundamental interest, MGs were also appreciated due to possible technological applications based on their thermal, mechanical, chemical, electrical and magnetic properties. These properties were soon realized as unusual after the discovery of the first MG Au-Si and a lot of research was done to investigate them in 1970s and 1980s [2, 3]. The extensive use of MGs is hindered by their thermodynamical metastability and global brittleness. The metastability results from the higher energy configuration as compared to the stable crystalline structure, and the brittleness is due to the plastic deformation constrained in an extremely thin region (at most tens of nanometers). To date, much attention has been concentrated to develop new systems with a combination of good thermal and mechanical properties.

As the crystalline defects do not exist in the amorphous structure, the thermal and mechanical properties are thought to be directly related to the atomic bonds. In addition, the microscopic processes in the annealing-induced structural relaxation and mechanical deformation are similar, specifically, they are governed by the thermally-activated movement of an elementary unit. Therefore, the thermal and mechanical properties are regarded as correlated. A large amount of work has been done to reveal the connection between these properties. However, the relationship between the properties and atomic/electronic structures has not yet been fully studied [4]. In this respect, it could be interesting to explore the relationship from the perspective of atomic/electronic structure.

1.2 Objective and scope

MGs due to their unique structure and properties attract increasing attention with advancement of both experimental and computational techniques. Since so far a huge variety of MGs have been developed, the focus of research interest is to understand the structure-to-property relationship so as to support the designing of new MGs.

The objective of this project is to demonstrate and understand the correlation between the thermal and mechanical properties from the viewpoint of valence electron density with the hope to provide a guideline for the design of new amorphous alloys with desirable plasticity. Before looking at the relationship, it is necessary to systematically investigate the thermal and mechanical properties of MGs.

Chapter 1 presents a background introduction to MGs followed by objective and scope of the present study.

Chapter 2 presents a pertinent literature review on atomic structure, glass-forming principles, mechanical behaviors and applications of MGs so as that it can be figured out where to extend the work.

Chapter 3 demonstrates in detail the amorphous structures and thermal properties of nine MGs obtained or prepared in this study.

Chapter 4 describes the mechanical properties of MGs at various loading conditions such as loading rate, indentation depth and temperature.

Chapter 5 presents and explains the correlation between the thermal and mechanical properties according to the results in this work as well as in the literature.

Chapter 6 and **7** respectively conclude the present work and propose the problems to be investigated in the future.

Chapter 2 Literature Review

2.1 Introduction

MGs are relatively new to the family of materials and attract increasing attention due to their unique structural and functional properties. Underlying these properties is the atomic structure, much different from the translational symmetry in crystals. Understanding of the atomic structure of MGs is necessary for understanding of their unique properties. In the past decades, many efforts have been devoted to investigating the properties and atomic structure of MGs.

This chapter is organized in the following manner: Section 2.2 presents an overview on atomic structure. Sections 2.3 and 2.4 give an introduction to glass-forming principles and liquid-to-glass transition process by which conditions/parameters for glass formers can be identified. Section 2.5 details the deformation mechanisms of MGs by considering the various effects such as specimen size, temperature and strain rate. Section 2.6 summarizes the applications of MGs based on their mechanical, magnetic and chemical properties.

2.2 Atomic structure

Solid materials are primary building blocks of human’s living world due to their substantial physical properties which could be attributed to the diverse atomic or molecular configurations, either crystalline or amorphous or both. Thus, it is of great importance for design of new materials to see how atoms or molecules assemble together. From a theoretical viewpoint, given an accurate and adequate knowledge of the interaction potential function among N particles of a system, the configurational partition function can be calculated:

$$Q = \frac{1}{V^N N!} \int \cdots \int \exp\left(-\phi / k_\mathrm{B} T\right) \mathrm{d}V_1 \cdots \mathrm{d}V_N \tag{2.1}$$

where V is the volume of N particles, ϕ is the potential function, and $\mathrm{d}V_\mathrm{i}$ is an infinitesimal volume of particle *i*. Based on Eq. 2.1, thermodynamic properties of the system, such as Helmholtz energy, the internal energy *etc*., can be evaluated [5]. For a crystalline solid, its structure is well-defined and calculation of Q can be simplified because of lattice symmetry. For a non-crystalline solid, however, the absence of periodic structure renders it impossible to attain the configurational integral. It seems necessary to turn to an alternative method—model building.

It is agreed that amorphous alloys are macroscopically isotropic because of long-range disorder. However, there actually exists anisotropy in these alloy systems [6-8]. It has been known that the physical properties, notably those structure-sensitive properties such as ferromagnetic property can vary from one section of MGs to another. This would be surprising and was attributed in early times to that some of MGs are not amorphous but merely microcrystalline. Later, it was recognized that the anisotropic phenomena are originated from the local atomic environments in the glassy structure. Such atomic environments can be defined by short-range order (SRO) including two types: chemical or compositional short-range order (CSRO) and geometrical or physical short-range order (GSRO). These microscopic features have been observed using computational and experimental techniques [9-11].

CSRO gives an account of the state of mixture of the alloy elements and can be quantified by using the composition departure in the nearest neighbour shell from the average:

$$\omega = 1 - \frac{Z_{\mathrm{ij}}}{\langle Z \rangle x_{\mathrm{j}}} = 1 - \frac{Z_{\mathrm{ji}}}{\langle Z \rangle x_{\mathrm{i}}} \tag{2.2}$$

$$\langle Z \rangle = x_{\mathrm{i}} Z_{\mathrm{i}} + x_{\mathrm{j}} Z_{\mathrm{j}} \tag{2.3}$$

$$Z_{\mathrm{i}} = Z_{\mathrm{ii}} + Z_{\mathrm{ij}} \tag{2.4}$$

where Z_{ij} is the coordination number (CN) of atom *j* around atom *i*, $\langle Z \rangle$ is the average CN, Z_{i} is the total CN of atom *i*, and x_{i} is the concentration of element *i*. $\omega < 0$, $\omega = 0$ and $\omega > 0$ indicates chemical ordering, complete chemical disorder and clustering, respectively. The implicit assumption for Eq. 2.2 is that atomic size effect is excluded, that is, difference in total CN is neglected, resulting in $Z_{\mathrm{i}} = Z_{\mathrm{j}} = \langle Z \rangle$. A more applicable formula for description of CSRO whenever $Z_{\mathrm{i}} \neq Z_{\mathrm{j}}$ can be obtained [12]:

$$\eta_{\mathrm{ij}} = \frac{Z_{\mathrm{ij}}}{Z_{\mathrm{ij}}^{*}} - 1 \tag{2.5}$$

$$Z_{\mathrm{ij}}^{*} = x_{\mathrm{j}} Z_{\mathrm{i}} Z_{\mathrm{j}} \big/ \langle Z \rangle \tag{2.6}$$

where Z_{ij}^{*} is partial CN in the limit of complete chemical disorder. $\eta_{\mathrm{ij}} < 0$ in case of chemical preference for like bonds; $\eta_{\mathrm{ij}} = 0$ in case of complete chemical disorder; and $\eta_{\mathrm{ij}} > 0$ in case of chemical preference for unlike bonds. It is worth noting that these unlike bonds are often observed in TM-metalloid systems due to partially covalent bonding and TM-TM systems due to non-additive pair interaction and believed to be responsible for easy glass forming ability [13].

GSRO, also playing a crucial role in the properties of MGs, describes the geometrical/topological packing of atoms in the nearest neighbor distances. To estimate the stability of such local topological structures, a stress criteria was proposed by Egami *et al* [14]:

$$\sigma_{\mathrm{i}}^{\alpha\beta} = \frac{1}{2\Omega_i} \sum_{\mathrm{j}} f_{\mathrm{ij}}^{\alpha} r_{\mathrm{ij}}^{\beta} \tag{2.7}$$

where σ_{i} is the atomic level stress on atom i, α, β are Cartesian components, Ω_i is the local volume of atom i, f_{ij} and r_{ij} are the two body force and space interval between the ith and jth atoms. It is now known that the stress fluctuation due to thermal fluctuation is atomically localized in amorphous solids and represents the structural fluctuations. In reference [15], the local CN Z_{i} is related to the local pressure p_{i}: the compressed atoms tend to have Z_{i} smaller than the average.

Two concepts of primary importance have been reviewed to facilitate the subsequent introduction of models for MGs. Until now the structure of MGs still remain mysterious. The earlier structural model of a liquid proposed by Bernal [16] was based on the assumption that the system was made of atoms considered as ideal hard spheres. This hypothesis is reasonable from the point of view that the liquid density is about the same as that of the crystal. Such a liquid model was then extended to amorphous alloys by Cohen and Turnbull [17]. The agreement of this model with real systems was later examined [18, 19] and proved good. Despite the successful application, there are still intrinsic limitations preventing its extensive use. The first one is that the assumption of dense random packing (DRP) of hard spheres which are defined by hard potential in model calculation cannot account for the relative intensities of the two components of the split second peak, that is, the intensity of the first subpeak is lower than that of the second subpeak [20]. The second one is that Bernal's idea fails to model many binary MGs, especially metal-metalloid glasses, where the CSRO is significant. At last, Bernal's model cannot explain why the excellent glass-forming alloys often have exceptionally high densities relative to their crystalline counterparts (the density ratio is above 99.5%) [21, 22].

To tackle the first problem, soft potentials [20] are introduced to approximate the interatomic repulsive action, by which the ratio of intensities of the two subpeaks shows relatively good agreement with experimental data. However, they do not reconcile well with binary metal-metalloid alloys. It seems that DRP model sees its inability and a pressing need is to construct a novel model which better represents the real amorphous systems.

In late 1970s, Gaskell [23] proposed a stereochemically defined model based on the principle that the local structure of amorphous solids is always identical to that of crystalline types of the materials. The model was built by non-periodic arrangements of regular trigonal prismatic units (shown in Fig. 2.1) which are frequently found in glasses of transition metal borides, carbides, phosphides and silicides. As a result, there is satisfactory agreement between the experimental and computed data. In spite of the encouraging reproduction, whether this physical model is generally applicable is still under debate because experimental evidence has not yet been conclusive. It should be noted that this model renders an alternative solution to the second problem discussed above.

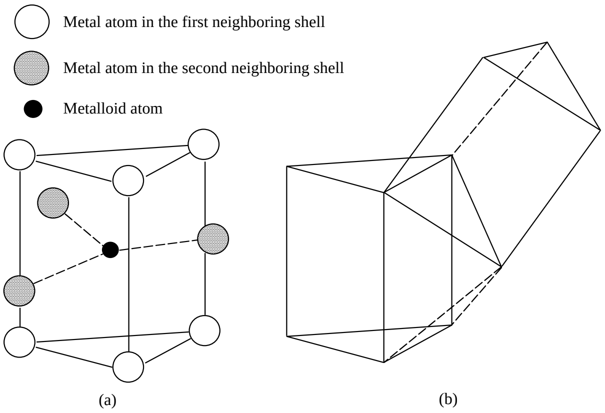

Figure 2.1 (a) Regular trigonal prismatic coordination; (b) Arrangements by edge sharing of units.

A recent model presented by Miracle [24, 25] demonstrates a possible solution to the remaining issue. It is based on the principle of efficient atomic packing and can be constructed at two steps: (1) Efficiently packed solute-centered clusters characterize the local structure; (2) These sphere-like clusters as structural elements fill space efficiently in a face-centered cubic (fcc) or hexagonal close-packed (hcp) forms. The atomic packing fractions of a number of MGs are calculated using this model and commonly vary between DRP (~0.64) and fcc packing (~0.74) [26]. Moreover, the predicted solute-to-solvent ratio shows a very close correlation with the observed values in various MGs. Both these factors state the validity of this model in describing the amorphous configuration. This concept was further applied and corroborated in Al-Y and Al-Y-Ni alloys [27]. However, there still exist discussible points in Miracle's model. Firstly, systems containing small amount of solute (＜20%) were only investigated and solute-solute bonding is excluded. Secondly, only fcc packing of clusters taken into account seems not adequate.

Later, to check if these previous models truly reflect the amorphous structure, a study was carried out using both experimental and computational techniques [28]. The in-depth analysis indicates that MGs often involves as many as several hundred types of coordination polyhedra among which a few types are dominant depending on atomic size ratio and that these polyhedral units are packed as likely as in an icosahedral fivefold form. Also, solute atoms would connect as strings or networks when enriched (＞20%).

So far a number of significant structural models have been reviewed and give us an approximate picture of atomic configurations at the short- and medium-range level. The proposed structural features in MGs are concluded as follows:

(1) MGs are built by dense packing of atoms. They display short-to-medium-range order but no long-range order.

(2) The nearest solute-solvent atoms neighbor themselves in an ordered way similar to that in competing crystalline phases, which is determined by atomic size ratio and concentration as well. *Cluster* is assigned as the name of such a structural unit. There are a huge number of polyhedral cluster types in real MGs among which certain types occur with large portions.

(3) When solute concentration increases, solute atoms might either occupy vacant sites among densely packed clusters, or form bonds encaged in clusters. Reaching a threshold fraction, solute atoms make network-like connection.

(4) These clusters join together by sharing of faces, edges and vertexes and form fcc, hcp or icosahedral polyhedra, leading to MRO.

(5) The absence of orientational order of clusters gives rise to disorder at a long-range scale.

(6) There may exist defects, i.e. interstitial vacancies in MGs.

2.3 Glass-forming principles

Amorphous alloys, also named metallic glasses, are very promising for structural, chemical and magnetic applications due to their ultrahigh strength, excellent superplasticity, superior corrosion resistance and low coercivity [29]. However, there exist three unfavorable factors limiting their extensive applications: brittleness, small volume and thermal metastability. To make thermally stable bulk metallic glasses, a lot of principles have been proposed.

Before going to review these principles, it is necessary to mention a term of glass forming ability (GFA) used to describe the ability of glass transition of a system from liquid to glass. Three types of conditions are associated with GFA: thermodynamic, kinetic and processing factors. Thermodynamic factors include the melting temperature T_m, or the liquidus temperature T_L; the heat of fusion ΔH_m and vaporization ΔH_v; and the free energies of all possible phases during solidification. Kinetic factors are quantified by the homogeneous nucleation rate I_hom; the melt viscosity υ; and the glass transition temperature T_g. Processing factors encompass the cooling rate (a function of sample thickness); the supercooling temperature increment $\Delta T = T_m - T$; and the heterogeneous nucleation rate I_heter which depends on the melt purity and quenching surface preparation.

Cohen and Turnbull predicted that glass formation should be a universal phenomenon

[30]. They [31, 32] also agreed that a deep eutectic is the best candidate for metallic glass formation. The lower the reduced liquidus temperature, the greater the glass forming tendancy:

$$T_{\mathrm{Lr}} = \frac{k_{\mathrm{B}} T_{\mathrm{L}}}{\Delta H_{\mathrm{v}}} \tag{2.8}$$

where T_{L} is the liquidus temperature, ΔH_{v} is the molar heat of vaporization. As stated in Ref. [31], behind this expression is the physical implication that a little energy (i.e., low T_{L}) is required to produce a given amount of disorder at constant cohesive energy (ΔH_{v}), which could happen due to small changes in the contact angle of the coordination polyhedral. The formula is derived from the free volume model (FVM) and will thus find its limitation in more complex systems [31].

After then a more useful parameter, the reduced glass transition temperature T_{gr} was proposed to describe GFA:

$$T_{\mathrm{gr}} = T_{\mathrm{g}} / T_{\mathrm{m}} \tag{2.9}$$

To understand the correlation between T_{gr} and GFA, let’s look back to the conception of Gibbs free energy. It is known that the molar free energy difference ΔG_{xL} between the liquid and equilibrium crystalline alloy can be expressed as:

$$\Delta G_{\mathrm{xL}} = \xi(T) \Delta S_{\mathrm{m}} (T_{\mathrm{L}} - T) \tag{2.10}$$

where ΔS_{m} is the entropy of fusion, ξ is a temperature-dependent correction factor. Taking T_g into the equation, the driving force at T_g is given by:

$$\Delta G_{\mathrm{xL}}(T_{\mathrm{g}}) = \xi(T)\Delta S_{\mathrm{m}}(T_{\mathrm{L}} - T_{\mathrm{g}}) = \xi(T)\Delta H_{\mathrm{m}}(1 - T_{\mathrm{gr}}) \tag{2.11}$$

The expression (2.11) indicates that large T_{gr} accounts for ease of glass forming due to small driving force for crystallization. According to Davies' theory [33], T_{gr} is inversely related to the critical cooling rate because large T_{gr} signifies high viscosity of the melt and hence low atomic mobility and reduced R_{c}.

A problem with T_{gr} criterion is that there are no available data of T_g for most of glassy materials until they are examined. One way to overcome the difficulty is to introduce an semi-empirical approach employed by Marcus and Turnbull [34]. They investigated the correlation between glass forming tendency and $(T_{\mathrm{L}}^{0} - T_{\mathrm{L}})$ and gave the following equation to describe the GFA.

$$\frac{\Delta T}{T_{\mathrm{L}}^{0}} = \frac{T_{\mathrm{L}}^{0} - T_{\mathrm{L}}}{T_{\mathrm{L}}^{0}} \tag{2.12}$$

$$\text{where } T_{\mathrm{L}}^{0} = \frac{\Delta H_{\mathrm{f}}^{\mathrm{A}} T_{\mathrm{m}}^{\mathrm{A}}}{\Delta H_{\mathrm{f}}^{\mathrm{A}} - R\ln(1-x)\cdot T_{\mathrm{m}}^{\mathrm{A}}} \tag{2.13}$$

and T_{L}^{0}, $\Delta H_{\mathrm{f}}^{\mathrm{A}}$, $T_{\mathrm{m}}^{\mathrm{A}}$, and x respectively denote the ideal solution liquidus temperature, the heat of fusion of the solvent, the melting point of the solvent and the mole fraction of the solute. It is observed that the GFA in alloys increases with negative departure ΔT, which could be resulted from the strongly attractive part of the interaction potential between different atoms. This ΔT criterion will fail when applied to those alloy systems where the solubility of solute is large, specifically, more than 15%, or those where compound phases form because the ideal solution model is not obeyed by them.

Donald and Davies [35] developed a similar approach where $T_{\mathrm{L}}^{\mathrm{mix}}$ takes place of T_{L}^{0} in the above equation:

$$\Delta T^{*}=\frac{\Delta T}{T_{\mathrm{L}}^{\mathrm{mix}}}=\frac{T_{\mathrm{L}}^{\mathrm{mix}}-T_{\mathrm{L}}}{T_{\mathrm{L}}^{\mathrm{mix}}} \tag{2.14}$$

$$T_{\mathrm{L}}^{\mathrm{mix}}=T_{\mathrm{m}}^{\mathrm{A}}x_{\mathrm{A}}+T_{\mathrm{m}}^{\mathrm{B}}x_{\mathrm{B}} \tag{2.15}$$

where $T_{\mathrm{L}}^{\mathrm{mix}}$ is the melting point of mixtures, $T_{\mathrm{m}}^{\mathrm{A}}$ and $T_{\mathrm{m}}^{\mathrm{B}}$ are the melting points of the pure elements A and B. As discussed in the article [35], $\Delta T^{*}>2$ suggests an easy glass former and inversely a non-easy glass former at a cooling rate lower than 10^7 K/s. 68 melt-quenched binary and ternary alloys were assessed and agreed with the rule with only 8 exceptions.

Although the Donald-Davies model has a wide application in predicting the GFA of many binary systems and even ternary systems if the liquidus temperature is known, it turns to be invalid when applied to the binary systems that have an extensive primary solid solution.

To modify the model, Whang [36] introduced an additional parameter C_{er}, the reduced eutectic composition defined by:

$$C_{\mathrm{er}}=\frac{C_{\mathrm{e}}-C_{\mathrm{s}}}{C_{\mathrm{e}}} \tag{2.16}$$

where C_{e} and C_{s} denote the eutectic composition and the minimum hypoeutectic composition respectively. To understand the physical connotation of C_{er}, the new measure of GFA, $T_{0\mathrm{r}}$, should be noted. It is defined by:

$$T_{0\mathrm{r}} = \frac{T_0(C_\mathrm{e})}{T_\mathrm{e}} = 1 - \frac{T_\mathrm{m}^\mathrm{A} - T_\mathrm{e}}{T_\mathrm{e}}\left(\frac{2}{2 - C_\mathrm{er}} - 1\right) = 1 - \frac{\Delta T_\mathrm{m}}{T_\mathrm{e}}\left(\frac{2}{2 - C_\mathrm{er}} - 1\right) \tag{2.17}$$

where $T_0(C_\mathrm{e})$, T_e and T_m^A are respectively the temperature T_0 at the composition C_e, the eutectic temperature and the melting temperature of the pure element A. T_0 is the temperature where the two phases of the same composition have an equal free energy. Compared with T_g the role of T_0 is made clear: a glass is easily produced if $T_g>T_0$ meaning that the melt rigidifies before reaching the freezing temperature where there is no composition change [37].

It was observed that increasing $T_{0\mathrm{r}}$ makes glass transition difficult and even impossible after exceeding a critical value, for example, 0.9 for Ti-based binary alloys. Replacing $\Delta T_m/T_\mathrm{e}$ by T_Lr, $T_{0\mathrm{r}}$ can be expressed as:

$$T_{0\mathrm{r}} = 1 - T_\mathrm{Lr}\left(\frac{2}{2 - C_\mathrm{er}} - 1\right) \tag{2.18}$$

It is reasonable to suppose $T_{0\mathrm{r}}$ is constant, and then $T_\mathrm{Lr}[2/(2\text{-}C_\mathrm{er})\text{-}1]$ should be constant. A two-dimensional plot can be constructed by T_Lr as one axis and C_er as the other separating easy glass formers from non-easy glass formers. The Whang's model cannot work when a metastable phase competes with the glassy phase.

2.4 Liquid-to-glass transition

Liquid quenching is the common process to fabricate MGs, where the melt is solidified at a relatively fast cooling rate to avoid the crystallization. Although a wide variety of MGs have been produced by this technique, the phenomenon of liquid-to-glass transition in MGs remain somewhat mysterious because the underlying atomic rearrangement has not yet been well understood [38].

Much effort has been centered on the topic. On one hand, theories have been proposed to work out the structural feature and dynamic behavior of LGT, such as FVM [32], shear transformation zone (STZ) model [39], mode-coupling theory (MCT) [40] and potential energy landscape (PEL) [41]. Free volume is often assumed to be an excess volume where atoms can move around without energy change. Turnbull introduced the concept and attributed the glass transition to the decrease of the free volume on cooling [32]. Although FVM is able to reproduce the flow characteristics of MGs, the absence of fundamental thermodynamic definition of the free volume prevents it from extensive use [42]. STZ introduced by Argon is a plastic deformation unit which consists of tens or hundreds of atoms. Within PEL framework, STZ model reveals that there is one-to-one correspondence relationship between viscosity and STZ shear modulus [42] and that glass transition can be referred to as percolation transition of mechanically unstable regions [43]. In MCT, the glass transition is supposed as the singular behavior of motion equations of the dynamic structure factors and successfully applied to the supercooled liquids at a critical temperature T_c above which the systems have ergodic nature. Because it was initially developed for thermodynamic equilibrium systems, MCT distinctly fails to predict the dynamic behavior on the glass side. In PEL, the dynamics of supercooled liquids and glasses is interpreted as space configurational hopping between local energy minima, called metabasins. This perspective suggests two types of metabasins: liquidlike and solidlike, of which the latter account for the slowing down of dynamics upon cooling because of multistep escapes from them [44].

On the other hand, stimulated by those theories, a large amount of experimental and computational work has been performed [45-48]. The in situ X-ray experiment of Pd-based bulk metallic glass (BMG) confirms the existence of the critical temperature T_c predicted by MCT and shows that the structure factors follow the Debye theory up to the glass transition temperature [45]. The structural change and corresponding change in atomic dynamics and physical properties are understood as the result of the evolution of icosahedral ordering verified by the molecular dynamics analysis on Cu-Zr models [48]. According to the previous studies, the key to understanding the LGT lies in understanding the evolution of the atomic configurations.

2.5 Mechanical behavior of metallic glasses

MGs are attractive for structural applications due to their interesting combination of mechanical properties. Compared to their crystalline counterparts, MGs have the elastic moduli of the same order, but exhibit remarkably large yield strength coupled with a high elastic strain at yielding. This implies that MGs are able to sustain extremely large elastic recovery energy and are promising for shock-resistant use. In addition, MGs exhibit stable Newtonian viscous flow at high temperatures, making them suitable for superplastic forming. Despite these superior characteristics, there exists one unfavorable fact resisting their extensive use, i.e., MGs have little or even no plasticity. It is well known that the plasticity of a structural material under loading service is expected before total fracture to avoid any catastrophic failure. The absence of plasticity in MGs is agreed as the result of fast propagation of shear bands (SBs) [49, 50].

SBs are a narrow region where the plastic deformation of MGs takes place. They nucleate through the shear-induced dilatation and grow with the assistance of local heating [49, 51]. The propagation velocity of a SB is close to that of the sound [49, 50], which accounts for the rapid brittle fracture of MGs especially under tensile loads. This localized deformation region forms through the microscopic structural “defects” which has been elaborated elsewhere [4, 52] and will be revisited as follows.

Free volume model is one of the earliest theories first introduced by Cohen and Turnbull [32, 53] to explain the glass transition in amorphous alloys, and then extended by Gilman [54] and Spaepen [55] for understanding the plastic flow of MGs. From the energy perspective, the free volume of an atom is a vacant area where the atom travels around without the energy input to overcome the barrier. From the structural perspective, the free volume sites have a loose atomic packing density in comparison with the neighboring regions. Due to the weak mechanical bonding around the free volume zones, the inelastic transition can be expected and activated by either mechanical deformation or structural relaxation through the local rearrangement of atoms. This model has been successfully applied to interpret the strain softening in the plastic deformation of MGs. As the mechanical stress is loaded on the glassy structures, the shear deformation occurs by creating the excess volume because of the absence of the periodic arrangement. Although the relaxation could follow on by atomic diffusion, the diffusive motion is slow and the excessive defects remain, leading to the reduced deformation resistance, strain softening, and localized shear transformation. The deformation process based on the FVM is schematically illustrated in Fig. 2.2a, where a single atomic jump is enabled by shear stress.

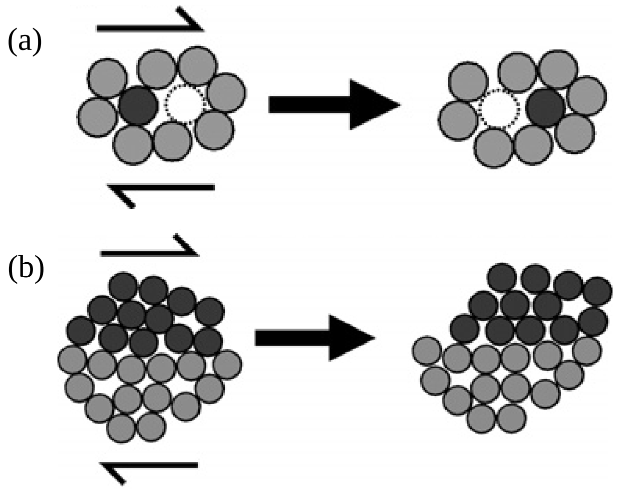

Figure 2.2 Schematically illustrated deformation mechanisms on the atomic length scale [52]. (a) Free volume model by Spaepen [55], and (b) shear transformation zone model by Argon [56].

Although the FVM is useful to explain the structural softening and inhomogeneous flow in MGs, it is not able to quantitatively describe the deformation process itself because a single atomic jump does not hold the shear strain.

Shear transformation zone model first applied to MGs by Argon [56] can tackle the problem with the FVM by recognizing the collective motion of atoms which has been verified experimentally and computationally. Argon in his early work [39] built a two-dimensional raft made up of two different sizes of bubbles in almost equal amounts to approximate the glassy structure. Upon shearing the rafts underwent shape change by a collection of very local shear transformations. Falk *et al* [57] adopted a numerical simulation on a two-dimensional binary noncrystalline system and revealed two-state STZs as an additional state variable for the constitutive equation of the viscoplastic deformation. These zones are very small, perhaps containing only five or ten molecules. Fig. 2.2b depicts a two-dimensional plastic deformation induced by the shear displacement of STZs. As concluded by Schuh *et al* [52], an STZ is in fact not a structural defect as compared to the dislocations in crystalline alloys; accurately, an STZ is a transition state which can only be detected upon deformation. It could be interesting to note that, according to the simulation work by Delogu [58], an individual STZ has an intermediate fractal dimensionality between line and plane.

The STZ operation can be readily activated at the energetic sites and similar to the atomic jump in the FVM, causes the structural dilatation. The dilatational volume is not eliminated by the slow relaxation process at low temperatures and therefore benefits the formation of new STZs. AS more and more STZs are activated to percolate, an embryonic SB forms, leading to the autocatalytic generation of STZs for the growth of the SB. When reaching a critical length [59], the SB will propagate in a runaway manner.

2.5.1 Size effects

It is necessary to specify whose dimension the “size” is before discussing its effect. In homogeneous polycrystalline metals, there exist two types of definitions: one indicates the specimen size whose effect can be expected when it approaches the order of the intrinsic microstructures (e.g., grains); the other indicates the grain size whose effect has been manifested in the well-known relation-the Hall-Petch equation [60, 61]. Since MGs do not have microstructural defects and are usually presumed to be elastically isotropic, and also this effect may vary from one testing mode to another, the specimen size effect will be addressed in terms of loading modes.

In compression, the most common mode, MGs show complicated plastic behaviors; some do not have plasticity, while some have prominent plasticity. The size-dependent behaviors also vary from glass to glass. In a Zr-based MG with a constant aspect ratio (height:diameter=2:1) [62], the small sample presents extensive plasticity which is highly localized in a few SBs, and no vein patterns form on its fracture surface. The yield strength appears independent of the specimen size investigated. The similar size-dependent plasticity has early been reported by Huang *et al* [63] where the sample diameters are adjustable to set the aspect ratio constant (2:1). The vein patterns remain on the fracture surfaces of all the samples, and the primary SB spacing increases with increasing sample diameter. Similarly, the yield strength has the positive size dependence. The discrepancy between the above two studies might arise from the different fabrication methods for the compression samples; in the former, all the samples were cut from a large drop-cast rod, while in the latter, the samples at various sizes were all prepared by drop casting into Cu molds in various diameters. For these reasons, the former relates the larger plasticity in smaller samples to the smaller elastic springback of the testing machine; the latter refers the phenomenon to the larger free volume per atomic volume in smaller samples which experience a faster cooling rate. Besides the effect of the specimen size (exactly, the diameter), the aspect ratio indeed influences the deformation behavior, too. The improved plasticity is usually attained in low-aspect-ratio samples due to the suppressed propagation of single SBs [64]. Nonetheless, the macro-compressive plasticity is still an issue of debate because of the various intrinsic or extrinsic effects.

So far all the compression testing discussed above is performed on a macroscopic length scale. As mentioned in the prior section, the plastic deformation of MGs is localized in a SB which is the result of the cooperative motion of STZs. The thickness of the SB is on the order of ten to a few hundred nanometers [52, 65, 66], and the size of the STZ is on the order of a few nanometers or below [67]. When the specimen size is comparable to these characteristic length scales, the different mechanical response could be imagined. Jang *et al* [68], by using the micro-compression on Zr-based MGs (most have a size below 1 μm), reported a transition of deformation behaviors from a localization mode at the size above 100 nm to a homogeneous mode at the size of 100 nm, which is considered to be the result of the dominant size-independent homogeneous flow. The compressive yield strength at 0.2% offset is reinforced down to a critical size and then holds constant. The similar transition for the plastic flow has already been observed in PdSi amorphous pillars [69]. Unlike the trend for the yield stress in the above work, the flow stress at 5% plastic strain, when near or in the homogeneous region, is reduced with decreasing pillar diameters; above the region, it remains nearly constant. Despite these contradictory facts, the knowledge on the plastic deformation of MGs keeps on expanding with the advancement of experimental techniques.

In macroscopic tension, monolithic MGs typically fail without showing plasticity; thus the microscopic tension will be discussed together. Different from the compressive fracture surface, the tensile fracture surface consists of round cores as well as shear offset and veins [70, 71]. The fracture starts from the shear offset which is a smooth region and related to the stable moving of the SB, carries on by the formation of the cores under the normal tensile stress, and propagates rapidly in a shear state. Wu *et al* [71], by doing a series of tensile tests, concluded that as the specimen has a size below the critical offset distance, the shear deformation is changed from unstable to stable, leading to the brittle-to-ductile transition. This conclusion sees its support in the work

[72] where the pronounced necking and large failure strain are both observed to occur in a nano-sized Zr-based MG under the *in situ* TEM tensile test. In the extreme case when the specimen size goes to that approaching the order of the SB thickness as demonstrated in [73], even atomic chain forms after necking, which is already reported experimentally and computationally in some metallic nanowires [74-77]. From these results, it could be inferred that the homogeneous flow should be common to amorphous alloys with a critical small size varying across glasses.

Regarding the computational technique, it is superior to the experimental technique in the sense that it can capture the electronic/atomic structures and relate them to the physical properties of bulk systems. Recently, Delogu [78], who performed the molecular dynamics of uniaxial compression on a binary MG, proposed a new insight into the size effect on the deformation behavior, exactly on the activity of STZs. He suggested that as the sample size is reduced so that a relatively large number of STZs consists of surface atoms as well, the autocatalytic activation of STZs is no longer operable because of the loss of the excess free volume on the surface. This assumption clearly throws light on the experimental facts described above that SB is hard to form when the specimen size is too small.

In bending, the sample is in both tensile and compressive stress states, and SBs are produced on the surface. As reviewed by Kumar *et al* [79], the shear offset distance and the SB separation are both proportional to the sample thickness, and when the offset is sufficiently smaller than the radius of the plastic zone, the bending plasticity will increase with reduction of the sample size.

At last, it is worth noticing that there is a special size effect referred to as indentation size effect (ISE), typically manifested as the increasing hardness with decreasing size. It is special in the definition of the “size” which is something not to do with the specimen dimension but to do with the indent depth or volume probed by the indenter. Indentation testing is operated in a constrained deformation mode with high hydrostatic pressure and high multiaxial stress states below the region of contact. During penetration, the hardness responds differently depending on the composition: most have the positive ISE, some have the negative ISE, and some do not have both. A multifarious nature for the positive ISE is already presented in the literature, such as the strain gradient [80] and the interface friction [81]. The negative ISE is likely due to the nanocrystallization induced by either heat or stress [82]. The disappearance of ISE may stem from the remarkably small characteristic material length scale.

Overall, the size-dependent properties shed light on the underlying deformation mechanisms and the potential application of MGs in miniaturization.

2.5.2 Temperature effects

At room temperature the plastic flow of BMGs is localized into SBs because of structural and thermal softening. The formation of SBs is related to the collective operation of STZs which are thermally activated. In addition, when heating up to above glass transition temperature, MGs enter into the supercooled liquid state. All the above processes are associated with temperatures. Thus, the temperature dependence of mechanical properties can be expected.

Regarding the temperature change in SBs, as Spaepen put it [51], it is very important for understanding the SB operation and improving the mechanical properties. As reviewed by Lewandowski *et al* [49], the early work treated the heating as adiabatic [83] and the calculated temperature increase was around 40 K [84]. However, the calculation was not correct in considering the thermal diffusion and did not recognize the even larger shear rate in SBs than the strain rate applied on the specimen. Later, more work was done and predicted the temperature rise going from a few kelvins to a few thousand kelvins [85-87]. The experimental evidence for local heating was already shown by Yang *et al* [88] who used the infrared thermography to measure the temperature increase of averagely 0.4 K. Due to the limited spatial and temporal resolution with the technique, the accurate temperature profile around the band cannot be revealed. Lewandowski *et al* [49] figured out a method with better resolution, the fusible tin-coating on a MG, and estimated the local temperature rise to be as high as a few thousand kelvin over a few nanoseconds. Recently, Cheng *et al* [89] found that the SB is not necessarily hot, depending on loading conditions. Furthermore, Miracle *et al* [90] revealed that the thermal profile is size dependent. From the above knowledge, MGs could appear ductile at low temperatures because the temperature rise in SBs is reduced. For example, a cryogenic compression was performed on a Ti-based MGs and demonstrated that the plasticity as well as strength increases with decreasing temperature (6.8% , 14.5% for plastic strain and 1.58, 1.71 GPa for yield strength, respectively at 298 and 123 K) [91]. The local heat around the shear-band front is partially relieved by low temperature. As a result, the SB growth becomes more difficult, possibly leading to the formation of more SBs or the rotation of SBs. The similar results have been reported in other MGs [92, 93].

Regarding the thermally-activated STZ activity, at low homologous temperatures, a critical shear event is driven at high stress and without diffusion-induced ordering process; at high homologous temperatures, the critical shear event, with assistance of large thermal energy, can occur at low stress. The shear stress (strength at yielding), as concluded by Schuh *et al* [52], is related to temperature by a power law with a temperature form of $(T/T_g)^{1/2}$. Johnson and Samwer [94] elicited the similar relation with a slightly different dependence of $(T/T_g)^{2/3}$. High-temperature nanoindentaion on a Au-based MG by Yang *et al* [95] proved that the Johnson-Samwer analysis is applicable to the hardness change with temperature in the inhomogeneous state. Besides the strength, the deformation behavior is also dependent on temperature. Nanoindentation experiments on two MGs [96], of which one is Pd-based having a high T_g (≈303 °C) and the other is Mg-based having a low T_g (≈135 °C), show that far below T_g (as of Pd-based), MGs deform inhomogeneously and the elevated temperature promotes the displacement bursts; while near or above T_g (as of Mg-based), homogeneous flow dominates as the stress required for such flow becomes smaller than for the inhomogeneous flow at low temperatures, and the serrations vanish. Other experiments such as compression [97, 98] also see the similar response.

In summary, the temperature-dependent behavior is reflective of the shear banding characteristics.

2.5.3 Strain rate effects

The strain rate response of SBs and mechanical properties has been investigated under a variety of loading modes. In uniaxial tension, a single SB tends to nucleate and grow rapidly along the maximum shear plane, resulting in the brittle fracture of MGs. In uniaxial compression, due to the geometrical constraints, MGs exhibit a limited plasticity through a series of shear banding events. Under both modes, the strength of MGs at room temperature is usually observed to be independent of strain rates over a broad range, at least six orders of magnitude from a quasi-static mode up to a low-velocity impact mode [52]. In contrast, some other experiments under these conventional modes distinctly revealed either positive or negative effects of strain rates [99-102]. Meanwhile, some computational work supports the strength scaling with rate for MGs at the nanometer scale [103, 104]. These contradictory results might occur for two reasons: firstly, as predicted in the theories [52, 94], MGs have an extremely low strain rate sensitivity beyond the resolution ability of these traditional loading methods; secondly, the strain rate effect could be influenced by a few factors, such as material composition, sample geometry, test temperature and loading mode.

Unlike these traditional loading techniques, instrumented nanoindentation is an important investigative technique with high spatiotemporal and force resolution, allowing for the precise measurement of stress drops or displacement bursts in materials [105]. In this respect, nanoindentation is a more helpful way to study the deformation behavior of MGs. Recently, experiments under this mode have been widely conducted to probe the loading/strain rate effect [106-109]. Pan *et al* [107] employed a skillfully designed method (i.e., rate-change indentation) and found that the hardness of both Ni-based MG and nanocrystalline nickel increases slightly with elevated loading/strain rates when measured at high loading rates (≥13.2 mN/s) underneath large depths (>1 μm), while Sort *et al* [106] observed the opposite effect of loading rates over a large range at a depth less than 300 nm, which is attributed to the enhancement of free volume therein.

2.6 Applications of metallic glasses

Table 2.1 gives an outline of potential applications of MGs. Since the birth of the first MG Au-Si at Caltech, researchers have made persistent and successful efforts in applying them to practical use, such as industrial coatings, digital casings, storage devices, electronics cores, and space projects [110, 111]. Rather than discussing these applications by alloy category, it is preferable to organize them according to a property or characteristic.

2.6.1 Mechanical properties

The high strength, hardness, fracture toughness, elastic stain limit and low Young's modulus makes MGs specially attractive to structural applications.

a. Sporting, electronic and other consumer goods

Lighter and stronger materials are demanded in the sporting industries where MGs could play gracefully. The earlier commercial use can be found in golf clubs [112], and then expanded to tennis rackets, bicycle frames, fishing equipment and so on [111].

The incorporation of MGs into electronic products can be dated back to the year of 2002 when Liquidmetal technologies began producing liquid crystal display casings on cell phones [113]. These alloys combine both performance and processing characteristics and assure more excellent durability.

Fine jewelry is the newest application field where MGs prove superior to other crystalline metals because of strength, processing and finishing advantages [114]. For example, platinum-based MGs have low liquidus temperature of 522℃, large supercooled liquid region of 98℃ for easy processing and low critical cooling rate representing large casting thickness of 20mm. They show high yield strength (e.g., 1400MPa for $Pt_{57.5}Cu_{14.7}Ni_{5.3}P_{22.5}$), are friendly with gemstone and thus do not degrade the gem.

Table 2.1 Applications of metallic glasses based on mechanical, chemical, magnetic properties and superplastic forming ability

Material	Application	Property	Source	Year
$Ti_{41.5}Zr_{2.5}Hf_5Cu_{42.5}Ni_{7.5}Si_1$	Mass flowmeter	Low Young's modulus, high strength	[115]	2007
$Zr_{55}Al_{10}Ni_5Cu_{30}$	Pressure sensor			
$Zi_{44}Ti_{11}Cu_{10}Ni_{10}Be_{25}$	Replication of features on silicon mold	Superplasticity	[116]	2007
$Pd_{77.5}Cu_6Si_{16.5}$	Patterning		[117]	2007
Fe-Cr-Mo-Al-Y-C-B	Bipolar plate in fuel cells	Corrosion resistance	[118]	2006
$Mo_{31}Si_{20}N_{45}$	Bridge-type or cantilever-type varactor	Good conductivity, favorable mechanical attribute	[119]	2006
$Zr_{55}Cu_{30}Al_{10}Ni_5$	FIB Nanopatterning		[120]	2006
Co-Fe-B	Free and reference layer of SDT junctions		[121]	2004
$Pd_{76}Cu_7Si_{17}$	Spring linear actuator		[122]	2003
	Inductor	Good conductivity	[123]	2003
	Microforming of cantilever		[124]	2003
$Zi_{41.25}Ti_{13.75}Cu_{12.5}Ni_{10}Be_{22.5}$ (Vitreloy1)	Substrate of Surface acoustic wave device	Low as-cast surface roughness	[125]	2002
$Fe_{70.2}Co_{7.8}Si_{12}B_{10}$	Strain sensor based on magnetic tunneling junctions (MTJs)	Magnetostrictivity	[126]	2002
$Zr_{75}Cu_{19}Al_6$	Electrostatic microactuator		[127]	1999
$Fe_{40}Ni_{38}Mo_4B_{18}$	Microsensors for remote query	Magnetoelasticity	[128]	1999

b. Industrial applications

MGs have moved their steps into extensive application areas, e.g. medical, automobile and aerospace industries besides the above mentioned.

In medical industry, Vitreloy has been used for production of ophthalmic scalpel blades, knives and razor blades due to high quality but less expensive processing.

In automobile industry, valve springs made of Zr-based MGs were invented at the research lab [129]. Replacement by a Zr-based MG will reduce the overall weight of an engine and thus improve fuel consumption.

Up to the present, only Zr-Nb-Cu-Ni-Al was reported to be used in aerospace as a coating layer catching solar wind [113].

c. Coatings and reinforcement in composites

MGs obtain their application in coatings industry due to high wear resistance. Fe-based amorphous alloy (e.g. Armacor developed by Liquidmetal) is now commercially available in the refinery coker wall, firebox, and oil drill pipe. Amorphous coatings also catch lab researchers’ attention. Recently, AISI 4140 steel coated with Fe-Cr-Mo-Y-B-C MG was attempted by laser surface processing, revealing improvement in hardness and wear resistance although amorphous structure does not remain after processing [130]. Meanwhile, Fe-B-Si-Cr-Mo amorphous coating was successfully prepared on a 304 stainless-steel substrate by gas tunnel type plasma spraying [131]. Abrasive wear test shows that the MG coating has a higher abrasive wear resistance than SUS substrate.

Beyond coatings application, MGs as reinforcement in composites are quite promising as well. In early 1980s, MG ribbons were added into epoxy resin and enhancement of tensile strength was observed (36~67% increase in fracture strength depending on the stress state of the MG ribbons) [132]. Several years later, MG ribbons were introduced into glass ceramics and significant improvements in strength (80.7~120.4% increase in fracture stress depending on the reinforcements and their volume fraction), fracture toughness of matrices (151.9~270.6% increase) were found [133]. Recently, Al-based metal matrix composites reinforced with Al-Y-Ni-Co glassy powders were formed by powder metallurgy method, exhibiting high strength (up to 295 MPa for the composites with 50 vol. % glassy phase as compared to 155 MPa for pure Al) and ductility (ranging between 7% and 10% at maximum stress) [134].

2.6.2 Magnetic properties

Soft magnetic MGs with low coercivity and high electrical resistivity are very suitable for transformer cores. Fe-Al-Ga-P-C-B-Si glassy alloy powders prepared by Yoshida *et al* [135] were made into a core which has a constant permeability of about 110 up to 10MHz in comparison to commercial cores and a very low core loss of 610 kW/m^3 in a magnetic field of 100 kHz, 0.1 T. Based on these distinguished high frequency magnetic properties, magnetic-shielding sheets for laptops were fabricated [136]. Metglas 2605SA1 (Fe-based, “metglas” is a trademark), a commercial magnetic material has an as-cast saturation induction of 1.56 T, maximum permeability of 45,000, and coercivity as low as 1.2 A/m, resulting in extremely low core loss—less than 0.2 W/kg at the magnetic field of 60 Hz, 1.4 T and suggesting brilliant use for motors and high frequency inductors.

A problem with MGs is their small size that limits them to a range of small-scale applications before the year of 2000. Nevertheless, it is now possible to use MG ribbons at a large size (more than 100 mm in width) [110]. The world's largest amorphous metal-based distribution transformer was produced in Korea 2007, the size of which is 3.7 m×3.95 m×3.5 m (width×depth×height) with efficiency of 99.31%.

2.6.3 Chemical properties

The superb corrosion resistance present in MGs is believed to originate from the amorphous structure, composition and the passive films growing on the surface. A review has been given elsewhere [137] on corrosion resistance of Zr-, Ni-, Fe- and Cu-based BMGs, where the corrosion resistant properties are correlated with compositon and surface films.

Friendly biomaterials are undergoing an expanding need and seem to be the most likely application field exploiting the corrosion resistant properties of MGs. Most recently, a Ti-Pd-based MG without toxic elements was developed [138] with good bending plasticity, high glass transition temperature of 797 K, large supercooled liquid region of 36 K, and superior passivating performance in a lower current density of around 10^{-2} A/m^2 compared to Ti and Ti6Al4V alloys. Relying on these properties, the Ti-Pd-based MG is very appropriate for use in an orthopedic bone fixation device.

Fuel cell technology is a hot area driven by the energy needs and environmental issues. Bipolar plates (BPs) are one of the most key parts accounting for 60~80% of weight and 29~45% of cost in a fuel cell stack [139, 140]. Fe- and Ni-based MGs have been selected for materials as BPs [141, 142]. The findings show that both Fe- and Ni-based MGs are better in corrosion resistance than SUS316L while Ni-based MGs exhibit more excellent performance.

In conclusion, the widespread use of MGs can be expected based on those good mechanical, magnetic and chemical properties.

2.7 Summary

MGs are very fascinating due to their excellent physical and chemical properties. A large number of MGs have been developed with good mechanical properties and thermal stability. Based on these superior properties, MGs have seen their wide applicatinons in the industrial fields such as coatings, digital casings, storage devices, electronics cores, and space projects.

Atomic structure is the origin of material properties. Unlike crystals, MGs do not have crystallographic symmetry and long-range structural periodicity, and thus there are no crystalline defects in the amorphous structure. A few models such as DRP and ECP have been proposed to clarify the amorphous structure, although they are not sufficient to represent all the structural features in MGs (see Section 2.2). So far it is agreed that the amorphous structures especially in strong glass formers are not fully composed of randomly packed atoms; in fact, they exhibit short-to-medium range order. As a result, the mass density is quite close to that of their crystalline forms.

Due to the absence of defects, MGs deform plastically through the propagation of SBs which are localized in a very thin region. As the propagation is as fast as the sound velocity, MGs fail without showing macroscopic plasticity. The rapid propagation results from the structural softening. Two models were already proposed to recognize that the softening arises from the shear-induced dilatation: free volume model and shear-transformation-zone model. In addition, the shear banding characteristics (e.g., the temperature profile in the SBs, the shear strain rate, *etc*.) are influenced by testing conditions, such as specimen size, temperature and strain rate.

In review of the past efforts, it is hoped that the work in this project may expand the knowledge on thermal and mechanical properties of MGs so as to further establish their relationship and improve the properties.

Chapter 3 Amorphous Structure and Thermal Properties of Metallic Glasses

3.1 Introduction

As introduced in the literature review chapter, atomic structure is the origin of material properties. In addition, this project focuses upon MGs. Thus, it is necessary to identify the amorphous nature of the as-prepared materials prior to the investigation of their properties.

In this chapter, nine amorphous compositions are fabricated which present largely different glass transition temperatures ranging from approximately 100 ℃ up to 500 ℃ (see Table 3.4). Their glassy structures are verified by experimental methods. Computational methods are used as a complementary tool to give an insight into the amorphous structure. Finally, the thermal properties of these compostions are characterized and discussed.

3.2 Experimental methods

3.2.1 Melt spinning

Melt spinning is a technique most commonly used for production of MGs due to the rapid cooling rates (normally ranging from the order of 10^4 to 10^7 K/s [143]). An alloy ingot is melted, usually in a quartz crucible and by radio-frequency induction. The melt runs through a nozzle of the crucible, is ejected against a cold rotating copper wheel and solidified into a continuous ribbon. The width of the ribbon is adjusted by the size of the nozzle while the thickness is controlled by the rotating speed of the wheel. The set-up configuration of the melt spinner is illustrated in Fig. 3.1 [143].

In this work, Al-based and Mg-based amorphous ribbons were both fabricated by melt spinning in an argon atmosphere. The wheel speed is 30 m/s for Al-based ribbons and 10 m/s for Mg-based ribbons; the former have a thickness of ~20 µm and a width of ~3 mm, whereas the latter have a thickness of ~100 µm and a width of ~2 mm.

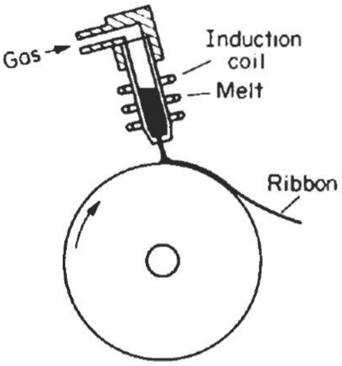

Figure 3.1 The set-up configuration of a melt spinner [143].

3.2.2 Magnetron sputtering

Magnetron sputtering is a method of depositing thin films with application of a magnetic field. The sputtering process is operated in a vacuum chamber which is evacuated to a base pressure and then backfilled with a continuous flow of gas such as Ar. The gas, under a discharge voltage, is ionized and the ions bombard the surface of a so-called “target” material where coating atoms are knocked off and condense as a thin film on a “substrate”. The magnetic field is introduced to confine the motion of electrons and thus sustain the ionization. Compared to other rapid solidification techniques such as melt spinning, sputter deposition is more effective in making glassy structures because the rapid cooling rates are more easily achievable. Fig. 3.2 gives a system configuration of a magnetron sputtering.

In this work, CuZr thin films were deposited on Si (100) substrates by magnetron sputtering system under an argon (Ar) atmosphere. The base pressure was 2.0–2.5×10^{-4} Pa, and the sputtering process Ar pressure was 0.3 Pa. To achieve the desired compositions, two targets were used; one a $Cu_{50}Zr_{50}$ alloy target operated under direct-current (DC) power of 250 W and the other a Cu target with a radio-frequency (RF) power of 0, 25, 50, 100 and 120 W. The Si substrates were placed on a holder rotating around a central axis at a constant speed (i.e., about 20 cycles/min). To strike off the possibly existing oxide layer on the target surface, pre-sputtering was carried out for a few minutes (within 2 mins), followed by a sputtering process for ~220 mins. The thickness of the thin films ranges from 3.5 to 4.6 μm. Shown in Fig. 3.3 is the Cu content as a function of RF power, where a linear relationship is obviously observed.

3.2.3 X-ray diffraction

X-ray diffraction (XRD) is a non-destructive method for quantitative analysis on phase composition of materials. In this work, XRD was operated on a system (Philips X'pert 1830) using monochromatic CuK_{α} radiation (λ=0.1542 nm). The detector step size is 0.02 ° with a scan rate of 1.00 °/min. The work voltage and current are respectively maintained at 30 kV and 20 mA.

3.2.4 Scanning electron microscopy

Scanning electron microscopy (SEM) has seen a lot of applications to materials characterization: surface morphology by secondary electron imaging, phase identification by backscattered electron imaging, and compositional analysis by energy dispersive X-ray spectrometry (EDX or EDS), *etc.*, which are due to the interaction of incident electron beams with the surface of test materials. SEM imaging is realized by raster scan of fine focused beams over the sample surface, and the size of interaction volume accounts for the imaging resolution.

In this work, SEM imaging was carried out on JEOL JSM-5600LV under an accelerating voltage of 20 kV. The chemical composition was analyzed using EDX (Oxford Instruments).

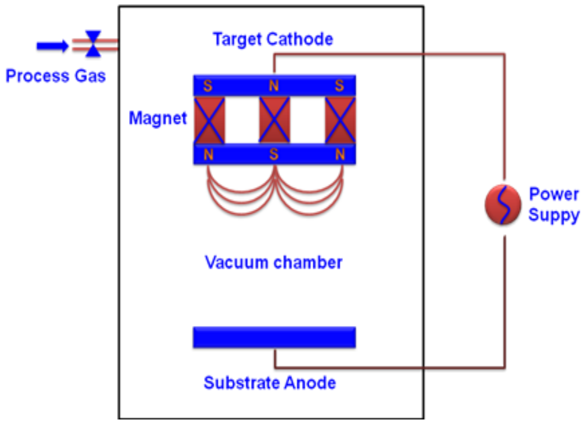

Figure 3.2 Schematic representation of a magnetron sputtering system for the fabrication of thin films.

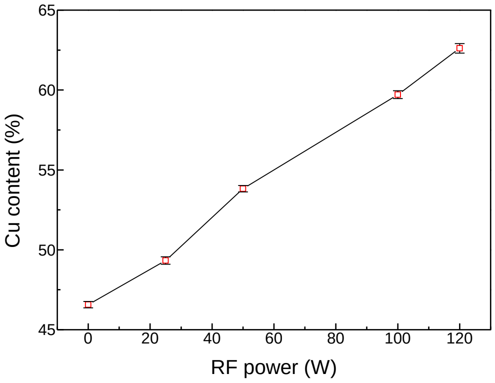

Figure 3.3 Compositional dependence of Cu_xZr_{100-x} thin films on radio-frequency (RF) power.

3.2.5 Transmission electron microscopy

Transmission electron microscopy (TEM), is to form an image by “seeing” electrons travelling through a thin specimen. Unlike SEM, TEM has a imaging process that the object plane of the intermediate lens coincides with the image plane of the objective lens so that the image is projected onto the viewing screen.

In the current project, TEM was operated on JEOL2010 at an accelerating voltage of 200 kV. As amorphous structure could be damaged (e.g., crystallization) when subjected to ion milling at a beam energy above 3 keV, two very thin specimens were fabricated for direct TEM observation; one deposited on a PMMA substrate by sputtering of a $Cu_{50}Zr_{50}$ target at a DC power of 100 W for 4 mins, and the other deposited on the same substrate by co-sputtering for 2.5 mins at a DC power of 250 W for $Cu_{50}Zr_{50}$ target and a RF power of 50 W for Cu target. Then, they were transferred onto a Cu grid by dissolving PMMA with acetone.

3.2.6 Differential scanning calorimetry

Heat flow during physical or chemical process can be detected by differential scanning calorimetry (DSC). This thermoanalytical technique has been widely used to measure the characteristic temperatures where phase transitions (e.g., glass transition, crystallization) occur.

In this study, thermal analysis was carried out using TA Q200 DSC. Temperature and heat of fusion are both calibrated by using standard reference materials (indium and zinc). The test mass varies, depending on specimens; for those in a bulk or ribbon form, it is 10-20 mg, whereas for those in a thin film form, it is 1-2 mg. The specimens were wrapped in Al pans and then loaded into the DSC pressure cell filled with a continuous flow of Ar gas at a flow rate of 50 mL/min for bulk or ribbon specimens and 200 mL/min for thin film specimens. After temperature equilibration, they were continuously heated up at various heating rates (5-80 K/min) to above full crystallization temperature and then cooled down, followed by a second heating run as a baseline. Glass transition temperature (T_g), crystallization temperature (T_x) and heat enthalpy (ΔH_x) are calculated by following the methods in ASTM E1356 and ISO 11357.

3.3 Computational methods

Molecular dynamics simulation (MDS) is a computational method by which the motion of atoms or molecules can be calculated according to the Newtonian mechanics. Incorporated with computer simulation, materials research takes on a new look and can be visualized. Visualization means that change at the atomic or microscopic scale can be observed. Using MDS helps correlate the atomic process with the bulk properties, which is indeed useful for materials design.

3.3.1 Statement of purpose

Even though TEM is commonly used to characterize 2D structure of MGs at an atomic scale, it is most often difficult if impossible to image atomic configurations due to multiple factors such as spherical aberration and sample thickness. Atomic configuration is herein defined as the way of atomic arrangement especially in the first and second neighboring shells. The emergence of MDS, however, makes it possible to "observe" such short-to-medium-range order structures.

In the computational work (Section 3.4.2), $Ti_{50}Cu_{50}$ compound was selected as model system. The structural evolution and short-to-medium-range order structures will be investigated as an extension of experimental work (Section 3.4.1). The reasons for the choice of the $Ti_{50}Cu_{50}$ system are as follows:

(1) It contains only two metallic elements, which is preferable for simulation from the viewpoints of both computational efficiency and accuracy. Systems with more than two elements are not interesting because few potential functions are available, while one-element systems are not technologically attractive because they are difficult or even impossible to be made glassy in experiments.

(2) It is chemically similar to $Cu_{50}Zr_{50}$ which will be studied in experiments (Section 3.4.1). $Ti_{50}Cu_{50}$ has been known as a poor glass former from the viewpoint of reduced glass transition temperature (e.g., 0.47 from Ref. [144]), while $Cu_{50}Zr_{50}$ is one of the best glass formers among binary amorphous alloys. Since a lot of work has been performed on the atomic structure of $Cu_{50}Zr_{50}$, the study on a poor glass former would give an alternative perspective for the effect of atomic structure on the glass forming behavior.

(3) The fast atomic dynamics in a poor glass former may be suitable for investigation of structural evolution on rapid quenching.

3.3.2 Simulation conditions

The computational study is carried out with Materials Explorer 5.0. Presented in Fig. 3.4 is the diagram of typical simulation process.

The selection of conditions is critical for correct simulation. These conditions include potential function, timestep size and cutoff radius.

3.3.2.1 Potential function

Potential function is the most important factor because it defines the interatomic action. The more accurate the potential, the more reliable the simulation is. In the present study, general embedded-atom method (GEAM) is used to describe the interatomic forces.

The total energy of GEAM takes the form [145, 146]

$$E_{\text{tot}} = \frac{1}{2}\sum_{i,j,i\neq j}\phi_{\text{ij}}(r_{\text{ij}}) + \sum_{\text{i}} F_{\text{i}}(\rho_{\text{i}}) \tag{3.1}$$

$$\phi_{\text{ij}}(r_{\text{ij}}) = \phi_{\text{e}} \exp[-\gamma(r_{\text{ij}}/r_{\text{e}} - 1)] \tag{3.2}$$

where ϕ_{ij} is the two-body potential between atoms i and j separated by r_{ij}, r_{e} is the equilibrium spacing between nearest atoms, and F_{i} represents the embedding energy depending on ρ_{i}, the electron density which can be expressed as

$$\rho_{\text{i}} = \sum_{j,\, j\neq i}\varphi_{\text{j}}(r_{\text{ij}}) \tag{3.3}$$

$$\varphi_{\text{j}}(r_{\text{ij}}) = \varphi_{\text{e}} \exp[-\beta(r_{\text{ij}}/r_{\text{e}} - 1)] \tag{3.4}$$

where φ_{j} is the electron density at atom i due to atom j at a distance r_{ij}. The parameters (e.g., ϕ_{e}, r_{e}, φ_{e}, γ and β) in the above expressions are obtained by fitting to basic material properties such as lattice constants, elastic constants, vacancy formation energies, *etc*. [145].

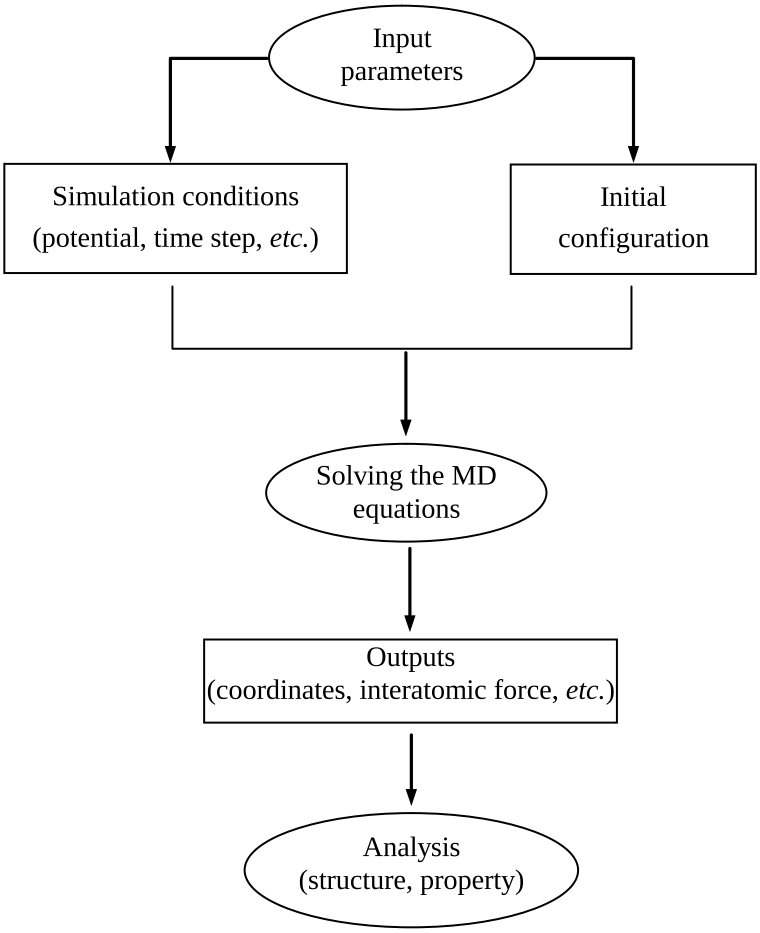

Figure 3.4 Flow chart depicting the various steps of MD simulation process

The system evolves under control of fifth-order Gear's predictor-corrector algorithm, which consists of three basic steps. The first step is to predict atomic positions r_i at time t+Δt using a fifth-order Taylor series:

$$r_{\mathrm{i}}(t+\Delta t)=r_{\mathrm{i}}(t)+\dot{r}_{\mathrm{i}}(t)\Delta t+\ddot{r}_{\mathrm{i}}(t)\frac{\Delta t^{2}}{2!}+r_{\mathrm{i}}^{(\mathrm{iii})}(t)\frac{\Delta t^{3}}{3!}+r_{\mathrm{i}}^{(\mathrm{iv})}(t)\frac{\Delta t^{4}}{4!}+r_{\mathrm{i}}^{(\mathrm{v})}(t)\frac{\Delta t^{5}}{5!} \tag{3.5}$$

$$\dot{r}_{\mathrm{i}}(t+\Delta t)=\dot{r}_{\mathrm{i}}(t)+\ddot{r}_{\mathrm{i}}(t)\Delta t+r_{\mathrm{i}}^{(\mathrm{iii})}(t)\frac{\Delta t^{2}}{2!}+r_{\mathrm{i}}^{(\mathrm{iv})}(t)\frac{\Delta t^{3}}{3!}+r_{\mathrm{i}}^{(\mathrm{v})}(t)\frac{\Delta t^{4}}{4!} \tag{3.6}$$

$$\ddot{r}_{\mathrm{i}}(t+\Delta t)=\ddot{r}_{\mathrm{i}}(t)+r_{\mathrm{i}}^{(\mathrm{iii})}(t)\Delta t+r_{\mathrm{i}}^{(\mathrm{iv})}(t)\frac{\Delta t^{2}}{2!}+r_{\mathrm{i}}^{(\mathrm{v})}(t)\frac{\Delta t^{3}}{3!} \tag{3.7}$$

$$r_{\mathrm{i}}^{(\mathrm{iii})}(t+\Delta t)=r_{\mathrm{i}}^{(\mathrm{iii})}(t)+r_{\mathrm{i}}^{(\mathrm{iv})}(t)\Delta t+r_{\mathrm{i}}^{(\mathrm{v})}(t)\frac{\Delta t^{2}}{2!} \tag{3.8}$$

$$r_{\mathrm{i}}^{(\mathrm{iv})}(t+\Delta t)=r_{\mathrm{i}}^{(\mathrm{iv})}(t)+r_{\mathrm{i}}^{(\mathrm{v})}(t)\Delta t \tag{3.9}$$

$$r_{\mathrm{i}}^{(\mathrm{v})}(t+\Delta t)=r_{\mathrm{i}}^{(\mathrm{v})}(t) \tag{3.10}$$

The second step calculates the interatomic force f_{i} on each atom at time $t+\Delta t$ using the predicted position:

$$f_{\mathrm{i}}=-\sum_{j,\,j\neq i}\frac{\partial\phi(r_{\mathrm{ij}})}{\partial r_{\mathrm{ij}}}\vec{\mathrm{r}} \tag{3.11}$$

where $\vec{\mathrm{r}}$ is the unit vector in the r_{ij} direction.

The last step is to correct the predicted positions and their derivatives using the discrepancy $\Delta\ddot{r}_{\mathrm{i}}$ between the predicted acceleration and that given by the evaluated force f_{i}:

$$\Delta\ddot{r}_{\mathrm{i}}=\left[\ddot{r}_{\mathrm{i}}(t+\Delta t)-\ddot{r}_{\mathrm{i}}^{\mathrm{f}}(t+\Delta t)\right] \tag{3.12}$$

3.3.2.2 ***Timestep***

Timestep is Δt in Gear's predictor-corrector algorithm, which directly influences the computational errors and thus accuracy of the simulation result. From the viewpoint of computational efficiency, a large timestep size is preferable. However, a small timestep size is better from the viewpoint of computational accuracy. The choice of timestep is dependent on system size, controlling algorithms, potential functions, simulation time and so on. Due to a lot of factors affecting the determination of timestep size, it is better to use the trial-and-error method before performing a simulation.

In this study the effect of timestep size was examined on the properties of systems with different size and found that the system is stable when the timestep size is lower than 5 fs and becomes fluctuating when the timestep size is larger than 5 fs.

3.3.2.3 Cutoff radius

Cutoff radius is a distance where the interatomic force can be taken as zero. On one hand, a large cutoff radius will increase the number of calculations. On the other hand, a small cutoff radius can make the calculation deviate from the real solution. Trial and error method is used again to determine the cutoff radius.

To this aim, a model structure was built with 576 particles divided equally by Ti and Cu atoms. The timestep size is 1 fs. The cutoff radius was set as 5, 6, 7.5 and 10 Å, respectively. Then, the relaxation run was performed. The potential energy is monitored to see how it changes with cutoff radius, which is given in Fig. 3.5.

It is evident that the potential energy decreases rapidly and becomes almost constant beyond the cutoff radius 7.5 Å. Therefore, the cutoff radius of 10 Å is chosen in the following work.

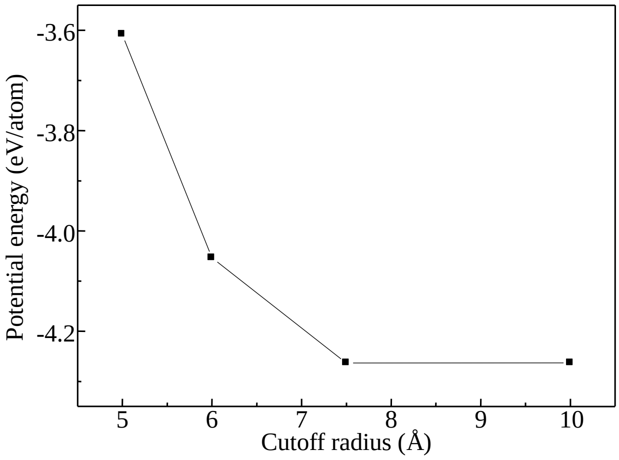

Figure 3.5 Change of potential energy with cutoff radius

3.3.3 Analysis techniques

The common techniques, which are used to characterize the atomic structure in simulation, involve radial distribution function (RDF) and Voronoi tessellation analysis (VTA).

3.3.3.1 Radial distribution function (RDF)

Since there is no periodicity in noncrystalline materials, RDF is a good method to describe the atomic arrangement in them. RDF is defined as the possibility of finding an atom at a distance *r* from the origin. For simplicity of explanation, a schematic picture showing the definition of RDF is given in Fig. 3.6. From a mathematical standpoint, the RDF is the integration over the peak, i.e., the dotted region in the figure. From RDF patterns, a few structural characteristics can be calculated such as the degree of order, CN and bond length as follows: the degree of order is determined by the intensity and width of RDF peaks; $\mathrm{CN} = 4\pi\rho\int_{\mathrm{r}} r^2 g(r)\mathrm{d}r$, where ρ and $g(r)$ stands respectively for the average number density of atoms and RDF; bond length is defined as the distance where the first peak reaches the maximum intensity.

3.3.3.2 Voronoi tessellation

RDF just presents the average structural information and does not show polyhedral construction in 3D space. Voronoi tessellation deals with this problem by seperating 3D space into Voronoi cells [147, 148], the analog of Wigner-Seitz cells in crystalline materials. So one configuration can be distinguished from another through Voronoi index $<n_3, n_4, n_5, n_6, \cdots>$, where n_i stands for the number of *i*-edged faces of a Voronoi cell and $\sum n_i$ is the total CN. For example, the Voronoi indices of bcc, hcp, fcc and icosohedron are <0, 6, 0, 8>, <0, 12, 0, 0>, <0, 12, 0, 0>, and <0, 0, 12, 0>, respectively. According to VTA, some quantities can be calculated such as Voronoi volume, surface area of model system and distribution of atomic configurations.

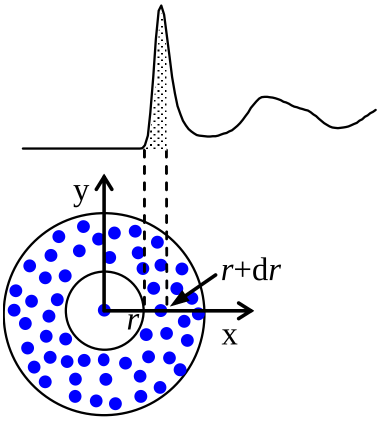

Figure 3.6 Schematic picture showing the definition of RDF

3.4 Amorphous structure

3.4.1 Experimental characterization

Nine MG compositions were surveyed (see Table 3.1). Prior to measurement of their properties, it is necessary to confirm that they are fully amorphous. XRD and TEM are complementary methods for structural characterization. Shown in Fig. 3.7 are the XRD spectra for all the compositions of this study. Over the whole range of diffraction angle, no crystalline peaks appear. A broad diffraction peak typically occurs, which is characteristic of amorphous structure. The diffraction angle where the broad peak emerges depends on the composition; for example, in Fig. 3.7a, La-based MG has an angle of 31.12 °, while the others have an angle of around 38 °. Interestingly, in Fig. 3.7b, the diffraction halo maximum for Cu_xZr_{100-x} thin films shifts to the right as the Cu content increases.

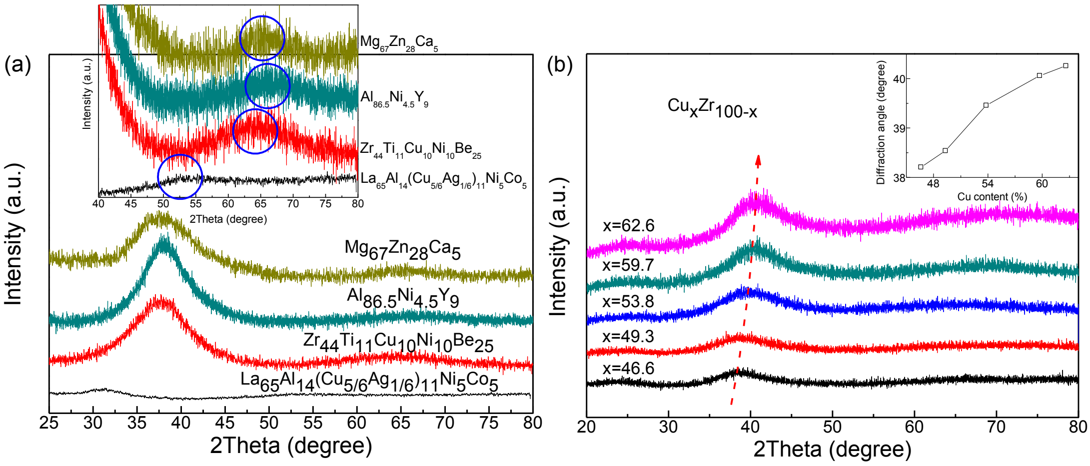

Figure 3.7 X-ray spectra for nine compositions in (a) a bulk or ribbon form and (b) a thin film form. In (a), indicated by circles are the areas where a second amorphous peak occurs.

It is known that, when assuming the amorphous structure consists of only one type of atom, the X-ray scattered intensity due to a particular interatomic distance r can be described as [149]:

$$I_r(\mathbf{k}) = N_r f^2(\mathbf{k})\left[1+\frac{\sin(2\pi\mathbf{k}\cdot\mathbf{r})}{2\pi kr}\right] \tag{3.13}$$

where N_r is the number of atoms at a separation r, $f(\mathbf{k})$ is the atomic scattering factor, and $\mathbf{k}$ is the scattering vector. The intensity has maxima at $2\pi kr=(1+4n)\pi/2$ (n=1, 2, 3, …). The average radius R_s of the first coordination shell is thus given as [149]:

$$R_s = r = \frac{5}{4}\cdot\frac{\lambda}{2\sin\theta}, \quad n=1 \tag{3.14}$$

where λ is the X-ray wavelength and θ is the angle where a maximum occurs in the diffraction pattern. According to the above equations, there are two points worth noting: the first is that the scattered intensity is closely related to atomic distance; the second is that the term $\lambda/(2\sin\theta)$ representing the Bragg equation can only be applied to amorphous materials when multiplied by a factor, e.g., 5/4 in Eq. 3.14. In practice, the factor has a smaller value of 1.22 [150].

Now it is understood that the peak shift with addition of Cu corresponds to the decrease in R, which is attributed to the smaller size of Cu atoms than that of Zr atoms. The average radius R is summarized in Table 3.1. Metallic bonding is normally dominant in MGs. However, there exists a covalent component in Mg-based alloys. Careful analysis on XRD patterns in Fig. 3.7a reveals that, beyond the first broad peak, there usually exists a second broad peak with very low intensity (indicated by circles in the inset of Fig. 3.7a), which is related to medium-range-order structures.

Fig. 3.8 presents the TEM images and corresponding selected-area electron diffraction (SAED) patterns for CuZr thin films (refer to Section 3.2.2 for detailed sputtering conditions) and an as-quenched $Al_{85}Ni_5Y_8Co_2$ ribbon (courtesy of H. W. Yang [151]). No obvious lattice fringes exist, which suggests random atomic arrangement. A sharpening secondary halo, marked by a white arrow in the inset diffraction patterns, has been related to medium-range order [152]. Such length-scale order cannot be accessible by conventional techniques using X-ray, electron or neutron beams because they typically characterize the structure over a comparatively large volume of specimen. In the next subsection, a simulation method will be used to “see” the atomic structure at the short-to-medium range of length.

Table 3.1 Information on nine compositions surveyed in this project. R_{Bragg}, R_{m} and R_{c} indicate the radius calculated from the Bragg equation, the metallic bonding length and the covalent bonding length.

Composition	Fabrication method	Geometry, thickness (μm)	R_{Bragg} (Å)	R (Å)	R_{m} (Å)	R_{c} (Å)	Exp. (Å)
$Al_{86.5}Ni_{4.5}Y_9$	Melt spinning	Ribbon, ~20	2.37	2.89	Al-Al 2.86 Al-Ni 2.67 Al-Y 3.21	Al-Al 2.36 Al-Ni 2.33 Al-Y 2.80	For $Al_{87}Y_8Ni_5$ [153]: Al-Al 2.86 Al-Ni 2.68 Al-Y 3.20
$Mg_{67}Zn_{28}Ca_5$	Melt spinning	Ribbon, ~100	2.40	2.92	Mg-Mg 3.20 Mg-Zn 2.98 Mg-Ca 3.57	Mg-Mg 2.72 Mg-Zn 2.61 Mg-Ca 3.10	
$La_{65}Al_{14}(Cu_{5/6}Ag_{1/6})_{11}Ni_5Co_5$ [154]	Copper mold casting	Bulk	2.87	3.51	La-La 2.76 La-Al 2.81 La-Cu 2.66	La-La 2.50 La-Al 2.43 La-Cu 2.42	La-La 3.76 [154] La-Al 3.31 La-Cu 3.16
$Zr_{44}Ti_{11}Cu_{10}Ni_{10}Be_{25}$ (LM1b) (Liquidmetal Technologies, Inc.)	Copper mold casting	Bulk	2.39	2.91	Zr-Zr 3.20 Zr-Ti 3.05 Zr-Be 2.72	Zr-Zr 2.90 Zr-Ti 2.77 Zr-Be 2.35	
$Cu_{46.6}Zr_{53.4}$	Magnetron sputtering	Film, 3.58	2.36	2.87	Cu-Cu 2.56 Cu-Zr 2.88 Zr-Zr 3.20	Cu-Cu 2.34 Cu-Zr 2.62 Zr-Zr 2.90	For $Cu_{50}Zr_{50}$ [155]: Cu-Cu 2.53 Cu-Zr 2.75 Zr-Zr 3.15 For $Cu_{57}Zr_{43}$ [156]: Cu-Cu 2.65 Cu-Zr 2.80 Zr-Zr 3.15
$Cu_{49.3}Zr_{50.7}$	As above	Film, ~3.5	2.34	2.85			
$Cu_{53.8}$ $Zr_{46.2}$	As above	Film, 3.57	2.28	2.79			
$Cu_{59.7}Zr_{40.3}$	As above	Film, 4.61	2.25	2.75			
$Cu_{62.6}Zr_{37.4}$	As above	Film, ~4	2.24	2.73			

Note: In columns of R_{m}, R_{c}, and Exp., only dominant bonding types are given for comparison.

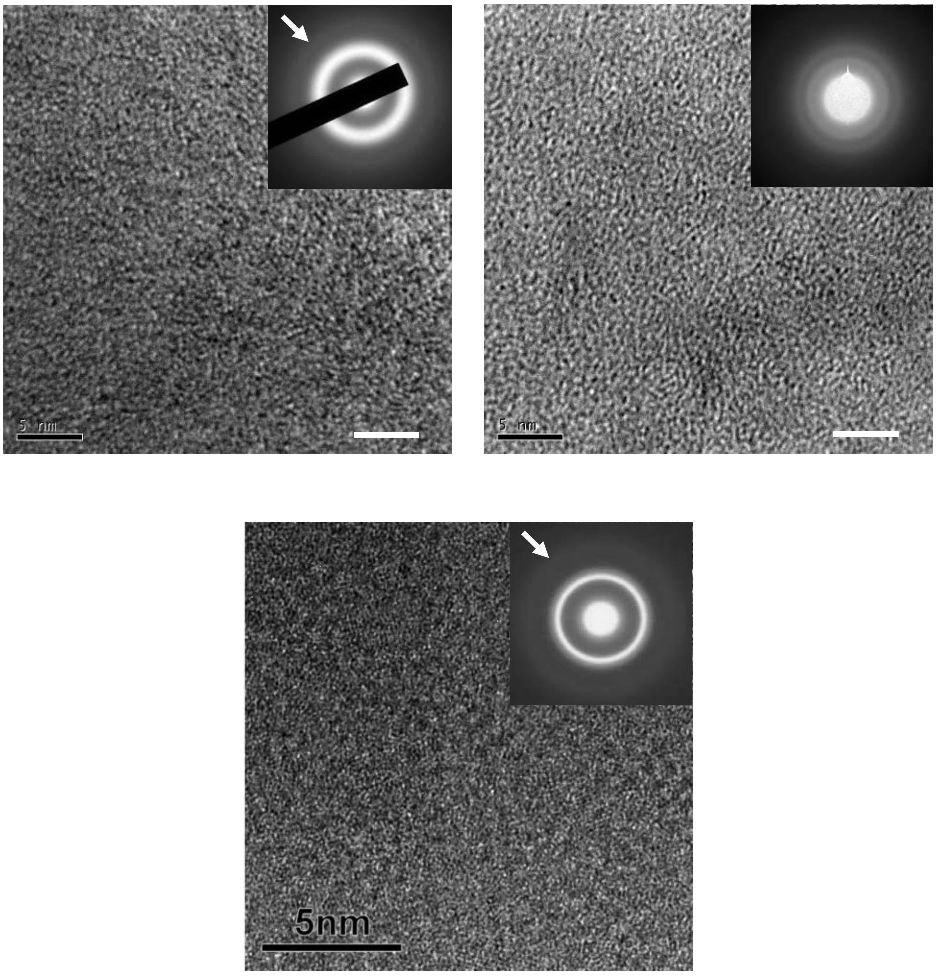

Figure 3.8 TEM images for (a) a CuZr thin film by sputtering at a DC power of 100 W, (b) a CuZr thin film by co-sputtering at a DC power of 250 W for CuZr target and a RF power of 50 W for Cu target, and (c) an as-quenched $Al_{85}Ni_5Y_8Co_2$ ribbon (courtesy of H. W. Yang [151]). Insets show the corresponding SAED patterns. The white arrow indicates a second amorphous ring which could be related to medium-range order. The white scale bar represents 5 nm.

3.4.2 Molecular dynamics simulation

The work in this section has been published in [157].

3.4.2.1 ***Simulation method***

A starting configuration of 2592 atoms is constructed with a crystalline structure (B11) and density (6.25 g/cm^3). The configuration has a size of $3\times3.3\times3.9$ nm^3 and the atoms are divided equally into Cu and Ti. Calculations are carried out under the ensemble of NPT with number of particles N, pressure P (P=0 throughout the simulation) and temperature T constant. The equations of motion are solved by a fifth-order Gear's predictor-corrector algorithm with a time step size of 5 fs. Velocity scaling method controls the temperature at every time step. Periodic boundary conditions are applied along the three Cartesian axes. The cutoff distance used in the force calculation is 10 Å, which is two times smaller than the edge length of the simulation box and thus avoids the interaction between the origin and image atoms. To capture the structural evolution and the amorphous structure as well, the liquid quench process is employed. The liquid state is achieved by directly equilibrating the initial crystalline configuration at the melt temperature of 2000 K for 12.5 ps (2500 time steps). Such heating temperature is much higher than the melting point of $Ti_{50}Cu_{50}$ compound (1255 K) and allows for the homogeneous liquid state. Then the system is cooled down continuously to 298 K at a cooling rate of 17 K/ps, followed by an equilibration run at 298 K for 12.5 ps. The equilibrated structure takes a volume of approximately $3.1\times3.2\times3.9$ nm^3. Atomic structure is characterized by Voronoi tessellation which separates 3D space into Voronoi cells, the analog of Wigner-Seitz cells in crystalline materials. Hence, one configuration can be distinguished from another through Voronoi index $<n_3, n_4, n_5,$

n_6, …>, where n_i stands for the number of *i*-edged faces of a Voronoi cell and Σn_i is the total CN.

3.4.2.2 Structural evolution

The total and partial RDFs from 2000 K to 300 K are both given in Fig. 3.9. The first maximum peak positions correspond to the nearest interatomic distances. As the temperature decreases , the first maximum peaks in all RDF patterns shift step by step to the right but the first minimum step by step to the left. For example, the first neighboring distances from 2000 K to 300 K in the total RDFs are respectively 0.266, 0.266, 0.268, 0.268, 0.268, 0.269, and 0.269 nm. The reduced first neighboring distances reveal that the nearest interatomic action becomes stronger with increasing temperature due to the weakening effect from atoms in the next neighboring shells. The damping intensity and broadening of the first peak both shows that the system appears more and more disordered at a higher temperature. These phenomena mentioned have been verified in experiments [45, 46]. The CNs in the first shell of all states at different temperatures are calculated by integrating the first peak over a defined distance region. It is found that they have quite similar CNs ranging between 12 and 13 (see Table 3.2).

Table 3.2 The local structural parameters in the first shell of all states

	Temperature (K)						
	300	500	700	900	1200	1500	2000
First peak position (nm)	0.269	0.269	0.268	0.268	0.268	0.266	0.266
First minimum (nm)	0.355	0.360	0.365	0.370	0.370	0.370	0.380
Coordination number	12.5	12.5	12.8	12.9	12.8	12.6	12.7

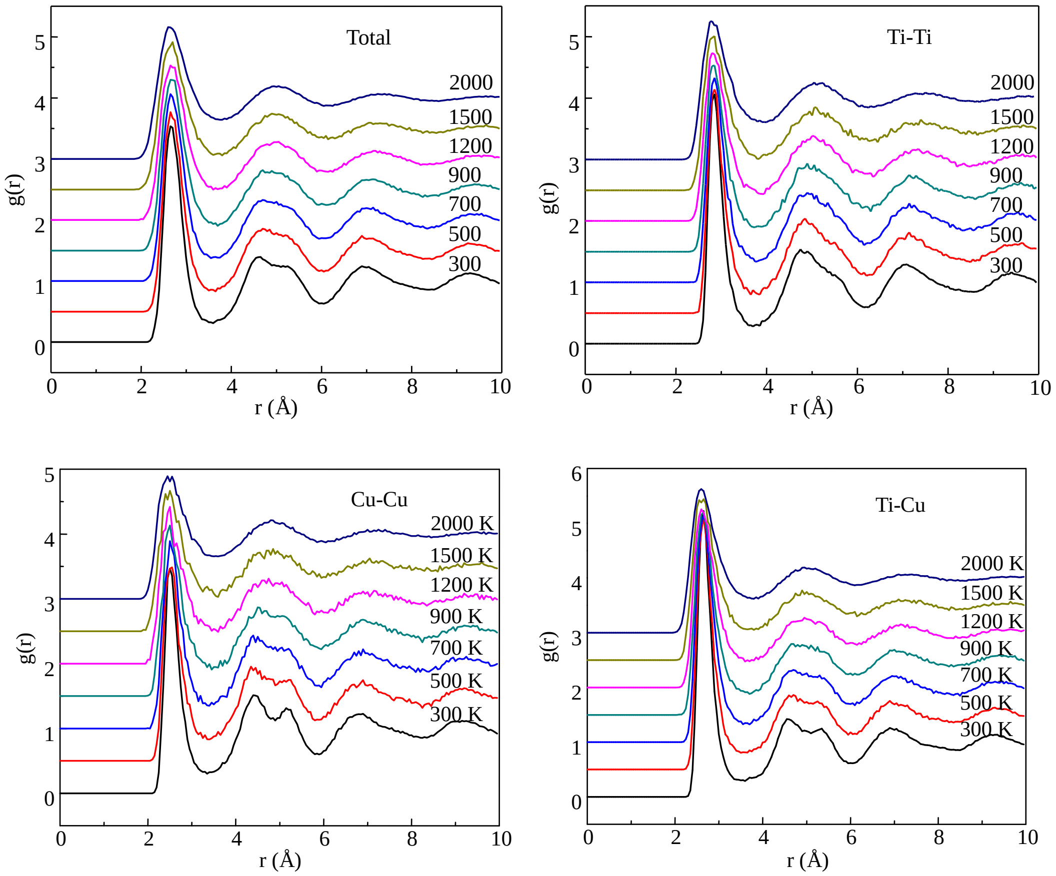

Figure 3.9 Total and partial RDFs of $Ti_{50}Cu_{50}$ at different temperatures.

The second RDF peak is worth noting because it also involves useful information about the structural evolution. Obviously, as temperature drops, the shape of the second peak changes from a smooth feature to that of having a shoulder. The transition temperature is around 900 K where the second peak begins to split into two subpeaks. Thus, it could be said that the undercooled liquid exhibits an amorphous feature. The splitting of the second peak is considered to be a natural consequence of narrowing of the first peak [158]. Exactly, the splitting arises from the change of bonded pairs or polyhedral configurations with temperature [159].

Structural evolution contributes to the change of RDFs and structure factors with temperature. The distribution of the most commonly occurring Voronoi polyhedra at temperatures of 300 and 2000 K are shown in Fig. 3.10. Due to its sensitivity to thermal vibration and cutoff radius, the polyhedral distribution was obtained by averaging over a time period to eliminate the thermal effect. In addition, the results were compared by adopting possible cutoff radii and negligible difference was found. Unlike the crystals of this study where the CN of an atom is 14, the CNs of 12 and 13 are preferable in both liquid and glassy states. The fraction of polyhedra with CN of 12 increases by about 5% from 2000 to 300 K, and that of the others does not change much. Such a distribution is not unique and has been discovered in a number of amorphous metallic systems [11, 160, 161]. It should be noted that even though $Ti_{50}Cu_{50}$ is a weak glass former it exhibits a very similar polyhedral distribution to the bulk MGs.

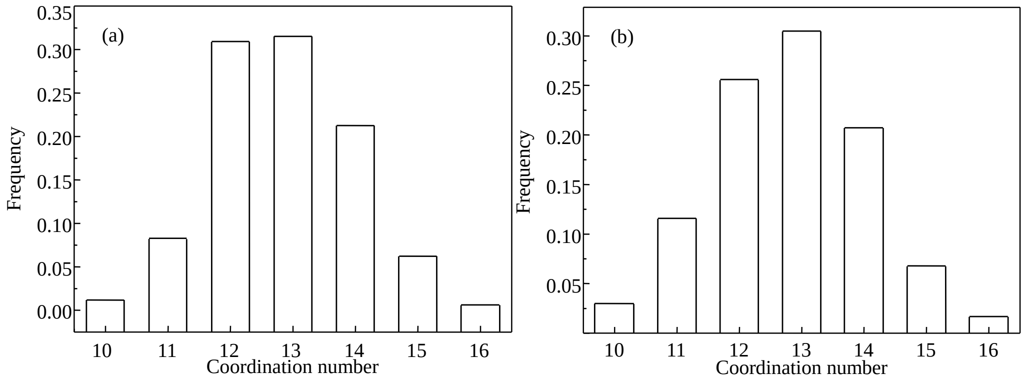

Figure 3.10 Polyhedral distribution at temperatures of (a) 300 K and (b) 2000 K.

Because the configurations with CNs of 12 and 13 are both the dominant types, their variation with temperature is presented in Fig. 3.11, where other polyhedra with population lower than 1% are neglected. Interestingly, some polyhedral types appear to be sensitive to temperature, and some not. In Fig. 3.11a, the icosahedral type <0, 0, 12, 0> has a rather low fraction of around 1% at 2000 K, which is often believed to be the major component consisting of the amorphous structure in MGs. As the temperature decreases, its number frequency grows slowly in the liquid region and then rapidly in the supercooled liquid region. At the glassy region, the frequency approaches a constant of about 8%. Similarly, the structural evolution happens to the polyhedral types <0, 2, 8, 2>, <0, 1, 10, 2>, and <0, 2, 8, 3>. Such configurational development on cooling has been reported elsewhere [48, 162]. It is worth noting that besides <0, 0, 12, 0> those polyhedra <0, 2, 8, 2>, <0, 3, 6, 3>, <0, 1, 10, 2>, <0, 2, 8, 3> and <0, 3, 6, 4> are also common in MGs. <0, 2, 8, 2>, <0, 1, 10, 2> and <0, 2, 8, 3> can be regarded as distorted icosahedra [163], whereas <0, 3, 6, 3> and <0, 3, 6, 4> are distorted bcc polyhedral [164]. The polyhedral type <0, 3, 6, 4> increases gradually in amount from about 6% at 2000 K to about 11% at 300 K, a little larger than the fractions of the other polyhedra except <0, 2, 8, 2> at 300 K, indicating that the model prefers to form bcc clusters which are favorable in the crystalline compound of $Ti_{50}Cu_{50}$. By easy summation the total fractions of icosahedron- and bcc-like configurations are 33% and 16%, respectively. Hence, the amorphous structure of $Ti_{50}Cu_{50}$ is mainly comprised of icosahedral and bcc clusters. The popularity of icosahedral clusters in amorphous $Ti_{50}Cu_{50}$ is attributed to the accompanying reduced potential energy. As temperature drops at a very rapid cooling rate, the nucleation and crystallization are both hindered. Structural rearrangement is needed to release the excess potential energy. Icosahedron has long been recognized as a stable structure in supercooled liquids [165]. Recently, Iwamatsu and Lai [166] employed a minimization technique to determine the lower-energy structures of isolated 13-atom binary clusters and found that the icosahedral clusters are favored conditionally. It should be addressed that the relatively large portion of the other polyhedra other than full icosahedra could also be responsible for the poor glass forming ability of the present model because these distorted configurations are considered to facilitate the atomic mobility while the full icosahedra slow down the atomic dynamics [48].

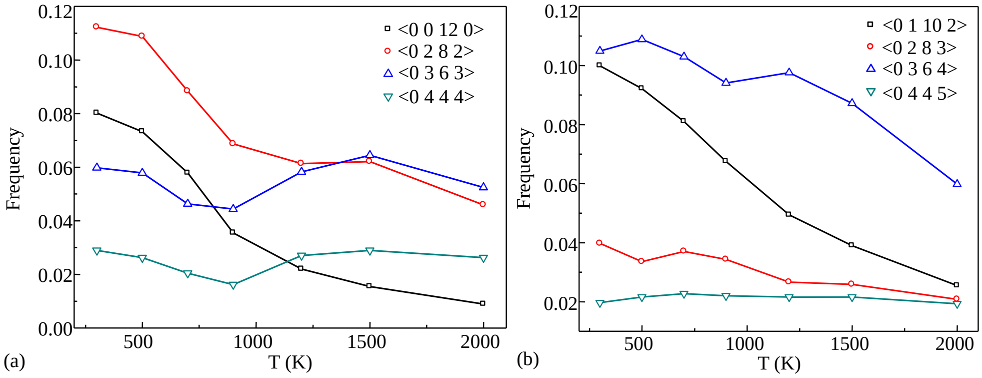

Figure 3.11 Configurational evolution with temperature. (a) CN=12 and (b) CN=13.

To understand the structural evolution in depth and also confirm the modelling result, the total structure factors are calculated after sine fourier transformation of the total RDFs. The transformation equation is given below:

$$S(q)-1=n\int_{0}^{\infty}4\pi r^{2}\left[g(r)-1\right]\frac{\sin qr}{qr}\,\mathrm{d}r \tag{3.15}$$

where q is the scattering factor, n is the average number density and $g(r)$ is the RDF at the distance r. The pattern of structure factors looks very similar to that of RDFs and is not shown here. The structure factor is related to temperature in harmonic approximation by the Debye-Waller factor, $W_T(q)$, a quantity describing the thermal effect on scattering [167, 168]:

$$S_{\mathrm{T}}(q)=1+\left[a(q)-1\right]\exp\left[-2W_{\mathrm{T}}(q)\right] \tag{3.16}$$

$$W_{\mathrm{T}}(q)=\frac{3\hbar^2 q^2 T^2}{2m k_{\mathrm{B}}\Theta^3}\int_0^{\Theta/T}\left(\frac{1}{2}+\frac{1}{e^z-1}\right)z\mathrm{d}z \tag{3.17}$$

where $\hbar$ is the reduced Planck constant, m is the atomic weight, Θ is the Debye temperature. For $T>>\Theta$, $S(q)$ varies with temperature in an approximately linear way. The above equation can be used to estimate the Debye temperature in amorphous solid. In doing so, the $W_{\mathrm{T}}(q)$ equation is simplified by replacing e^z with $(1+z)$ according to the Taylor's expansion. The reduced form of $W_{\mathrm{T}}(q)$ is

$$W_{\mathrm{T}}(q)=\frac{3\hbar^2 q^2 T}{2m k_{\mathrm{B}}\Theta^2} \tag{3.18}$$

Finally, based on the above equations, the solution to the Debye temperature is given from

$$\ln\frac{S_{\mathrm{T}_2}(q)-1}{S_{\mathrm{T}_1}(q)-1}=-\frac{3\hbar^2 q^2}{m k_{\mathrm{B}}\Theta^2}(T_2-T_1) \tag{3.19}$$

The parameters used for calculation of the Debye temperature are provided in Table 3.3. The choice of temperature is to make sure the ratio of Θ/T small enough (<1). The q values are adopted around the first maximum of $S(q)$. The estimated Debye temperature is (296±41) K for the glass and (206±14) K for the supercooled liquid. The former is very close to the experimental value of (296.6±4.0) K [169]. If more q points are examined, it is no doubt that the estimated value deviates but not too much from the experimental one. Then, choosing Θ=206 K, T_1=300 K, the $S(q)$ at T_2=900 K is calculated. The patterns are plotted in Fig. 3.12. The good matching between the calculated and Fourier transformed $S(q)$ increases the confidence in the simulation results.

Table 3.3 Parameters for determination of the Debye temperature

m (kg/mol)	Tepermature (K)	300	500	700	900	1200
	Scattering vector *q* (nm^{-1})	Structure factor *S* (nm^{-1})				
55.707	28	34.5274	33.8203	32.8265	31.0579	28.4676
	29	35.4551	33.9093	32.2406	29.7796	26.5171

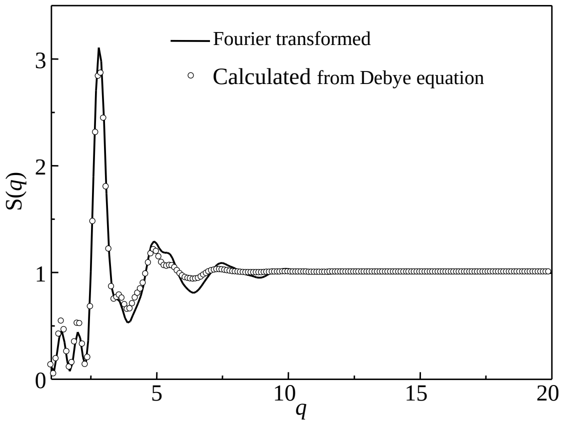

Figure 3.12 Comparison between structure factors Fourier transformed (line) and calculated from Debye equation (circle).

The changing behavior of $S(q)$ with temperature is also similar to that of $G(r)$. Shown in Fig. 3.13 is the temperature dependence of scattering vector and structure factor at the first maximum peak. The scattering factor decreases linearly from room temperature up to the melting temperature, which is attributed to the thermal expansion without structural change [45]. The height of the first maximum is sensitive to the state transition. The glass transition and melting temperature can be easily recognized from the pattern in Fig. 3.13b. What causes the change of the height is the structural disorder in the quenching process. The embedded picture in Fig. 3.13b clarifies the change of the first peak intensity with temperature.

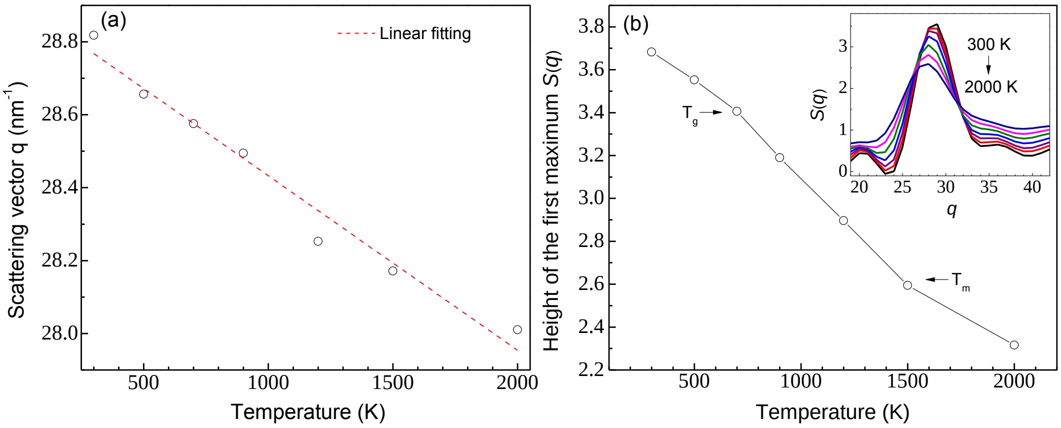

Figure 3.13 Temperature dependence of (a) scattering vector at the first maximum peak and (b) height of the first maximum of structure factor. Inset in (b) are the first maximum peak patterns of *S*(*q*) in an order from 300 K at the top to 2000 K at the bottom.

3.4.2.3 Atomic structure

The efficient cluster packing (ECP) model developed by Miracle [26] has been employed to describe the short-to-medium range order of bulk MGs. The concept of cluster is helpful to understand the atomic structure of amorphous $Ti_{50}Cu_{50}$. It should be noted that the amorphous cell for structural analysis is obtained from the previous work [170] and consists of 576 atoms. Nevertheless, RDF analysis confirms the structural similarity of both models. Given in Fig. 3.14a-c are a few typical polyhedral units present in the amorphous model with corresponding Voronoi cell inside. Connection of atoms is defined by a cutoff distance corresponding to the first minimum in the total RDF. It is evident that, unlike the crystalline unit, there exist a variety of polyhedral configurations. Such abundance is not unique and has been found in many other MGs [9, 28, 171, 172]. The irregular geometrical characteristics indicate the non-efficient atomic packing in the amorphous model.

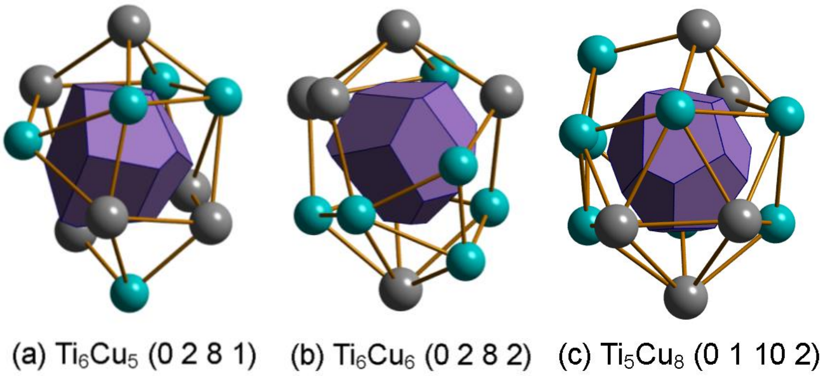

Figure 3.14 Representative polyhedral configurations extracted from the amorphous model of $Ti_{50}Cu_{50}$ in this study. From (a) to (c), the coordination numbers are respectively 11, 12, and 13. The connection of atoms by solid lines indicates close contact of atoms.

The distribution patterns of atomic configurations in Fig. 3.15 are obtained manually by sampling 80 Cu and 80 Ti atoms, respectively. It is manifest that they prefer CNs of 12 and 13. The polyhedral configurations around Cu atoms tend to have a smaller CN than those around Ti atoms, which is due to its atomic size. The smaller the atomic size, the less space for acceptance of atoms and thus lower the CN. The cluster packing is shown in Fig. 3.16. These clusters connect by vertex-, edge- and face-sharing and form a five-fold symmetry [28]. The symmetry can be regarded as medium range order. The average distance between clusters is 0.45 nm about two times as much as the periodic length in the total RDF, confirming the applicability of cluster packing to the present amorphous model.

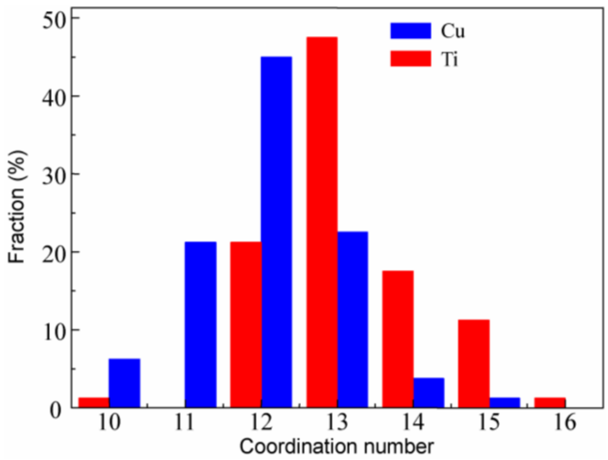

Figure 3.15 Distribution of polyhedral configurations around Ti and Cu atoms in amorphous $Ti_{50}Cu_{50}$.

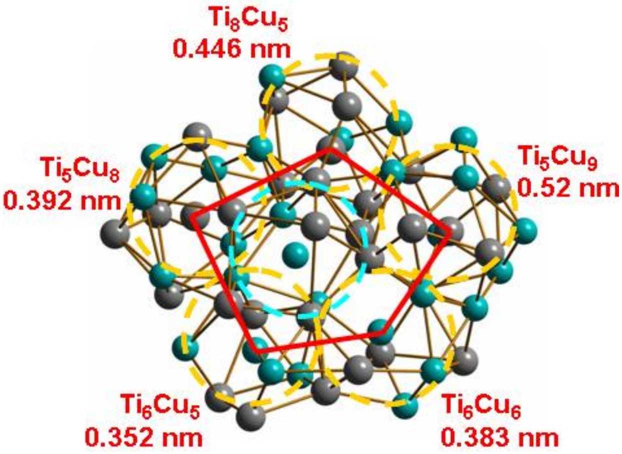

Figure 3.16 Packing of polyhedral clusters shows an approximate five-fold symmetry. The central cluster is circled in light blue and the neighbors are circled in yellow. The blue and grey balls stand for Cu and Ti atoms, respectively. The clusters and the distance from neighoring clusters to central one are also given.

3.5 Thermal properties by non-isothermal DSC

Fig. 3.17 gives the representative non-isothermal DSC curves at various heating rates for six compositions. It is known that amorphous alloys are thermodynamically metastable phases and would transform to a more thermally stable phase under external conditions such as heat. As illustrated in the inset of Fig. 3.17a, amorphous alloys generally undergo three transition regions before crystallization: structural relaxation, glass transition and supercooled liquid. Structural relaxation (SR) emits heat, which is attributed to an elementary relaxation process termed β-relaxation [41]. This process corresponds to configurational hopping between neighboring basins [41]. Glass transition, which is characterized by the rapid but continuous change in heat capacity, starts at the temperature T_{gs} and ends at the temperature T_{ge}. The supercooled liquid region (SLR, $\Delta T_x=T_x-T_{gs}$), retains liquid features below the freezing point and compared to SR, involves additional relaxation process termed α-relaxation occurring between contiguous metabasins [41]. The SLR is interrupted at the point T_x where crystallization starts off and the transformation rate reaches the maximum at the peak point T_p. All the data are tabulated in Table 3.4.

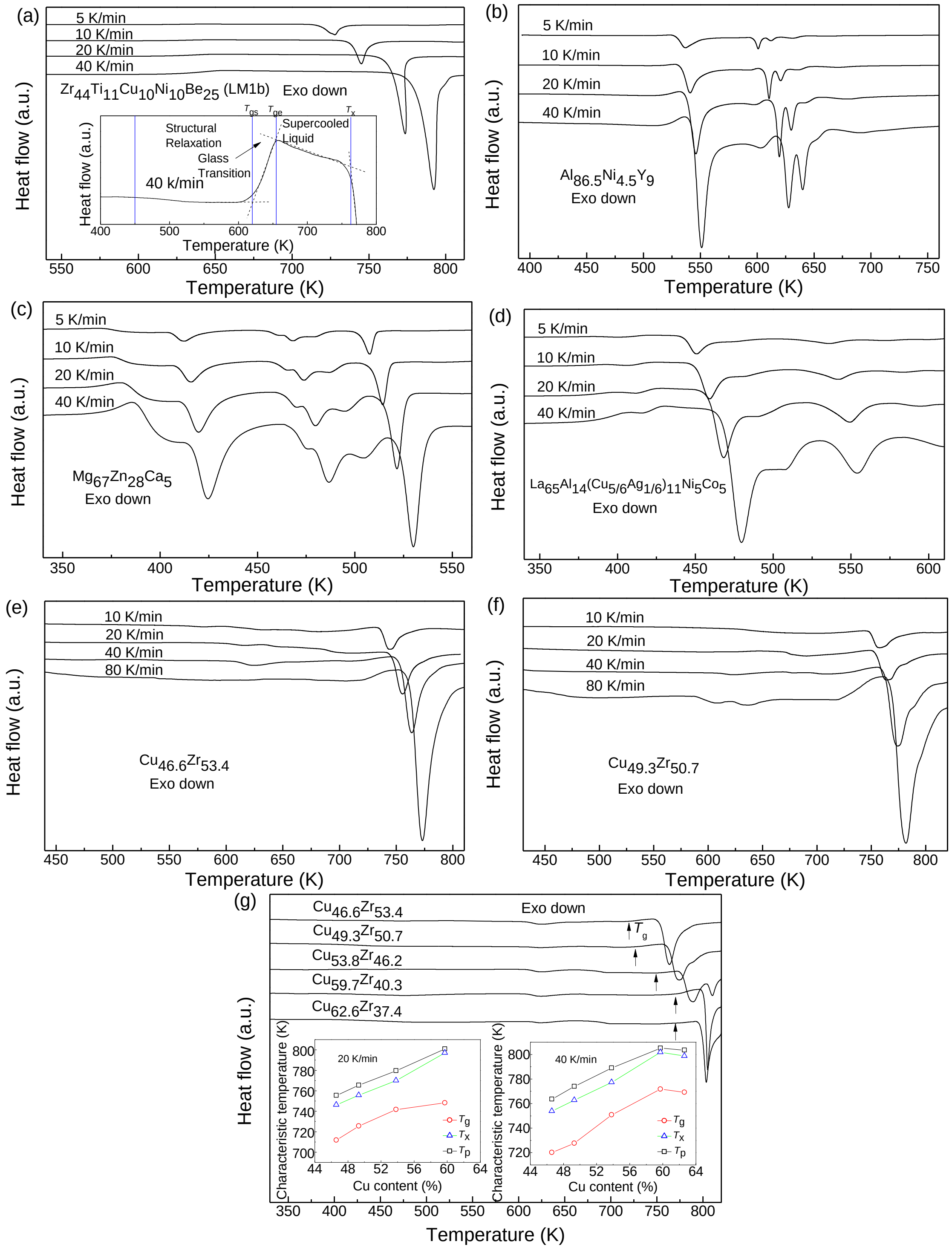

Figure 3.17 Continuous DSC profiles at various heating rates for (a) $Zr_{44}Ti_{11}Cu_{10}Ni_{10}Be_{25}$ (Inset: three regions are typically identified when MGs are being heated), (b) $Al_{86.5}Ni_{4.5}Y_9$, (c) $Mg_{67}Zn_{28}Ca_5$, (d) $La_{65}Al_{14}(Cu_{5/6}Ag_{1/6})_{11}Ni_5Co_5$, (e) $Cu_{46.6}Zr_{53.4}$, and (f) $Cu_{49.3}Zr_{50.7}$. (g) Cu_xZr_{100-x} thin films at 40 K/min (Inset: transformation temperatures as a function of Cu content at heating rates of 20 and 40 K/min. They increase with an increase in Cu content.)

The glass transition temperature (i.e., T_{gs} if without specifying because T_{ge} cannot be usually identified) and the width of the SLR are two useful quantities for characterizing the thermal stability of MGs, i.e., the larger the quantities and the more stable the glasses. Fig. 3.18 shows their correlation and dependence on heating rates. Clearly, increase in one quantity generally implies increase in another quantity, and the extent of increase varies across glass compositions. Both T_{gs} and ΔT_x increase as the heating rate increases, which can be described by a logarithmic equation. Based on Table 3.4, T_{gs} within the range of heating rate investigated here changes by 9–30 ℃ (sequentially in $Al_{86.5}Ni_{4.5}Y_9$ and $Cu_{59.7}Zr_{40.3}$), showing that glass transition is somewhat sensitive to heating rate. It has been reported that, however, T_g is weakly dependent upon cooling rate [41, 173]. This discrepancy might suggest that heating and cooling processes are not exactly equivalent. Notwithstanding, the primary mechanism for heating/cooling rate dependence of T_g should be the same: the faster the rate, the shorter the time available for atomic diffusion and configurational sampling.

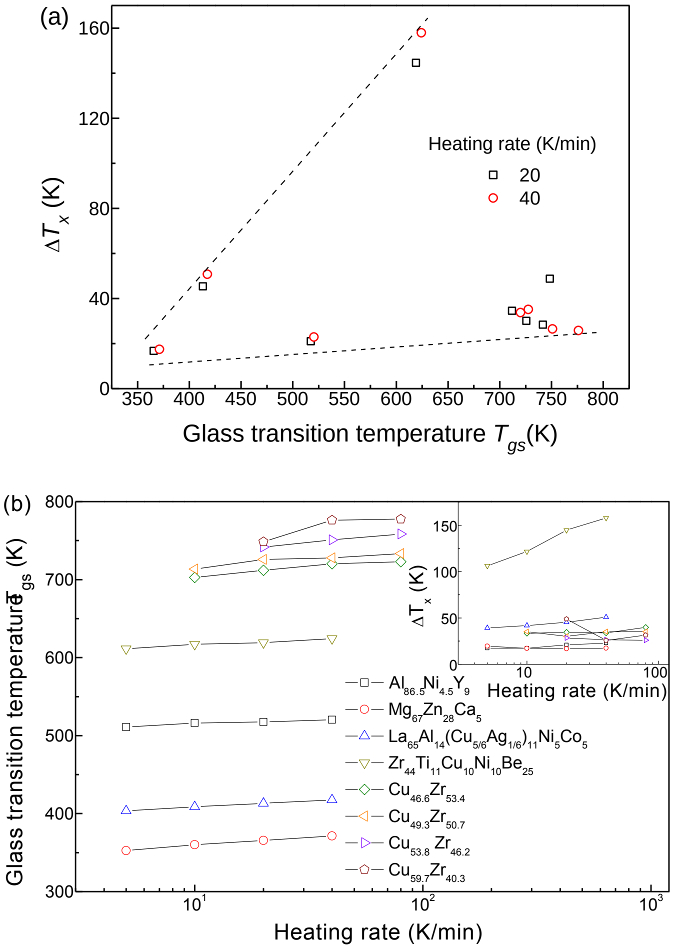

Figure 3.18 (a) The relationship between the width of SLR ΔT_x and glass transition temperature T_{gs}. (b) Glass transition temperature T_{gs} as a function of heating rate.

Fig. 3.19a illustrates the heat enthalpy ΔH_x at first crystallization as a function of heating rate. ΔH_x is defined herein as the amount of heat released or absorbed by the material per unit mass during crystallization. For most compositions, ΔH_x exhibits no strong dependence on heating rate, while for $Zr_{44}Ti_{11}Cu_{10}Ni_{10}Be_{25}$ (LM1b), ΔH_x increases with an increase in the heating rate.

Table 3.4 Summary of thermal properties for nine amorphous compositions surveyed. T_{gs}, T_{ge}, T_x and T_p respectively stand for glass transition temperatures at the onset and end, first crystallization temperatures at the onset and peak. ΔT_g, ΔT_x, and ΔH_x are temperature intervals for glass transition, supercooled liquid region, and heat of first crystallization, respectively. m_{cs} and m_{ce} are the fragility indices at the onset and end of glass transition, respectively.

Composition	Heating rate (K/min)	T_{gs} (K)	T_{ge} (K)	T_x (K)	T_p (K)	ΔT_g (K)	ΔT_x (K)	m_{cs} (Eq. 3.24)	m_{ce} (Eq. 3.24)	m_{cs}* (Eq. 3.23)	m_{ce}* (Eq. 3.23)	ΔH_x (J/g)
$Al_{86.5}Ni_{4.5}Y_9$	5	511.01		528.48	536.87		17.47	49.27				52.45
	10	516.03		533.45	540.83		17.42	48.79				51.35
	20	517.4		538.36	546.02		20.96	48.66				49.2
	40	520.4		543.31	550.98		22.91	48.38				47.75
$Mg_{67}Zn_{28}Ca_5$	5	352.54		372.08			19.54	17.01				28.65
	10	359.99		377.15			17.16	16.66				27.96
	20	365.71		382.4			16.69	16.4				28.14
	40	371.29		388.66			17.37	16.15				28.48
$La_{65}Al_{14}(Cu_{5/6}Ag_{1/6})_{11}Ni_5Co_5$	5	403.61	418.5	442.67	451.06	14.89	39.06	26.15	39.32	31.3	60.3	10.42
	10	408.63	420.79	450.31	459.29	12.16	41.68	25.83	39.1			9.957
	20	413.23	424.52	458.62	468.16	11.29	45.39	25.54	38.76			9.63
	40	417.55	427.85	468.25	479.64	10.3	50.7	25.27	38.46			9.968
$Zr_{44}Ti_{11}Cu_{10}Ni_{10}Be_{25}$ (LM1b)	5	611.23	638.08	717.31	727.89	26.85	106.1	45.77	41.31	39.2	42.1	66.16
	10	617	642.66	738.26	745.01	25.66	121.53	45.36	41.02			63.43
	20	619.2	646.91	764.25	773.59	27.71	144.57	45.14	40.75			71.34
	40	624.28	652.15	781.21	792.18	27.87	157.82	44.87	40.42			85.44

$Cu_{46.6}Zr_{53.4}$	10	702.67		736.03	744.59		33.36	29.14	40.57
	20	711.85		746.4	755.58		34.55	28.77	40.6
	40	720.22		753.98	763.74		33.76	28.43	36.26
	80	722.87		762.77	773.19		39.9	28.33	40.94
$Cu_{49.3}Zr_{50.7}$	10	713.59		748.68	757.41		35.09	31.61	30.22
	20	725.65		755.67	765.49		30.02	31.08	40.04
	40	727.77		762.93	774.02		35.16	30.99	33.39
	80	733.32		768.46	781.06		35.14	30.76	35.47
$Cu_{53.8}$ $Zr_{46.2}$	20	741.7		770.04	779.64		28.34	26.25	37.23
	40	750.96		777.38	789.16		26.42	25.92	41.61
	80	758.46	766.44	784.48	797.41	7.98	26.02	25.67	31.76
$Cu_{59.7}Zr_{40.3}$	20	748.48	765.7	797.25	801.04	17.22	48.77		32.97
	40	776.1	786.22	801.86	805.19	10.12	25.76		33.68
	80	777.62	794.4	808.96	813.13	16.78	31.34		34.26
$Cu_{62.6}Zr_{37.4}$	40	769.19		798.76	803.62		34.43		

Shown in the inset of Fig. 3.19a are the first crystallization peaks for four compositions. Zr-based sample has a scanning peak with a steeper rising edge on the low-temperature side than on the high-temperature side, while the other compositions are the other way around. In addition, compared to the other compositions, Zr-based sample has a relatively smaller peak width. This unique shape may be related to its unique crystallization process [174], which accounts for the unique behavior of ΔH_x in Zr-based sample. Interestingly, referring to Fig. 3.18b, it is found that Zr-based sample has a noticeable increase in the width of SLR with an increase in heating rate, in coincidence with the increase of ΔH_x. Fig. 3.19b shows that ΔH_x increases with an increasing T_{gs}, implying that it can also be used to characterize the thermal stability of MGs.

A number of models have been well established to understand the crystallization kinetics during non-isothermal DSC, among which the Kissinger equation is most popular. The applicability of the Kissinger analysis has been justified theoretically for nucleation-and-growth and grain growth [174, 175]. This equation is formulated as:

$$\ln\left(\frac{R_h}{T^2}\right) = -\frac{E_a}{RT} + \text{constant} \tag{3.20}$$

where R_h is the heating rate, T is the characteristic temperature, E_a is the apparent activation energy for phase transformations, R is the gas constant. It is unambiguous that the logarithmic term $\ln(R_\mathrm{h}/T^2)$ is proportional to the inverse of temperature $1/T$ (see Fig. 3.20, where E_g, E_x and E_p respectively stand for activation energies for glass transition, crystallization at the onset and peak). As R_h and T are both measured by performing continuous DSC tests at various heating rates, E_a is thus estimated directly as the gradient of the fitting straight-lines.

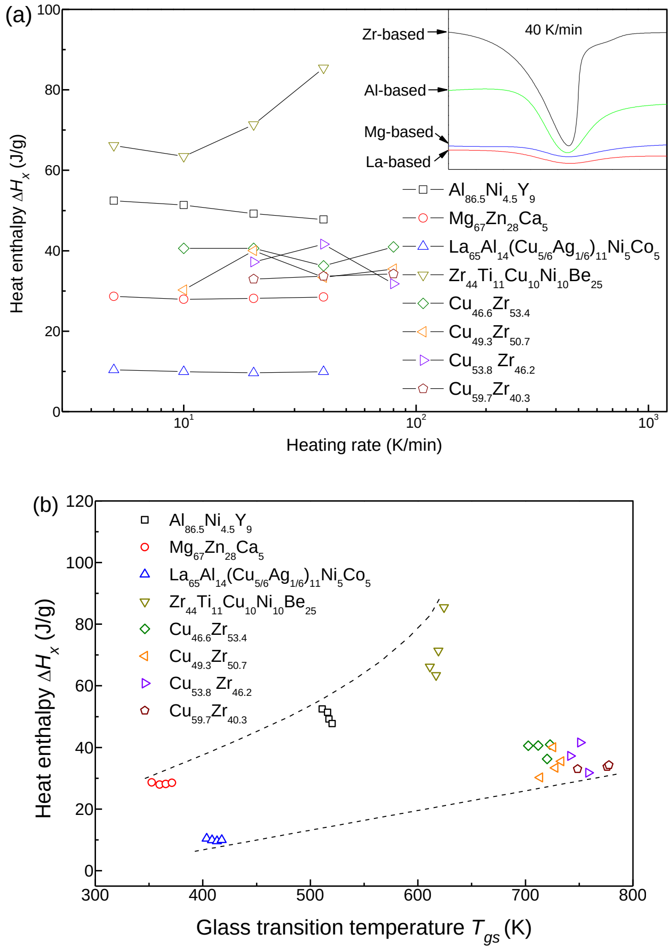

Figure 3.19 (a) Heat enthalpy of the first crystallization ΔH_x as a function of heating rate. Inset: peak shapes at the first crystallization. (b) The relationship between heat enthalpy ΔH_x and glass transition temperature T_{gs}.

It is worth noting that, although the Kissinger equation is derived for the peak temperature T_p, it is also applicable to the analysis of the shift of the onset points for glass transition (T_g) and crystallization (T_x). By comparing the activation energies among the compositions investigated, it can be seen that, for the Zr-based sample, the activation energies at the onset and peak crystallization are far lower than at the onset of glass transition. This large departure, again, appears to correspond to the marked increase of ΔH_x in Fig. 3.19a.

A quantity termed fragility index, *m*, is an important material constant which has been revealed to connect with other glass properties, such as glass-forming ability [176, 177], bulk modulus/the ratio of bulk modulus to shear modulus [178], and Poisson's ratio/plasticity [177]. It was initially introduced to quantify the fragility behavior of supercooled liquids which experience a rapid increase in kinetic properties (i.e., viscosity/relaxation time) as temperature drops from the melting point, T_m, to the glass transition point, T_g. The variation of kinetic properties with temperature generally follows the description of the Vogel–Fulcher–Tamman (VFT) equation [179]:

$$\tau = \tau_\infty \exp\left(\frac{A}{T_g - T_o}\right) \tag{3.21}$$

where τ represents the relaxation time at a temperature in the supercooled liquid regime. τ_∞, A and T_o are fitting parameters. Within a narrow temperature region, especially near T_g, Eq. 3.21 can be simplified into the Arrhenius form by giving T_o=0:

$$\tau = \tau_\infty \exp\left(\frac{E_a}{T_g}\right) \tag{3.22}$$

Based on Eq. 3.21, the fragility index *m* is obtained as the steepness of the curve of log(τ) vs T_g/T at T_g:

$$m = \left.\frac{d\log\tau}{d(T_g/T)}\right|_{T=T_g} = \frac{AT_g}{(T_g - T_o)^2 \ln 10} \tag{3.23}$$

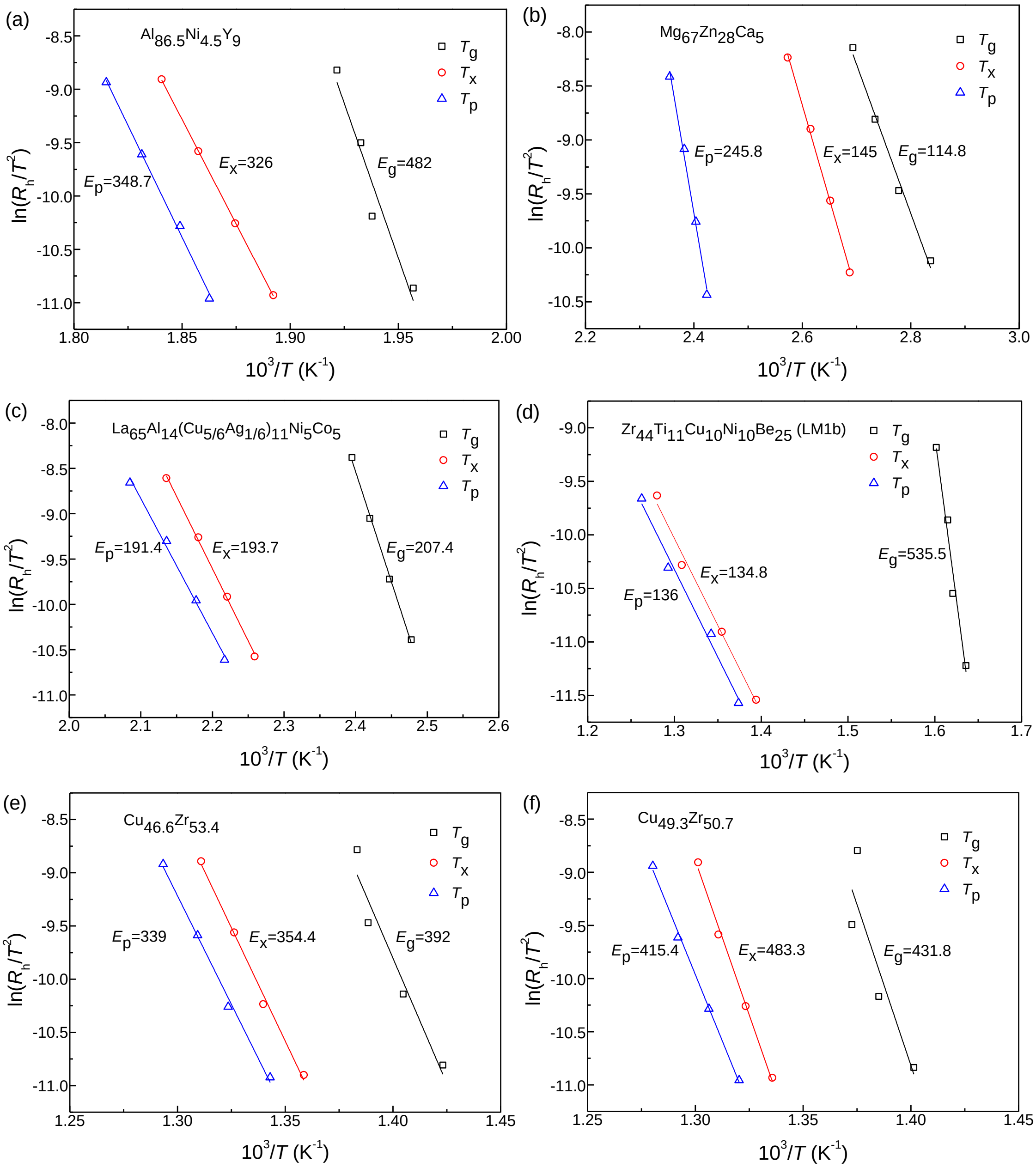

Figure 3.20 Kissinger plots for (a) $Al_{86.5}Ni_{4.5}Y_9$, (b) $Mg_{67}Zn_{28}Ca_5$, (c) $La_{65}Al_{14}(Cu_{5/6}Ag_{1/6})_{11}Ni_5Co_5$, (d) $Zr_{44}Ti_{11}Cu_{10}Ni_{10}Be_{25}$, (e) $Cu_{46.6}Zr_{53.4}$, and (f) $Cu_{49.3}Zr_{50.7}$. The unit for activation energy is J/mol.

and based on Eq. 3.22, the fragility index *m* is written as:

$$m = \frac{E_a}{RT_g \ln 10} \tag{3.24}$$

Obviously, larger index means higher fragility, i.e., the supercooled liquids deviate to a greater extent from the Arrhenius-type behavior. By this index, glass-forming liquids are classified into three types: strong ($16 \leq m < 30$), intermediate and fragile ($m \geq 100$) [180]. It should be noted that Eq. 3.24 is equivalent to Eq. 3.23 only if the supercooled liquids exhibit temperature dependence in a Arrhenius-type fashion, where E_a will hold constant over the whole temperature range. As m is related to T_g, which depends on heating rate, T_g should not be arbitrarily chosen. Generally, T_g is defined as the temperature where the relaxation time τ reaches 100 s [179]. When non-isothermal DSC is carried out to derive the fitting parameters in Eqs. 3.23 and 3.24, there exist two glass transition temperatures, T_{gs} and T_{ge}. Senkov and Miracle [181] have suggested that T_{ge} should be used because it corresponds to a supercooled liquid state. Taking into account the various definitions of T_g, the values for m are estimated and tabulated in Table 3.4.

Fig. 3.21 illustrates the temperature dependence of relaxation time at the onset and end temperatures of glass transition, which can be well fitted with the VFT equation (the fitting parameters are included in the figures). The relaxation time for glass transition is defined as $\tau=(T_{ge}-T_{gs})/R_h=\Delta T_g/R_h$. For compositions which do not have an observable SLR, T_{ge} is not identifiable and thus the temperature-dependent relaxation behavior is not plotted. Looking at Table 3.4, ΔT_g for the La- and Zr-based alloys is in fact not always constant but has a small change with an increase in heating rate, i.e., for the La-based, it decreases, while for the Zr-based, it increases. As pointed out by Senkov and Miracle [181], Eq. 3.24 is not applicable when ΔT_g depends on heating rate. Nevertheless, Eq. 3.23 is still valid. Using the fitting parameters, the glass transition temperature at τ=100 s is determined:

$$T_g = T_o + A/(16\ln 10) \tag{3.25}$$

T_{gs}=406.8 K and T_{ge}=420.1 K for La-based; T_{gs}=619.1 K and T_{ge}=645.6 K for Zr-based. Taking these temperatures into Eq. 3.23, the m values for the onset and end of glass transition are evaluated to be 31.3 and 60.3 for La-based alloy, and 39.2 and 42.1 for Zr-based alloy.

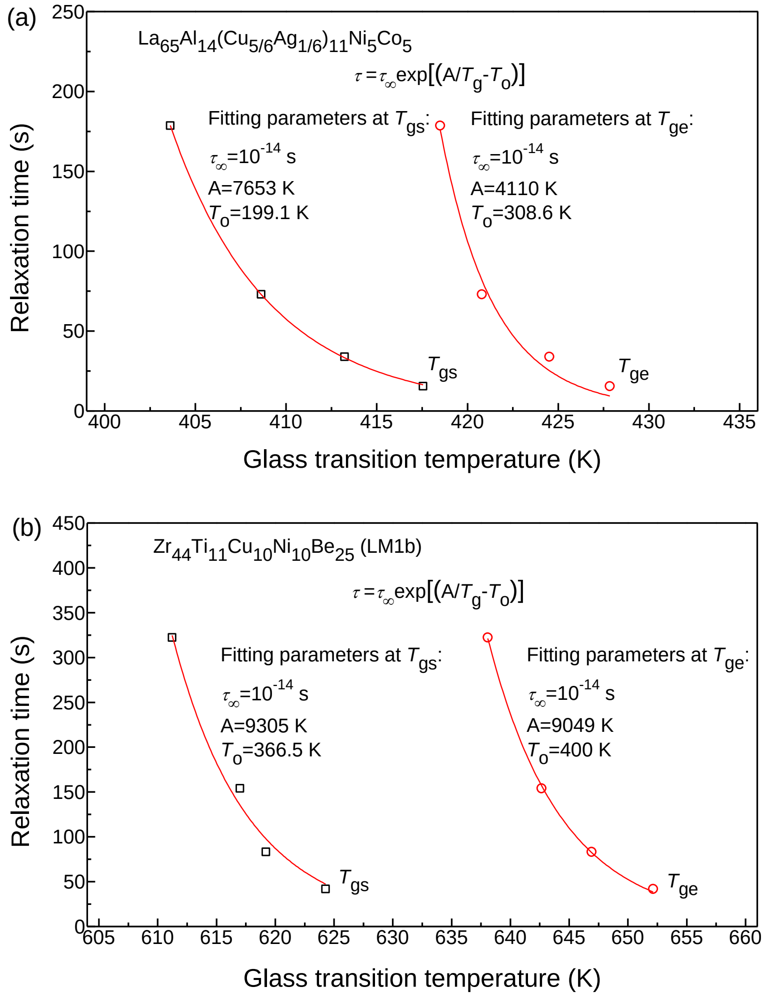

Figure 3.21 Temperature dependence of relaxation time at glass transition point for (a) $La_{65}Al_{14}(Cu_{5/6}Ag_{1/6})_{11}Ni_5Co_5$, and (b) $Zr_{44}Ti_{11}Cu_{10}Ni_{10}Be_{25}$.

3.6 Summary

The amorphous structure of MGs was investigated by experimental and computational methods. TEM imaging shows that atoms are randomly packed, while XRD and electron diffraction both indicate that there indeed exist short-to-medium-range orders. Molecular dynamics simulation confirms the existence of such order structures, and at the same time suggests that the amorphous structure consists of diverse polyhedral types, among which some types are dominant (e.g., icosahedral and bcc clusters in $Ti_{50}Cu_{50}$). These clusters form a five-fold symmetry in the medium range distance. During liquid-to-glass transition, the population of icosahedral configurations is more sensitive to temperature than that of the others, i.e., it increases as temperature decreases, which is attributed to the low-energy structure.

The thermal properties of MGs are studied by continuous DSC. For each composition, the glass transition temperature, crystallization temperature, and the width of the glass transition region unambiguously exhibit dependence on heating rate, i.e., they increase with an increase in heating rate; in contrast, the heat enthalpy at crystallization appears to be independent of heating rate except for the Zr-based sample. This exception is attributed to the unique crystallization process, which can be identified from the unique crystallization peak. Nevertheless, the larger glass transition temperatures generally correspond to the larger heat enthalpy and the wider glass transition region. Moreover, the relaxation time for glass transition of La- and Zr-based specimens is temperature dependent, which can be well fitted by the Arrhenius-type equation (Vogel–Fulcher–Tamman equation). As these thermal properties are correlated, they can be used to characterize the thermal stability and glass-forming ability of MGs.

Chapter 4 Mechanical Properties of Metallic Glasses by Nanoindentation

4.1 Introduction

In review of the literature work on MGs, the unique mechanical properties are the most topical issue. Instrumented nanoindentation is a relatively new and convenient technique with high spatiotemporal and load resolution, allowing for the fast and accurate measurement of mechanical properties of materials. This technique has been broadly used to explore the mechanical response of MGs and the pertinent structural origin. Ye *et al* [182] conducted the high frequency dynamic nanoindentation with a flat-end diamond punch and revealed the inelastic deformation of the free volume zone in the apparent elastic regime. Packard *et al* [183] discovered the cyclic hardening by applying cyclic indentation loads on MGs, which is attributed to the microplastic structural rearrangement via STZ activation. Pan *et al* [67] characterized the STZ volume and successfully associated it with ductility by performing rate-jump nanoindentation. In contrast to the work at room temperature, high-temperature nanoindentation has not yet been studied adequately [95, 96, 184, 185]. For example, Schuh *et al* [96] constructed a new deformation map according to the elevated temperature nanoindentation experiments. Li *et al* [185] investigated the nanoindentation behavior of a Au-based MG near glass transition temperature and found a transition from homogeneous flow at low loading rates to inhomogeneous flow at high loading rates in the supercooled liquid region.

This chapter starts with a viscoelastic model which addresses the existence of viscoelasticity in MGs. Subsequently, nanoindentation experiments at room and elevated temperatures are carried out to investigate the effects of loading rate, indentation size and temperature on the mechanical behaviors of MGs.

4.2 Experimental methods

Among nine amorphous compositions tested in Chapter 3, three are selected so as to study the mechanical properties of MGs. These compositions are respectively $La_{65}Al_{14}(Cu_{5/6}Ag_{1/6})_{11}Ni_5Co_5$, $Zr_{44}Ti_{11}Cu_{10}Ni_{10}Be_{25}$, and $Cu_{49.3}Zr_{50.7}$ (Table 3.1), covering a large range of glass transition temperatures. The mechanical properties are characterized by two instrumented nanoindentation systems, one for the room-temperature use and the other for the elevated-temperature use. As the elevated-temperature tests were carried out at an outside lab and the process was time-consuming, only a thin film composition was measured (i.e., $Cu_{50}Zr_{50}$ slightly different in composition from $Cu_{49.3}Zr_{50.7}$ for the room-temperature use but within the experimental error of EDX).

4.2.1 Instrumented nanoindentation

4.2.1.1 __Room-temperature nanoindentation__

Room-temperature nanoindentation was performed with a diamond Berkovich indenter on an MTS Nanoindenter® XP system. The force resolution and vertical displacement resolution are estimated to be less than 0.1 μN and 1 nm, respectively. Prior to the start of testing, the contact area function was calibrated using a standard fused silica material. The nanoindentation measurements were performed under a load-control mode and consisted of 6 sequential segments.

(1) The indenter drift rate control segment is to reach the allowable drift rate limit 0.05 nm/s. (2) The surface find segment is to identify the surface contact point. These two segments are designed to guarantee the stable and reliable measurements. (3) The loading segment reaches the preset maximum loads at various loading rates, followed by a (4) holding segment where the peak loads are kept for 2-100 s. Loads are removed in the (5) unloading segment at an unloading rate of 1 mN/s until the unload limit (10% of the peak load) was reached for all the tests. Finally, (6) thermal drift correction segment takes place where the absolute values of the thermal drift rates were usually well kept below 0.05 nm/s. The thermal drift effect was excluded from the resulting displacement data. Five indents were made in each test for statistical analysis and consistency inspection.

The hardness and the reduced elastic modulus were calculated by fitting the load-displacement (*P*-*h*) curve using the Oliver-Pharr method [186]. Specifically, the hardness was determined by the maximum load divided by the projected contact indentation area. The elastic modulus is associated with the unloading stiffness and the projected contact area. The unloading stiffness reflects the ability of surface to resist bending and equivalent to the initial gradient of the unloading curve. As the reduced elastic modulus is measured, the Young’s modulus of the material investigated can be derived as follows:

$$\frac{1}{E_r} = \frac{1-v_i^2}{E_i} + \frac{1-v^2}{E} \tag{4.1}$$

where E_r, E_i and E are respectively the reduced elastic modulus, the Young’s modulus for diamond and the Young's modulus for the test material. v_i and v are the Poisson's ratios for diamond and test material, respectively.

4.2.1.2 ***Elevated-temperature nanoindentation***

Nanoindentation experiments at the elevated temperatures were carried out using the NanoTest^{TM} (from Micro Materials, Wrexham, UK) equipped with a temperature-controlling heating stage (see Fig. 4.1). The detailed illustration of this high-temperature test configuration is available in [187]. The test temperatures were chosen as 298, 333, 363 and 393 K, respectively. To guarantee the correct measurement, the calibration procedures were taken on instrumental compliance, load, depth and contact area function at room temperature, while only the depth calibration performed at the higher temperatures. The maximum indentation depth is 400 nm, less than 10% of the film thickness in order to minimize the substrate effect. As the testing begins, a diamond Berkovich indenter approaches and penetrates the specimen surface at a loading rate of 0.7 mN/s in a depth-control mode, followed by a holding segment for 60 s and an unloading segment at a rate of 0.7 mN/s. The thermal drift rate was evaluated by holding the indenter at the 90% unloading for 60 s.

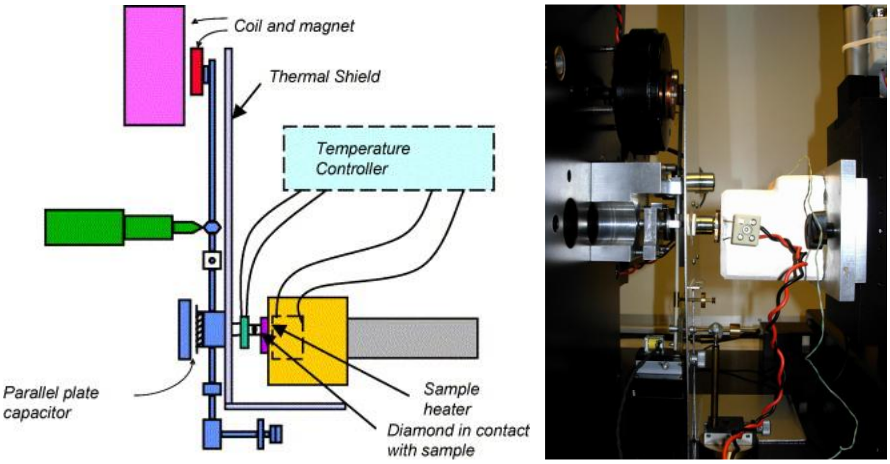

Figure 4.1 Schematic illustration of high-temperature nanoindentaion (on the left) [187] and the experimental set-up (on the right).

4.2.2 Atomic force microscopy

Atomic force microscopy (AFM) is somewhat like a mechanical profilometer in terms of operational manner, i.e., a probe is scanned across the sample surface. In principle, AFM measures the three-dimensional surface topography by detecting the reflection of an oscillating cantilever with a sharp tip on one end.

In this work, a tapping mode AFM (Dimension 3000 SPM, Digital Instruments) was operated in the air. The cantilever keeps oscillating at its resonant frequency and the amplitude remains constant so that the vertical height of the sample surface is revealed. The scan rate is set at 1 Hz.

4.3 Viscoelastic model

4.3.1 Purely elastic contact for Berkovich nanoindentation

The theoretical elastic contact load-displacement (*P*-*h*) curve can be formulated as below:

$$\frac{dP}{dh} = \frac{2}{\sqrt{\pi}} E_r \sqrt{A_p} \tag{4.2}$$

where A_p is the projected contact area. For three-sided Berkovich indenter, A_p is given by [188]:

$$A_p = 3\sqrt{3} h_c^2 \tan^2 65.3 = 24.5 h_c^2 \tag{4.3}$$

where the value of 65.3 indicates the included half-angle of a Berkovich indenter, and h_c is the contact depth. In practice, the indentation or penetration depth is directly measured, which consists of both surface elastic deflection and contact depth. This deflection is expected because the surface area at the contact perimeter can sink in as it feels the downward penetration force. According to the Sneddon's analysis and the work by Oliver and Pharr [186], the elastic deflection can be excluded and thus the contact depth is written as:

$$h_c = h - h_s = h - \varepsilon \frac{P}{S} \tag{4.4}$$

where h is the total measurement depth and h_s is the displacement of surface deflection. P and S are respectively the indentation load and contact stiffness. The dimensionless quantity ε is a geometrical correction constant which, for Berkovich tip, is commonly taken to be 0.75 [186]. P and S are both quantities depending on the indentation depth, and their ratio P/S is commonly proportional to the indentation depth, i.e., $P/S=\gamma h$. Thus, Eq. 4.4 can be rewritten as:

$$h_c = h - \varepsilon\gamma h = h(1 - \varepsilon\gamma) \tag{4.5}$$

By substituting Eqs. 4.3-4.5 into Eq. 4.2, the elastic contact equation is expressed as:

$$\frac{dP}{dh} = 2\sqrt{\frac{24.5}{\pi}}(1-\varepsilon\gamma)E_r h \tag{4.6}$$

$$dP = 2\sqrt{\frac{24.5}{\pi}}(1-\varepsilon\gamma)E_r h \cdot dh \tag{4.7}$$

Because of the boundary condition P=0 at h=0, the following closed-form equation for the P-h relationship using Berkovich indenter is arrived at:

$$P = \sqrt{\frac{24.5}{\pi}}(1-\varepsilon\gamma)E_r h^2 \tag{4.8}$$

from which E_r can be estimated if the elastic P-h curves and the parameter γ are measured.

4.3.2 Viscoelastic effect on elastic curve

MGs exhibit viscoelasticity, which implies that their mechanical properties are time-dependent. The viscoelastic response of MGs starts becoming prominent near glass transition temperature and is usually characterized by dynamic mechanical spectroscopy (DMS), where the Young's modulus can be separated into two components: storage modulus representing the solid-like behavior and loss modulus representing the liquid-like behavior. This separation is considered to be closely associated with the structural characteristics of MGs. As is widely known, MGs are frozen liquids, i.e., their amorphous structure is composed of both solid-like and liquid-like clusters; the former corresponds to the closely packed atomic configurations (e.g., full icosahedra or clusters with fewest disclinations [189]), while the latter corresponds to the loosely packed regions (i.e., distorted atomic configurations with extrinsic disclinations [189]). This nano-scale structural heterogeneity leads to the viscoelastic properties of MGs even at low homologous temperatures (i.e., $T/T_g<0.5$, T for test temperature and T_g for glass transition temperature). For example, Ye *et al* [182] conducted the high-frequency dynamic compression test on a Zr-based MG at room temperature (far below the glass transition temperature of 685 K) and found a mechanical hysteresis loop (anelasticity or viscoelasticity) in the apparent elastic regime as the stress rate increases. The loop has its structural origin, i.e., the liquid-like free volume zones should be confined within elastic atomic clusters.

According to the above discussion, viscoelasticity can be anticipated in amorphous alloys during nanoindentaion. A linear viscoelastic solution has been suggested by Feng and Ngan [190], who employed the correspondence principle in the solution derivation. For fully elastic contact, the relationship between load and the depth of indentation is given by Eq. 4.8. Shifting the parameter E_r to the left, the equation is rewritten as:

$$\frac{1}{E_r}P=\sqrt{\frac{24.5}{\pi}}(1-\varepsilon\gamma)h^2 \tag{4.9}$$

Following Feng and Ngan's work and replacing E_r with its viscoelastic version in Eq. 9 of the Ref. [190],

$$\left[\frac{1}{E_r}+\frac{3\dot{\varepsilon}_0}{4\sigma_0}\frac{1}{s}+\frac{E^2\dot{\varepsilon}_0}{36B^2(\sigma_0 s+E\dot{\varepsilon}_0)}\right]P^*=\sqrt{\frac{24.5}{\pi}}(1-\varepsilon\gamma)(h^2)^* \tag{4.10}$$

where s is a complex variable, $\dot{\varepsilon}_0$ and σ_0 are normalizing materials constants, E and B are the Young's and bulk moduli respectively, and * refers to the quantity in the Laplace transform. Inverse transform of Eq. 4.10 gives the following expression:

$$\frac{P(t)}{E_r}+\frac{3\dot{\varepsilon}_0}{4\sigma_0}\int_0^t P(t')dt'+\frac{E^2\dot{\varepsilon}_0}{36B^2\sigma_0}\int_0^t \exp\left[-\frac{E\dot{\varepsilon}_0}{\sigma_0}(t-t')\right]P(t')dt'=\sqrt{\frac{24.5}{\pi}}(1-\varepsilon\gamma)h^2 \quad (4.11)$$

Assuming $u=-E\dot{\varepsilon}_0/\sigma_0(t-t')$, the above equation is simplified:

$$\frac{P(t)}{E_r}+\frac{3\dot{\varepsilon}_0}{4\sigma_0}\int_0^t P(t')dt'+\frac{E^2\dot{\varepsilon}_0}{36B^2\sigma_0}\int_0^t \exp(u)P(t')dt'=\sqrt{\frac{24.5}{\pi}}(1-\varepsilon\gamma)h^2 \quad (4.12)$$

$$\frac{P(t)}{E_r}+\frac{3\dot{\varepsilon}_0}{4\sigma_0}\int_0^t P(t')dt'+\frac{E^2\dot{\varepsilon}_0}{36B^2\sigma_0}\int_0^t \dot{P}\frac{t'}{du/dt'}d\exp(u)=\sqrt{\frac{24.5}{\pi}}(1-\varepsilon\gamma)h^2 \quad (4.13)$$

$$\frac{P(t)}{E_r}+\frac{3\dot{\varepsilon}_0}{4\sigma_0}\int_0^t P(t')dt'+\frac{E^2\dot{\varepsilon}_0}{36B^2\sigma_0}\frac{\dot{P}}{du/dt'}\left[\left(t'\exp(u)\right)\Big|_0^t-\int_0^t \exp(u)dt'\right]=\sqrt{\frac{24.5}{\pi}}(1-\varepsilon\gamma)h^2$$

(4.14)

$$\frac{P}{E_r}+\frac{3\dot{\varepsilon}_0}{8\sigma_0\dot{P}}P^2+\frac{E}{36B^2}\left\{P-\frac{\dot{P}\sigma_0}{E\dot{\varepsilon}_0}\left[1-\exp\left(-\frac{E\dot{\varepsilon}_0}{\sigma_0}\right)\right]\right\}=\sqrt{\frac{24.5}{\pi}}(1-\varepsilon\gamma)h^2 \quad (4.15)$$

Usually the third term in the left-hand side is negligible because E/B^2 is too small. Thus, the reduced form of Eq. 4.15 is given as:

$$\frac{P}{E_r}+\frac{3\dot{\varepsilon}_0}{8\sigma_0\dot{P}}P^2=\sqrt{\frac{24.5}{\pi}}(1-\varepsilon\gamma)h^2 \quad (4.16)$$

Although this simple model disregards the structural origin, it has some implications:

1. The elastic portion of the load-displacement relationship is dependent on loading rates, which is more significant at lower loading rates.
2. The mechanical properties can be affected by loading rates due to the viscoelasticity. For example, when an equal indentation force is applied, the materials at lower loading rates should have a larger contact depth and thus a lower hardness.

The above analysis indicates that loading conditions are important for nanoindentation measurement especially on MGs. In the following sections, the major effects such as loading rate, indentation size and temperature will be systematically investigated.

4.4 Effects on load-displacement behaviors

4.4.1 Loading rate dependence

Load-displacement (*P*-*h*) curves for three MGs are respectively given in Fig. 4.2, which have been separated from each other for easy viewing. The loading-rate range for each MG is presented on the top of each figure and for consistency is specified here: 1 up to 50 mN/s for La-based, 0.05 up to 50 mN/s for Zr-based, and 0.01 up to 1 mN/s for $Cu_{49.3}Zr_{50.7}$. It can be observed that, for each alloy, the curves become increasingly serrated as the loading rate decreases. The similar behavior has been found in compression tests of MGs [191], where each load serration is thought to arise from the movement of an individual SB. By analogy, each serration during nanoindentaion on MGs is initiated by the operation of a single SB [52, 192]. This rate dependence of serrated flow can also be manifested by the indentation strain rate which is expressed as:

$$\dot{\varepsilon} = \frac{1}{h} \cdot \frac{dh}{dt} \tag{4.17}$$

where t denotes time. Presented in Fig. 4.3 is the equivalent strain rate versus indentation depth. The strain rate decreases as the depth increases and becomes almost constant at deep indents. The strain rate peaks definitely correspond to the load serrations and become less prominent as loading rate increases. The physical origin for the rate-dependent serrated flow still remains under discussion and so far two viewpoints have been proposed. Schuh *et al* [192] believed that this behavior is linked to the change of the deformation mechanisms, i.e., plasticity at low rates can be accommodated by single SBs, while at higher rates by multiple SBs. However, other researchers attributed the apparent inhomogeneous-to-homogeneous transition to the limited instrumental resolution. For example, Jang *et al* [193] found that the serrated flow strongly depends on the tip geometry during nanoindentation, i.e., the serration disappears at high rates for Berkovich indenter while still exists at the same high rates for cube-corner indenter, and thus concluded that the instrumental blurring largely contributes to the absence of serrated flow at high rates.

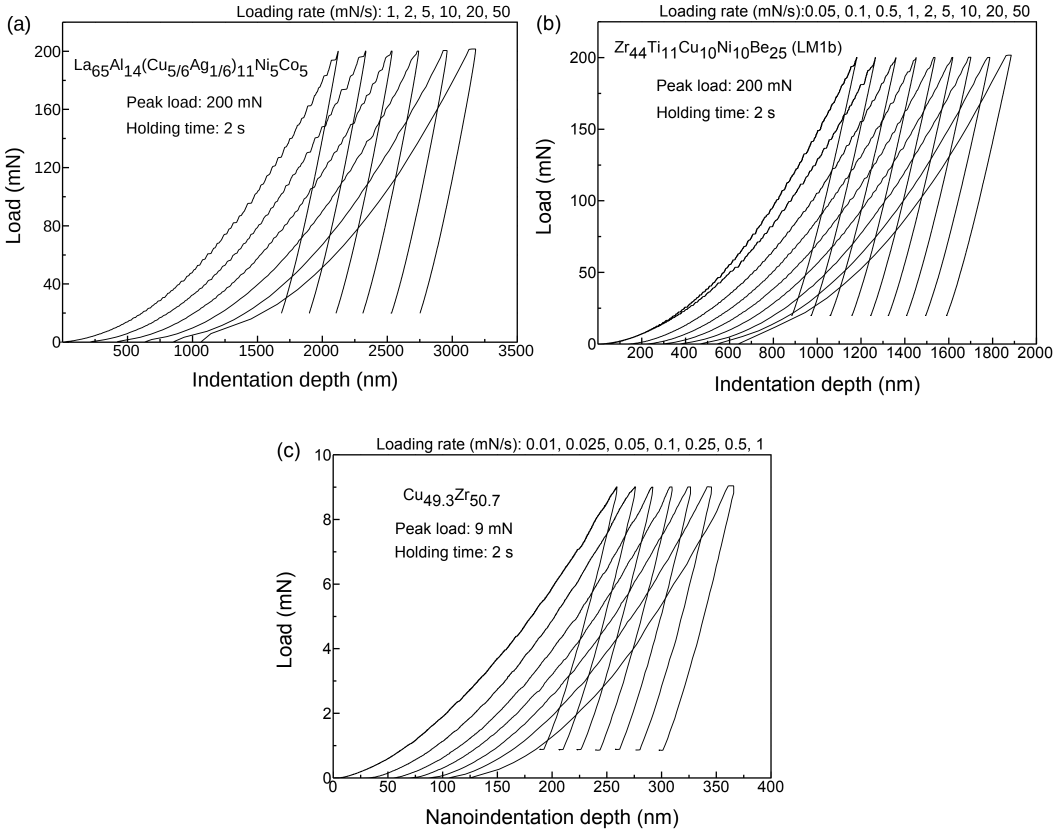

Figure 4.2 Load-displacement curves for three MGs of this study. The composition and loading rate are described in each figure. Curves are separated for clarity.

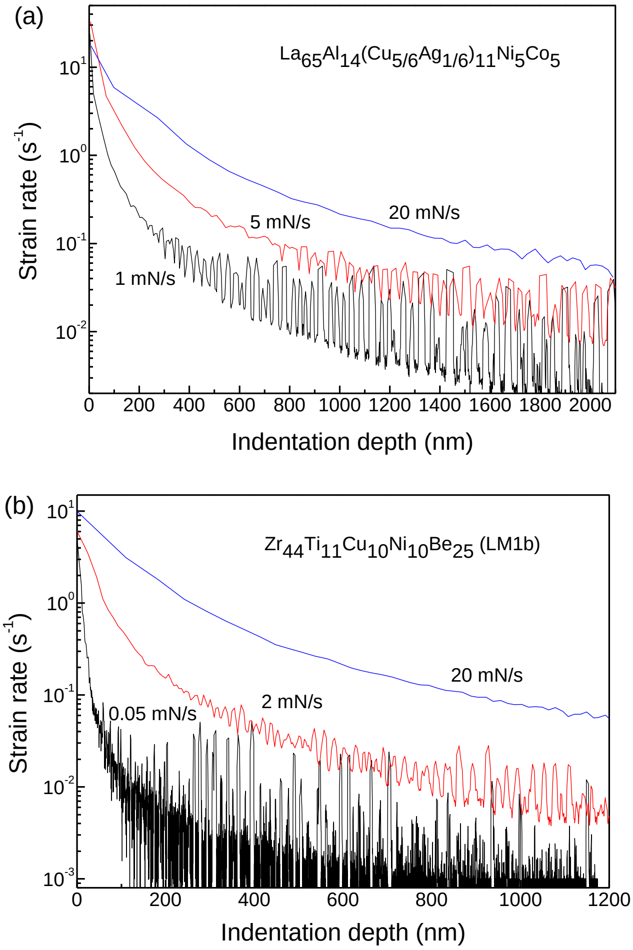

Figure 4.3 The dependence of strain rate on the indentation depth for (a) La- and (b) Zr-based MGs. The curves become increasingly serrated as the loading rate decreases.

Shown in Fig. 4.4 are the so-called consolidated elastic curves for both La- and Zr-based alloys, where the unloading elastic curve for La-based is given for comparison. The consolidated elastic curves are constructed by using the method of Gouldstone *et al* [194]. For La-based, the consolidated curve resembles the unloading curve, which suggests that the discrete displacement bursts mainly account for the plastic deformation. Since the serrated flow corresponds to the SB activity, AFM experiments were performed to scan the residual indents made at various loading rates. In Fig. 4.5, it can be seen that there exist a number of SBs around the indents even at high rates although no serration appears on the corresponding *P-h* curves. The intensity of SBs does not exhibit clear dependence on the loading rates. The indentation profiles at maximum loads for both La- and Zr-based alloys are presented in Figs. 4.6a and b, where the insets show the scanning direction. The black arrows in Figs. 4.6a and b point the slight increase in indentation depth which is due to the slight increase of maximum indentation load with increasing loading rate (about 1 mN difference between the slowest and fastest rates for both La- and Zr-based alloys). Pile-ups do occur during nanoindentation and affect the correct measurement of hardness and modulus. Demonstrated in Figs. 4.6c and d are the pile-up heights and height ratios (defined as the ratio of pile-up height to indentation depth) as a function of loading rate. They are both independent of loading rate. Therefore, pile-ups at various loading rates should contribute equally to hardness and modulus. Following the way of Ramamurty *et al* [195], the shear band zone size δ is measured (here defined as the radius from the center of the indentation to the edge of the visible outmost SB) and plotted as a function of loading rate in Fig. 4.6e. Clearly, when the peak load is fixed, δ holds approximately invariable within the range of loading rate. The physical implication of this length scale will be discussed in Section 4.5.1.

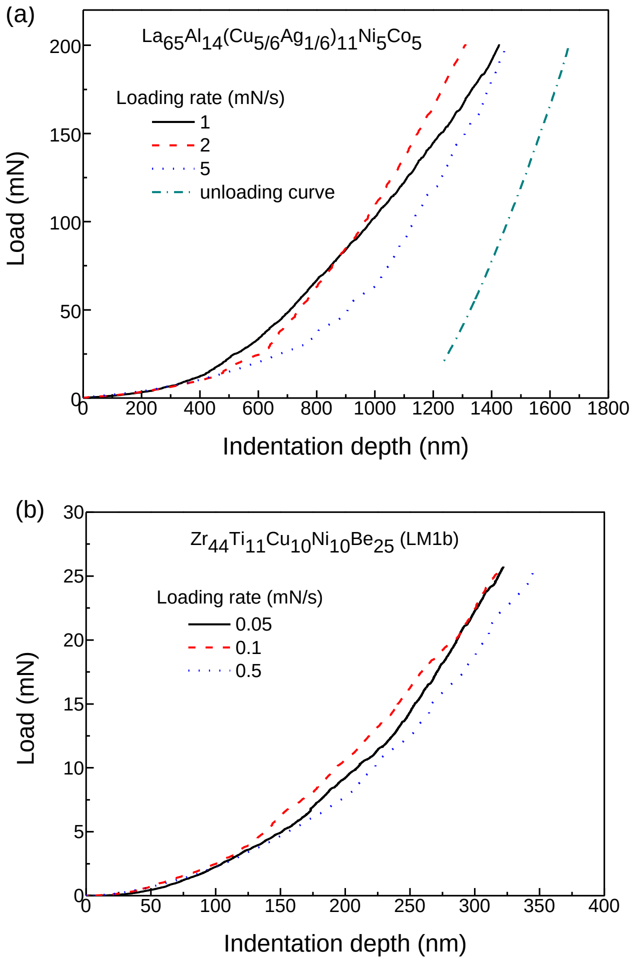

Figure 4.4 Consolidated elastic curves for (a) $La_{65}Al_{14}(Cu_{5/6}Ag_{1/6})_{11}Ni_5Co_5$ and (b) $Zr_{44}Ti_{11}Cu_{10}Ni_{10}Be_{25}$ (LM1b) alloys, which are constructed by substracting the displacement bursts from the *P*-*h* curves. The unloading elastic curve only for La-based alloy is presented in Fig. 4.4a for comparison because for Zr-based alloy, at small indentation load (i.e., below the unload limit which is 10% of the maximum load), the unloading curve is not given by the test instrument. Nevertheless, the consolidated curves for La-based alloy resemble the unloading curve, indicating that the displacement bursts mostly contribute to the plastic deformation.

(a) $La_{65}Al_{14}(Cu_{5/6}Ag_{1/6})_{11}Ni_5Co_5$

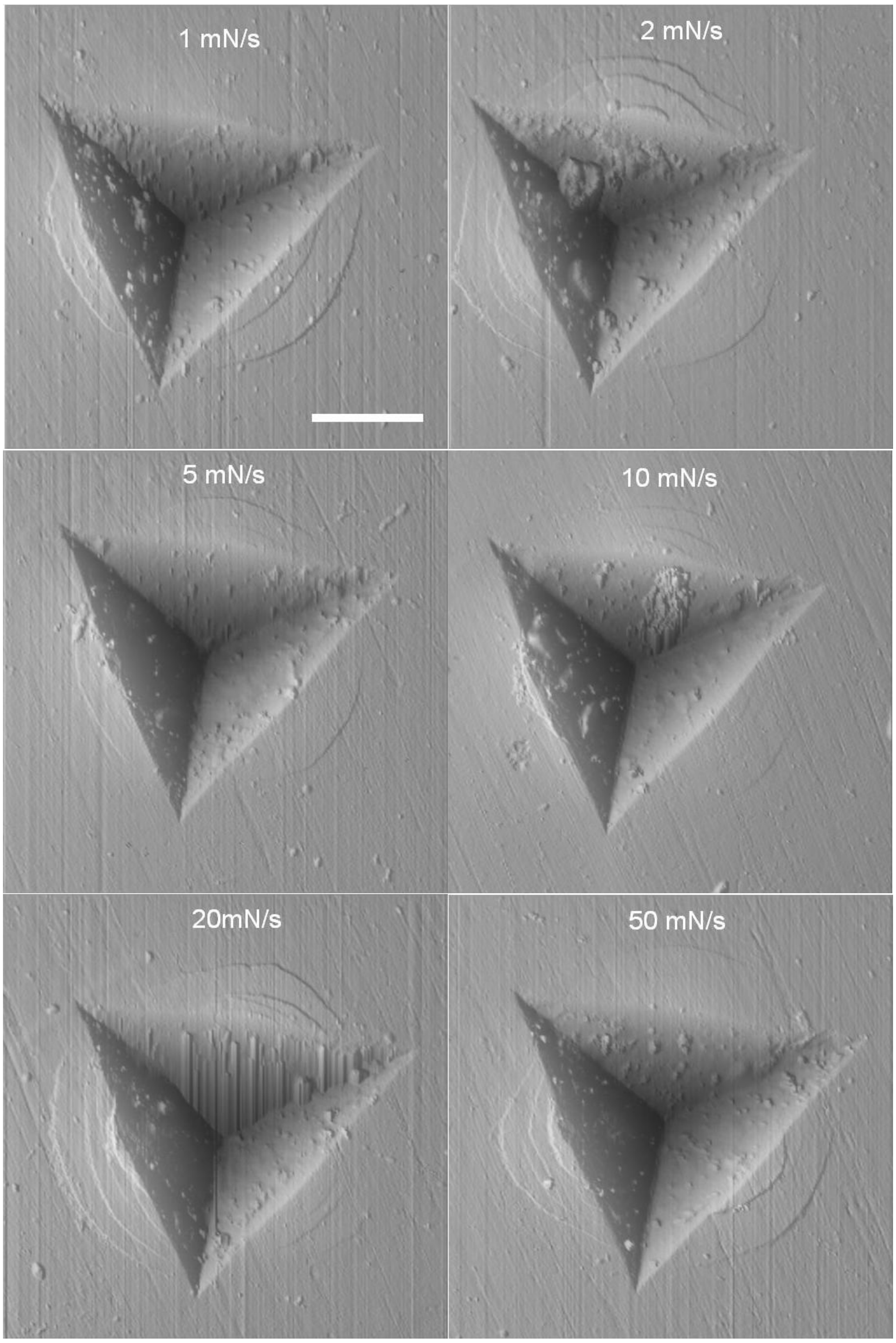

(b) $Zr_{44}Ti_{11}Cu_{10}Ni_{10}Be_{25}$ (LM1b)

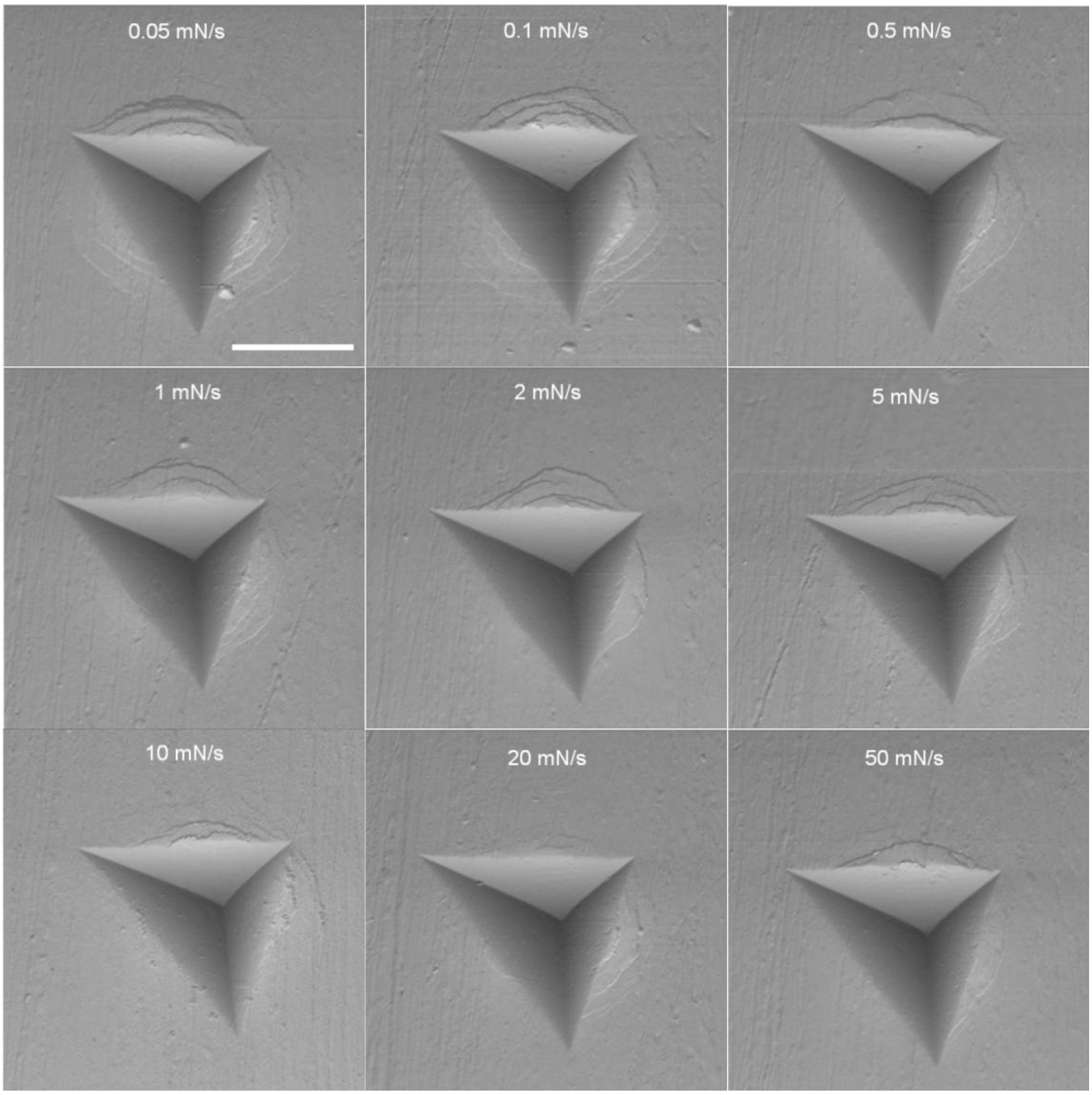

Figure 4.5 AFM images of residual indents made at various loading rates for both (a) La- and (b) Zr-based MGs. The white scale bars in the insets of the figures indicate 5 µm. Unlike the *P-h* curves where serrations disappear at high rates, SBs do occur around the edges of the indents even at the largest rates. There is not a clear relationship between SB density and loading rate.

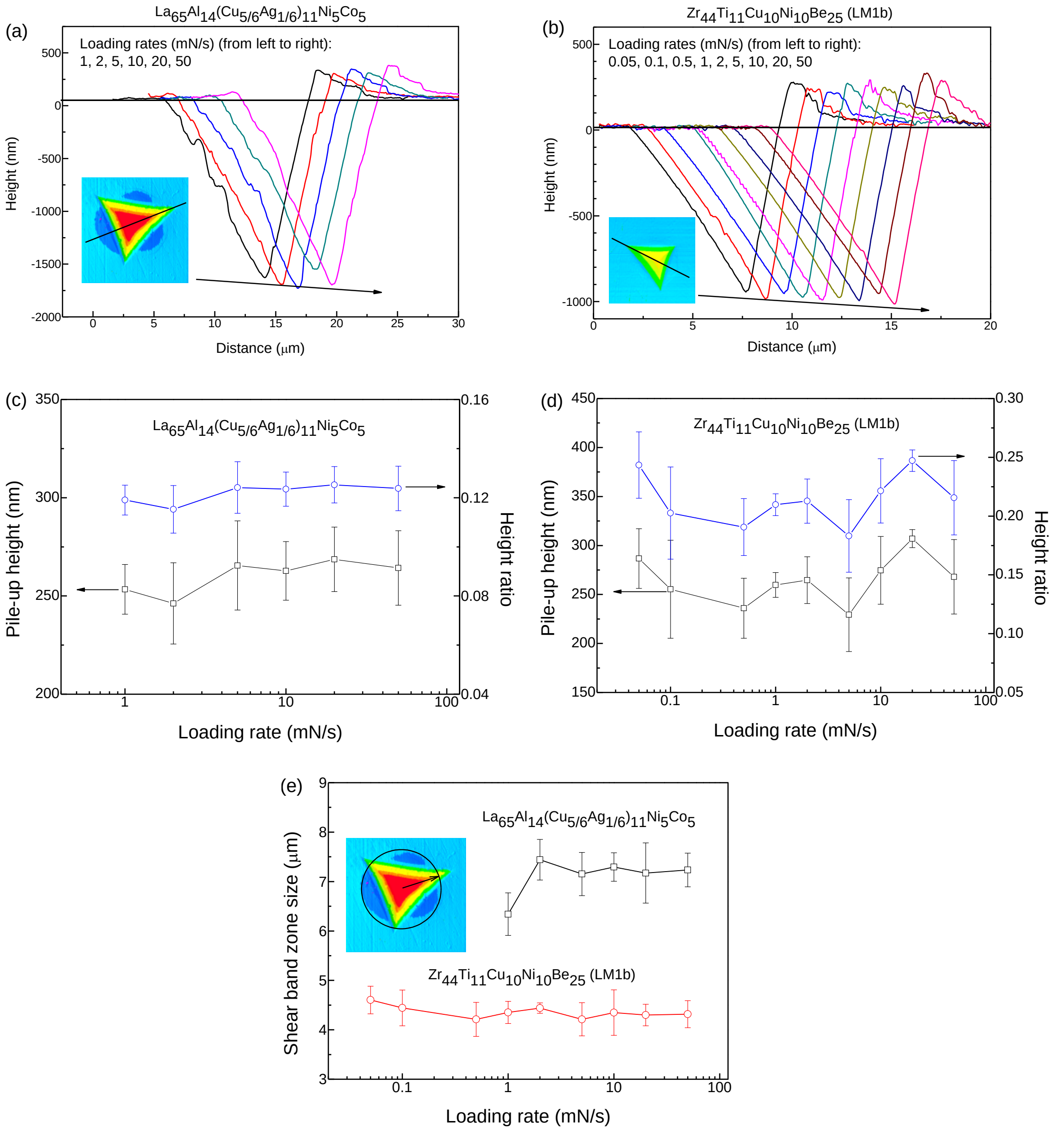

Figure 4.6 Indentation profiles for (a) $La_{65}Al_{14}(Cu_{5/6}Ag_{1/6})_{11}Ni_5Co_5$ and (b) $Zr_{44}Ti_{11}Cu_{10}Ni_{10}Be_{25}$ (LM1b) alloys with scanning direction indicated in the insets. The loading rate dependence of (c)-(d) pile-up height, height ratio and (e) shear band zone size are plotted. The black arrow in the inset of Fig. 4.6e shows the definition of shear band zone size.

From the *P-h* curves in Fig. 4.2, it can also be seen that the displacement burst length is dependent on the indentation depth, i.e., larger indentation depths make larger burst events, which is described for both La- and Zr-based MGs in Figs. 4.7a and b. This phenomenon is interpreted by Schuh *et al* [192] as a natural result of the growing length scale of the indentation geometry. Structurally, it could be related to the STZs. It is commonly known that SBs are produced by collection of these plastic deformation units. As the indentation depth increases, the plastic deformation zone beneath the tip expands and thus more STZs are involved, which promotes larger shear displacement of SBs [81]. It should be noted that, even at large indentation depth, there still exist small displacement bursts, which has been observed as well in other MGs [196]. Interestingly, the total displacement burst length (h_{bt}) is proportional to the corresponding indentation depth (see Figs. 4.7c and d), no matter what the loading rate is. In the insets of Figs. 4.7c and d, the ratio h_{bt}/h_p increases initially and holds constant finally, which might indicate that the plastic length is independent of loading rate because the total indentation depth does not change across the whole range of loading rates.

4.4.2 Elevated temperature

The representative P-h curves at elevated temperatures for $Cu_{50}Zr_{50}$ are presented in Fig. 4.8a, where the unloading curves are hidden for clarity. The DBs can be observed at each of the test temperatures, which is the result of shear banding movement. The shearing displacement becomes larger as the indentation depth increases, which is attributed to the increasing free volume concentration. Explicitly, the deformation behavior is certainly dependent on the temperatures. On the one hand, the occurring frequency of the DBs increases as the temperature rises, i.e., the higher the temperature, the larger number of SBs will be generated. On the other hand, the DBs appear to get slightly wider at higher temperatures. Shown in Figs. 4.8b and c are the P-h curves respectively at 298 and 393 K, each measured 5 times to confirm the repeatability of the serrated flow behavior.

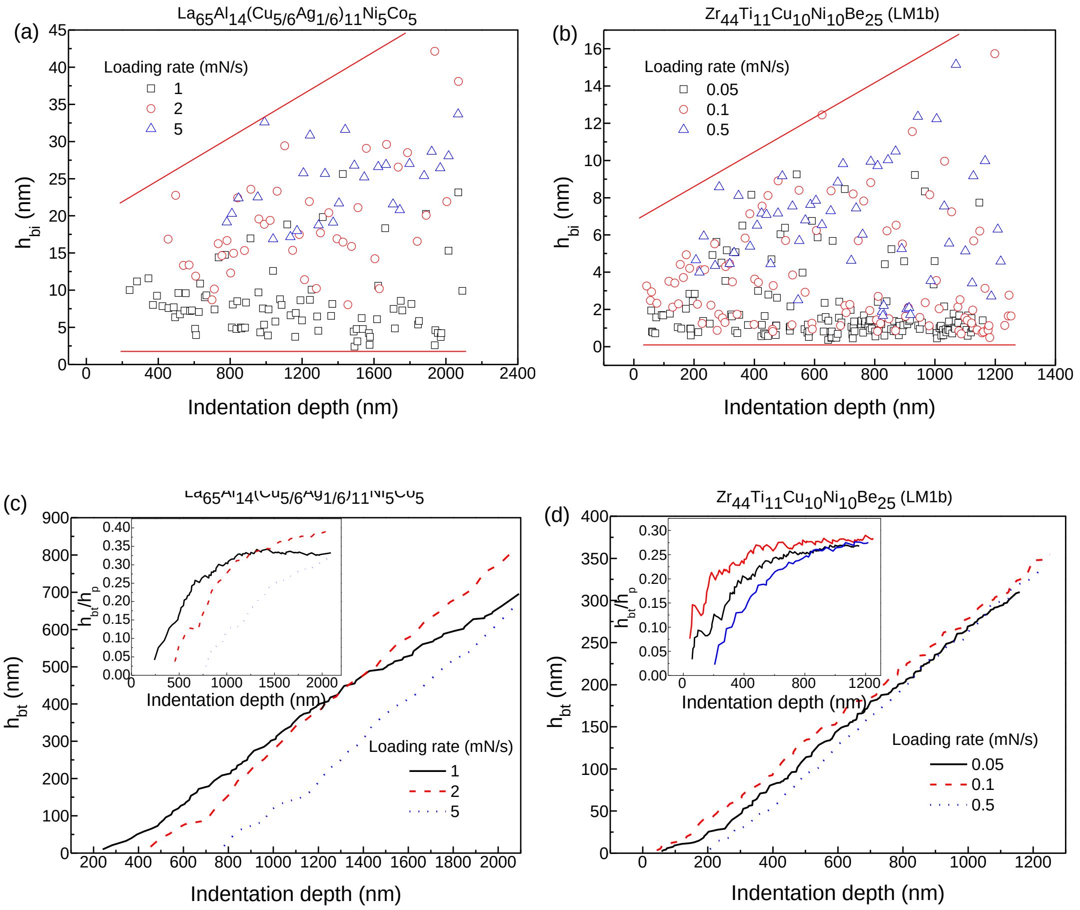

Figure 4.7 (a)-(b) An individual displacement burst length (h_{bi}) and (c)-(d) total displacement burst length (h_{bt}) plotted as a function of indentation depth. The insets in Figs. 4.6c and d show the relationship between the ratio h_{bt}/h_p and indentation depth.

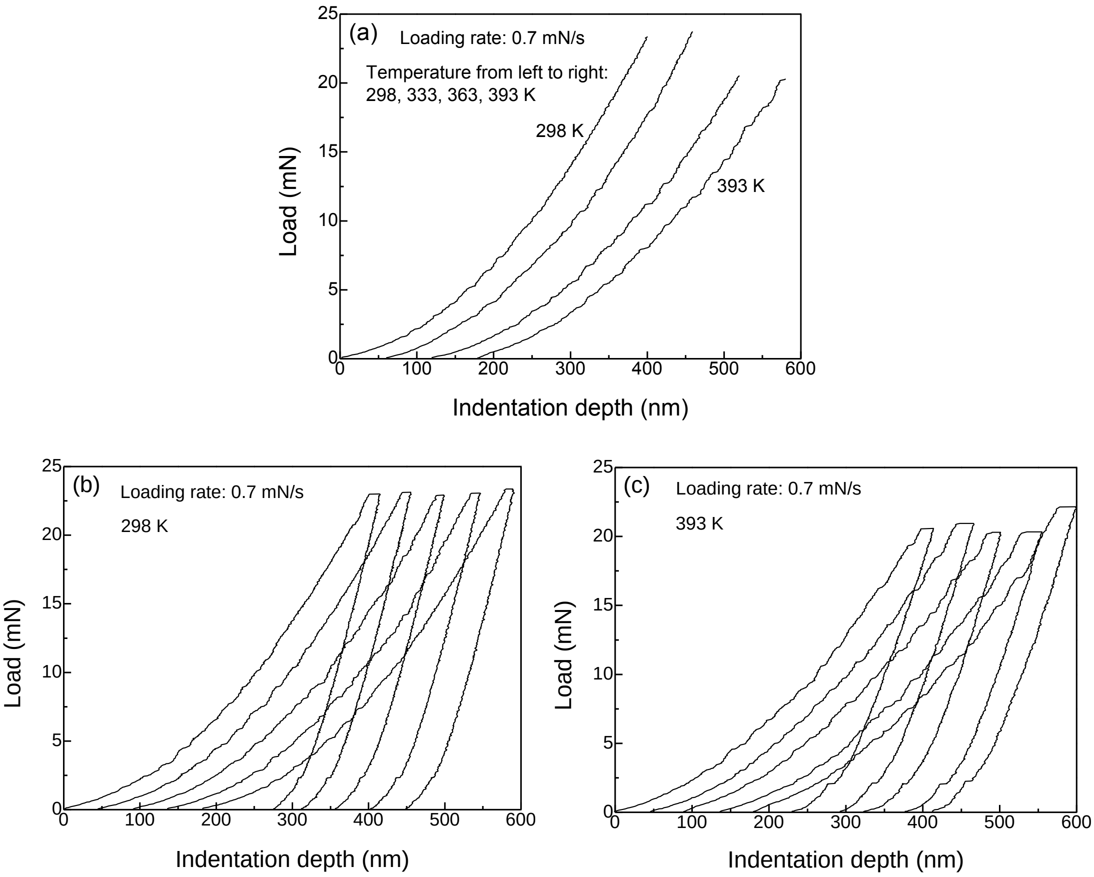

Figure 4.8 (a) Typical load-displacement curves at elevated temperatures for $Cu_{50}Zr_{50}$. Loading/unloading behaviors at (b) 298 K and (c) 393 K are shown to examine the reproducibility of the discrete flows.

4.5 Effects on mechanical properties

4.5.1 Loading rate dependence

The loading rate effects on mechanical properties such as hardness and modulus are illustrated in Fig. 4.9 for $La_{65}Al_{14}(Cu_{5/6}Ag_{1/6})_{11}Ni_5Co_5$, $Zr_{44}Ti_{11}Cu_{10}Ni_{10}Be_{25}$ (LM1b) and $Cu_{49.3}Zr_{50.7}$ MGs. In comparison with the nanoindentation experiment, hardness is also calculated directly upon measurement of the area of the residual indents by AFM imaging (see Fig. 4.5). Before discussing this effect, it is helpful to introduce an equation as given in [197]:

$$\frac{P}{S^2} = \frac{1}{\beta^2}\frac{\pi}{4}\frac{H}{E_r^2} \tag{4.18}$$

where β is a parameter depending on the geometry of the indentation tip. For elastically homogeneous materials, P/S^2 or H/E_r^2 reflects the true change in hardness because it does not contain the projected area. For La-based alloy, hardness remains almost constant while modulus has a small but visible increase with an increase in loading rate. Thus, H/E^2 in Fig. 4.9c appears to decrease. The reason for increasing modulus lies in the slight increase in the contact stiffness as shown in Fig. 4.9b. For Zr-based alloy, hardness and modulus at the lowest rate are comparatively large and approach constant values at higher rates. AFM measurements definitely indicate that hardness is not dependent on loading rate. Moreover, H/E^2 stays almost invariable across the loading rate range, agreeing well with the AFM results.

It is worth mentioning that, for both La- and Zr-based alloys, hardness by AFM is usually smaller than that by nanoindentation, which is attributed to the pile-up effects. The pile-up volume expands as the indentation depth is increased, which produces a pile-up height and sustains an extra indentation load. However, the indentation depth used in the Oliver-Pharr method does not take this height into consideration, in other words, the contact area is underestimated. By AFM imaging, the pile-up area is included in the total area measurement and thus the hardness can be expected to come down.

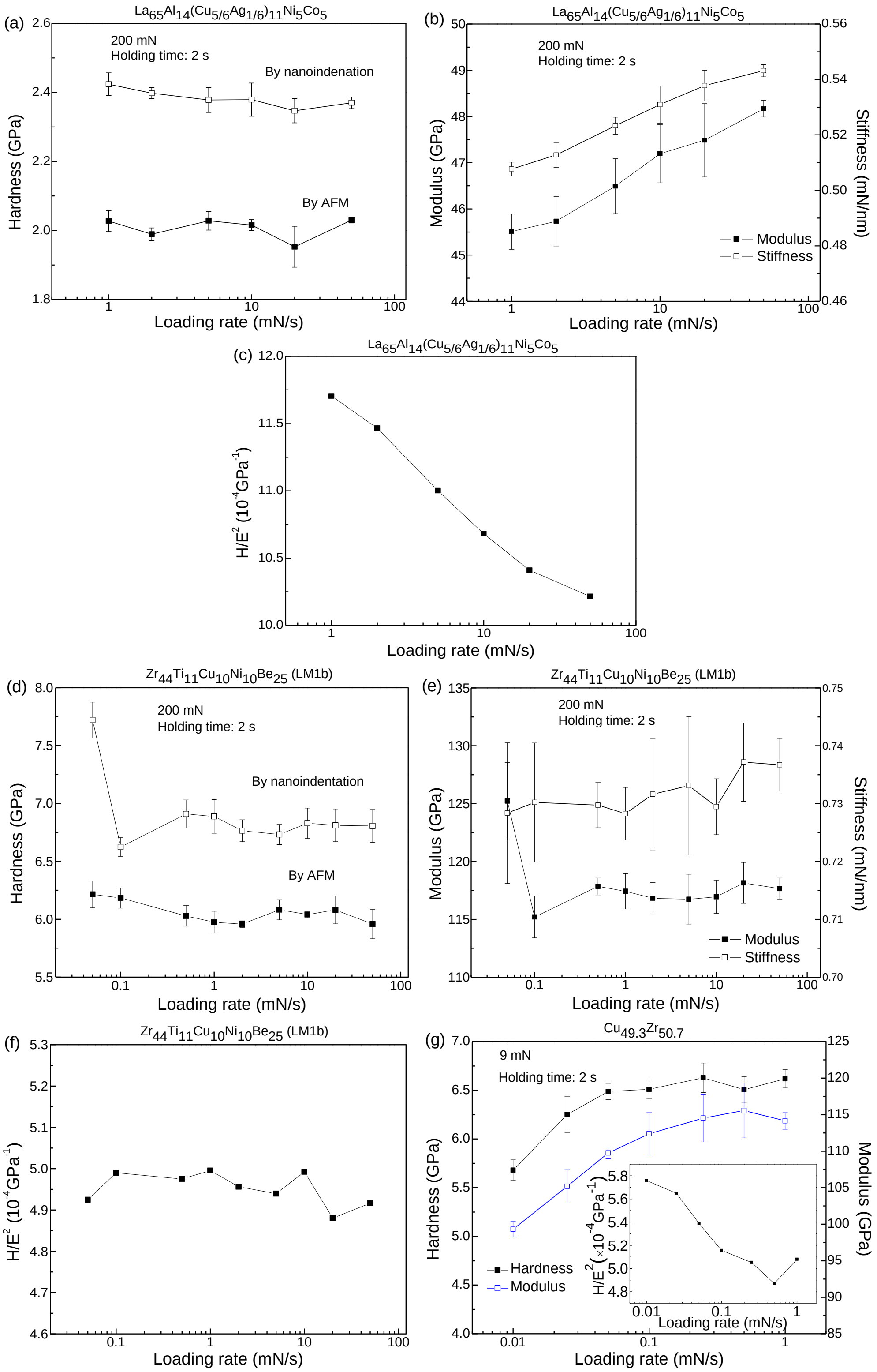

Figure 4.9 Loading rate dependence of mechanical properties for three MGs: (a)-(c) $La_{65}Al_{14}(Cu_{5/6}Ag_{1/6})_{11}Ni_5Co_5$, (d)-(f) $Zr_{44}Ti_{11}Cu_{10}Ni_{10}Be_{25}$ and (g) $Cu_{49.3}Zr_{50.7}$. AFM hardness is measured for comparison with the nanoindentaion results. The composition, holding time and peak load are indicated on each figure.

Fig. 4.9g displays the loading rate effects on the mechanical properties of the amorphous thin films $Cu_{49.3}Zr_{50.7}$ under the peak load of 9 mN with a holding time of 2 s. Both the hardness and modulus increase as the loading rate increases up to 0.1 mN/s, and as the loading rate continues increasing, they keep relatively stable during the tests. The free volume model or STZ model is usually introduced to understand the dependence relation. In fact, they are interrelated especially at equilibrium, described by the equation $C_\xi=\exp(-1/\xi)$, where C_ξ and ξ are respectively the concentration for STZs and free volume [52, 65]. Free volume is the preferential site to initiate the STZs, while STZ operations assist the generation of free volume by the shear-induced dilation. As Sort *et al* [106] discussed, the production rate of defect concentration is related to the loading rates. In the tests at the loading rate smaller than 0.1 mN/s, as the loading rate increases, the free volume cannot be created fast enough to facilitate the plastic deformation and thus the mechanical properties are enhanced. In the tests with a loading rate above 0.1 mN/s, however, this interpretation seems not viable for understanding the constant hardness. Another interpretation for the loading rate dependence of hardness takes into consideration the anelastic/viscoplastic properties of MGs [198]. These properties are time-dependent and would become more significant at lower loading rates. Therefore, plastic deformation can be fully developed at the lowest loading rate and hardness increases with increasing loading rates. At relatively large loading rates (0.1 mN/s in this study), these properties would become negligible and thus hardness remains constant. The variation in modulus can also be understood in terms of these time-dependent characteristics. It is known that the Oliver-Pharr method is only applicable to purely elastic materials. When materials exhibit viscoelasticity, correction to this method has to be made to recognize the viscoelastic effect on contact stiffness [199]. For this reason, the elastic modulus is found to be dependent on the loading rate. It is interesting to see the viscoelastic effect on the ratio of H/E^2. The inset in Figs. 4.9g is the plot of H/E^2 versus loading rate. It can be observed that, contrary to the trend of hardness and modulus, the ratio decreases as the loading rate increases. Therefore, in case of viscoelastic materials, H/E^2 should be carefully used when representing the hardness variation.

As viscoelasticity may exist in MGs, additional tests with a holding time of 100 s were performed for $Zr_{44}Ti_{11}Cu_{10}Ni_{10}Be_{25}$ (LM1b) and $Cu_{49.3}Zr_{50.7}$ alloys to eliminate the creep effect during the loading segment. The loading rate dependence of hardness and modulus is presented in Fig. 4.10. For Zr-based alloy, hardness and modulus both exhibit no dependence on loading rate, which is also verified by the approximately constant H/E^2 in the inset of Fig. 4.10a. Due to the lacking of viscoelastic effect, the extended holding time does not affect the values of hardness and modulus. For $Cu_{49.3}Zr_{50.7}$ alloy, the variation of hardness, modulus and H/E^2 resembles that shown in Fig. 4.9g, but the differences between the lowest and highest indentation rates (0.74 GPa in hardness and 8.97 GPa in modulus) become smaller than those with a holding time of 2 s (0.94 GPa in hardness and 14.83 GPa in modulus). In addition, as the result of viscoelasticity, the longer holding time reduces the hardness and modulus.

It can be concluded that, according to the above data, the mechanical properties of MGs investigated do not have loading rate dependence above a critical loading rate. Looking back at Section 4.4.1, the shear band zone size δ gives another evidence for this conclusion. Following the Johnson’s spherical cavity model [200], this size δ is related to the yield strength σ_y of materials [195]:

$$\delta = \left(\frac{3P}{2\pi\sigma_y} \right)^{0.5} \tag{4.19}$$

As described in Section 4.4.1, δ and P are both constants and thus the yield strength should be a constant, too. Since hardness has a linear relationship with yield strength [201], it does not change with loading rate.

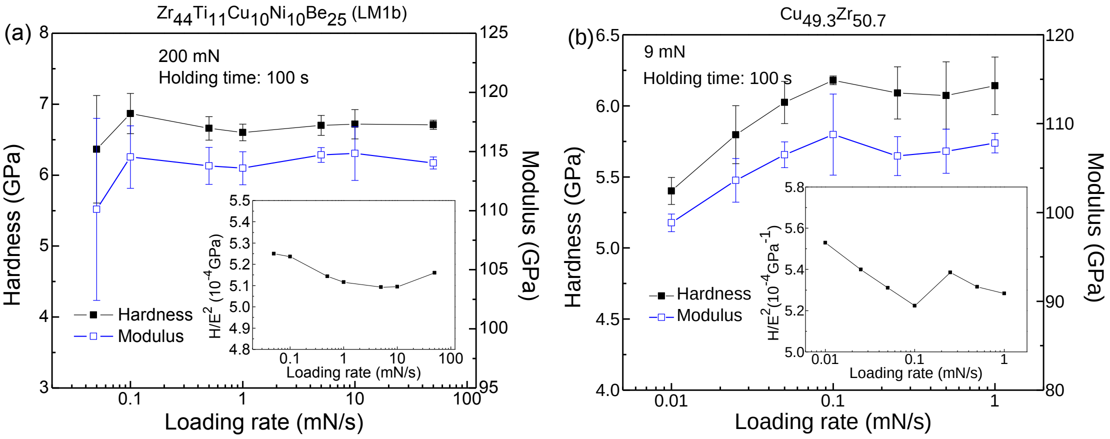

Figure 4.10 Loading rate dependence of mechanical properties for (a) $Zr_{44}Ti_{11}Cu_{10}Ni_{10}Be_{25}$ (LM1b) and (b) $Cu_{49.3}Zr_{50.7}$ characterized by a nanoindentation testing with a holding time of 100 s.

4.5.2 Indentation size effect

The indentation size effect (ISE) is a size-dependent behavior of materials subjected to the indentation load. For geometrically self-similar indenters such as Berkovich and Vickers, the indentation size indicates the indentation depth, and the ISE is known as the enhanced hardness at shallow depths. This effect has been widely observed in crystalline/amorphous alloys, which is interpreted by either the strain gradient plasticity (SGP) model [80, 105] or the proportional specimen resistance (PSR) model [81, 202, 203]. The SGP was firstly introduced to understand the ISE in crystalline materials [204]. During indentation, the so-called geometrically necessary dislocations are created by a strain gradient to accommodate the surface deformation. This structural picture leads to the most respected equation, the Nix-Gao relation [204]:

$$\frac{H}{H_0}=\sqrt{1+\frac{h^*}{h}} \tag{4.20}$$

where H_0 is the hardness in the absence of strain gradients, h is the indentation depth, and h^* is a characteristic material length scale. Similarly, in MGs, free volume exists instead of dislocations. The strain gradient should increase the free volume concentration with further deformation by inducing geometrically necessary excessive free volume and thus should reduce the hardness of materials. Accordingly, Yang *et al* [80] proposed an equation analogous to the Nix-Gao relation with a different mathematical form for H_0. One of problems with free volume theory is that it fails to describe the plastic deformation. Furthermore, computational and experimental work has suggested that plastic deformation of MGs is associated with the cooperative motion of STZs. From this cluster viewpoint, Lam and Chong [205] reformulated the relationship:

$$\frac{H}{H_0}=1+\frac{h^*}{\sqrt{h}} \tag{4.21}$$

where H_0 is the strain-gradient-free hardness, and h^* is the characteristic length scale depending on material properties and indenter shape.

The nanoindentation testing has been carried out on four MGs with two methods, named as normal method (NM) and continuous stiffness measurement (CSM) method, respectively. The NM has been described in the section of experimental methods (Section 4.2.1.1). The CSM is able to characterize the stiffness and thus both contact hardness and modulus at each of the penetration depths by applying a small sinusoidal vibration (2 nm in amplitude and 45 Hz in frequency) to the indenter column. The depth dependence of mechanical properties is presented in Fig. 4.11. For all of the four alloys, the Young's modulus remains constant above 100 nm, which is indicative of the reliable measurements because it is an intrinsic property of materials and should not change in most cases. By means of NM and CSM, the hardness for both La- and Zr-based alloys is found to be depth-dependent; the former shows a significant ISE while the latter has a slight ISE.

The testing on $Mg_{67}Zn_{28}Ca_5$ was performed to see if the tip radius of the indenter could contribute to the ISE (Fig. 4.11c). The tip is commonly supposed to have a perfect shape and its effect on indentation depth is ignored in the area function. This assumption is acceptable when the depth is large enough. However, when the depth is comparable to the tip radius, this assumption definitely fails. It can be envisioned that at small indents, as the depth declines, the tip rounding effect becomes progressively significant and the indentation depth is seriously underestimated. Thus, an artificial ISE may occur. In Fig. 4.11c, throughout the depth range above 100 nm, Mg-based alloy shows no variation in hardness and modulus, suggesting that the tip radius effect is trivial in the current study.

For La-based alloy, the remnant impressions made under different loads are visualized by AFM and displayed in Fig. 4.12, where the SBs are evident for each load. The AFM hardness given in Fig. 4.11a again confirms the existence of the ISE but has a lower value. In Fig. 4.13, the pile-up height and shear band zone size are both observed to have a positive size effect. Interestingly, the height ratio is independent of the indentation depth, and the experimental data for δ deviate slightly from the curve fitting with Eq. 4.19, which is thought to result from the ISE. Eqs. 4.20 and 4.21 are both applied to fit the ISE and the fitting parameters for CSM are tabulated in Table 4.1. Although these two equations have a good fit to the experimental results, Eq. 4.21 based on the cluster model appears more reliable because the strain-gradient-absent hardness H_0 approaches the measured value. For this reason, only the fitting parameters of Eq. 4.21 for NM and AFM are produced in Figs. 4.11a and b.

Table 4.1 Fitting parameters for the indentation size effects by CSM

Composition	$La_{65}Al_{14}(Cu_{5/6}Ag_{1/6})_{11}Ni_5Co_5$		$Zr_{44}Ti_{11}Cu_{10}Ni_{10}Be_{25}$ (LM1b)	
	Eq. 4.20	Eq. 4.21	Eq. 4.20	Eq. 4.21
H_0 (GPa)	4.74	2.37	15.09	7.55
h^* (nm)	24.04	48.07	14.15	28.30

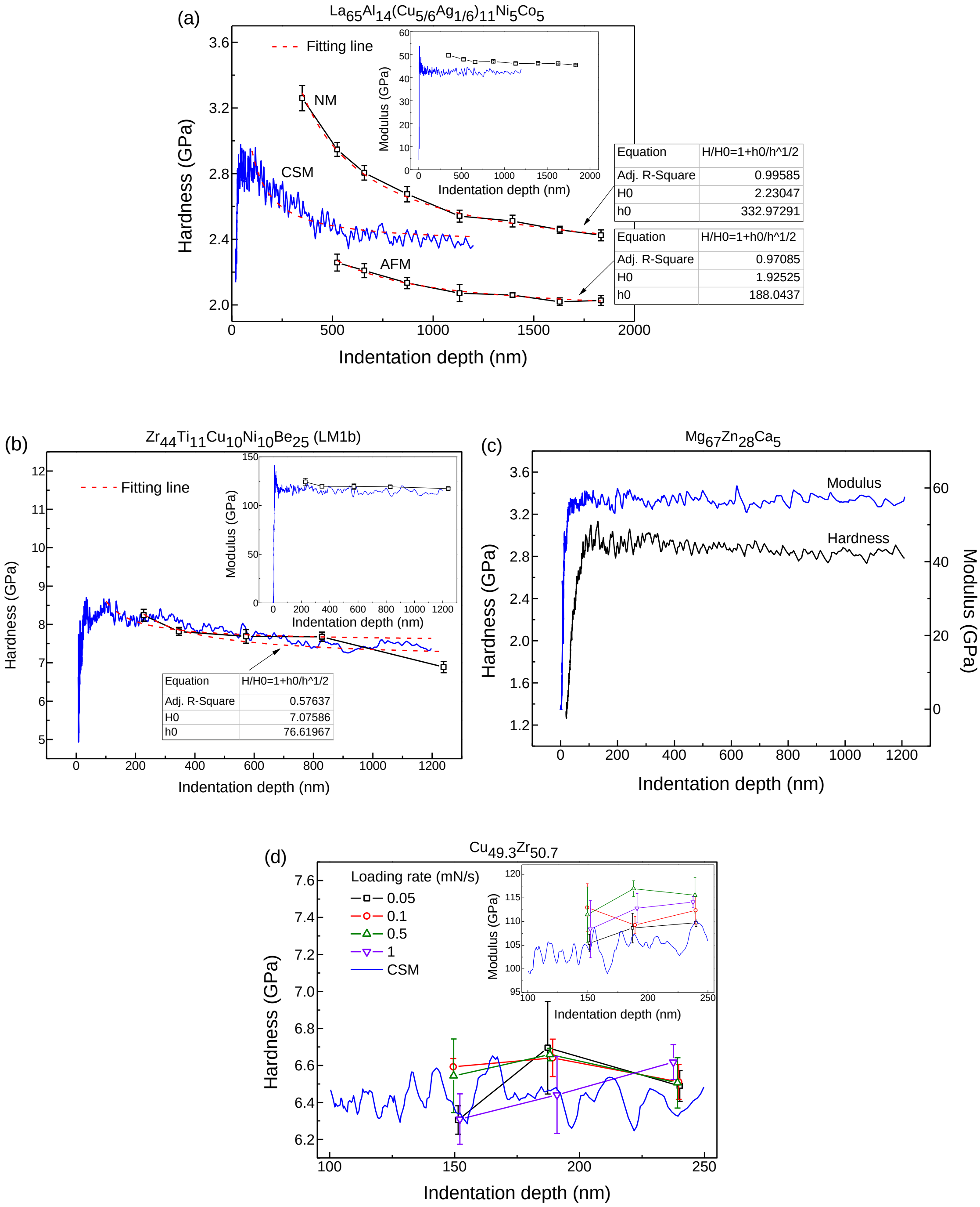

Figure 4.11 Mechanical properties as a function of indentation depth for four MGs. In the insets, the constant modulus indicates the reliable testing. La- and Zr-based alloys exhibit an ISE while $Cu_{49.3}Zr_{50.7}$ does not. The testing on $Mg_{67}Zn_{28}Ca_5$ is used to examine the tip radius effect on the ISE. The fitting parameters for NM and AFM are given in the figures and those for CSM are listed in Table 4.1.

The indentation depth dependence of hardness and modulus of the thin films $Cu_{49.3}Zr_{50.7}$ is given in Fig. 4.11d. It is obvious, at a large range of loading rates (at least two orders of magnitude), the hardness and modulus exhibit no size effect, i.e., they remain approximately constant throughout the depth range (150~250 nm). To confirm these results, an additional test was carried out using the CSM method. Similarly, the continuous hardness and modulus, also shown in Fig. 4.11d, hold constant over the depth range from 100 nm to 250 nm. Hardness and modulus beyond this range are not considered since experimental artifacts become increasingly significant. For example, at lower depths, the surface oxidation and tip blunting will play a more significant role; while at deeper depths, the substrate effect will come into play.

The continuous modulus fluctuates around 105 GPa, very close to the result (~100 GPa) by Chou *et al* [206] who fabricated ~2 um thick thin films of the similar composition on Si substrates. In comparison, Lee *et al* [207] reported the nanoindentation modulus of bulk $Cu_{50}Zr_{50}$ to be about 70 GPa. Most recently, Guo *et al* [208] measured a thin film (161 nm thick) of similar composition deposited on a free-standing SiN cantilevers (228 nm thick) using the force-deflection method and found the modulus to be only 50 GPa.

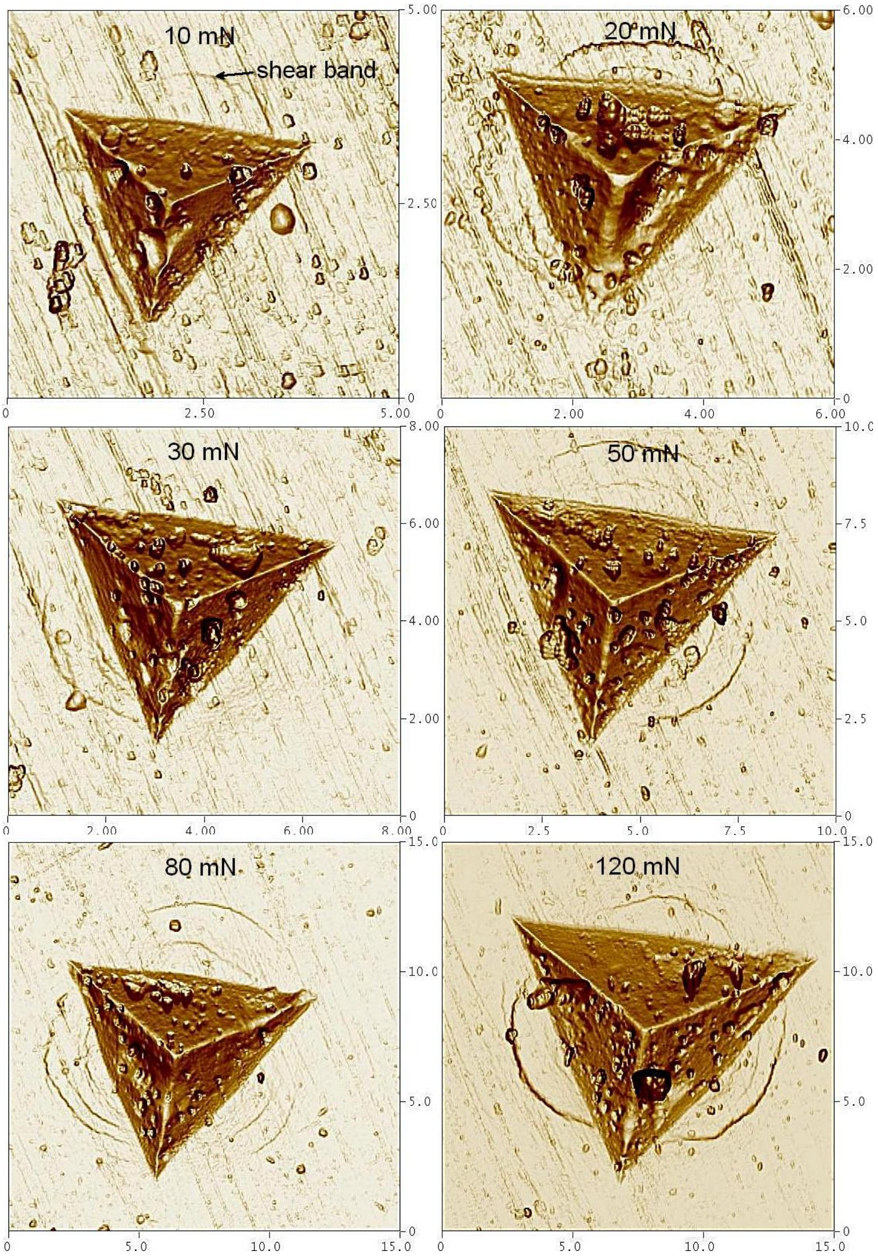

Figure 4.12 AFM images of remnant impressions generated by applied indentation loads ranging from 10 to 120 mN. Shear bands occur for all the loads. The dimension is measured in μm.

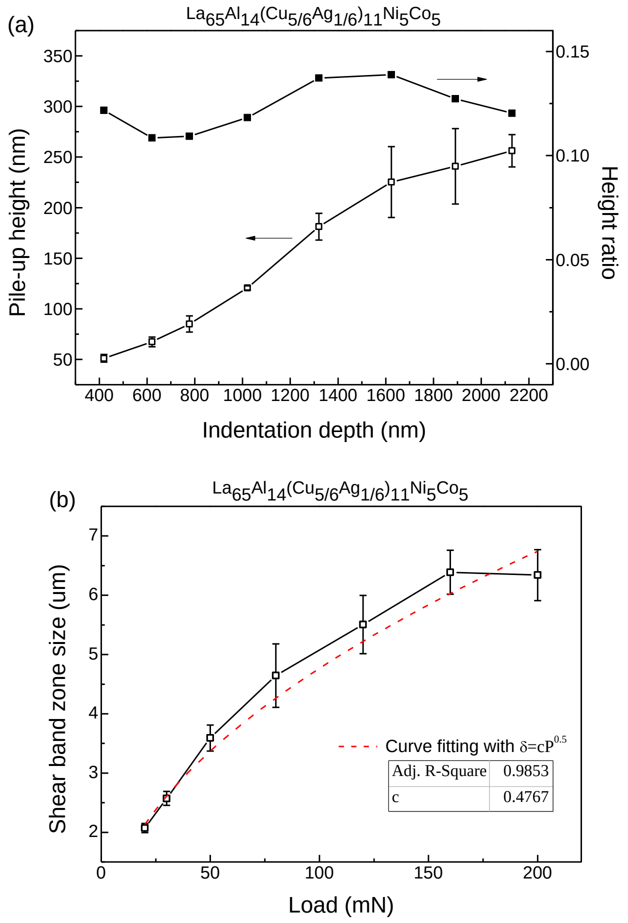

Figure 4.13 (a) The depth dependence of pile-up height and height ratio for $La_{65}Al_{14}(Cu_{5/6}Ag_{1/6})_{11}Ni_5Co_5$. (b) The shear band zone size as a function of indentation load.

To see if the hard substrate contributes to the large modulus, thin films were also grown on soft glass and continuous modulus was recorded (the plot is not shown for brevity). A plateau is usually observable above the indentation depth of 100 nm where the modulus reaches about 100 GPa. In addition, Saha and Nix's method [197] was applied to the current test so as to minimize the substrate effect and the modulus was recalculated to be around 100 GPa. Thus, the big difference in modulus most likely arises from the big difference in sample fabrication process and measurement techniques.

The SGP model by Yang *et al* [80] predicts that the ratio of the indentation hardness to the Young's modulus (H/E) is inversely proportional to the indentation depth, which has been verified by the nanoindentation on a Zr-based bulk MG within the depth range of 25~200 nm [209]. For the current case, however, rather than increase with increasing reciprocal of the depth as suggested by the SGP model, the ratio appears nearly invariable, i.e., this composition does not have an ISE. According to Eqs. 4.20 and 4.21, the absence of ISE is phenomelogically attributable to the negligibly small material length scale.

The PSR model has been successfully applied to both crystalline and amorphous materials [81, 202, 203]. Within the PSR framework, the surface friction is expected to play a significant role in determining the mechanical properties in nanoindentation especially at the nanometer scale due to the large surface/volume ratio. When the indenter is driven into the surface, the friction acts against the indentation load and makes it necessary to apply a larger force than in the case without friction at an equivalent depth. According to the PSR model, the ratio of indentation load to displacement (P/h) is a linear function of displacement as defined below:

$$\frac{P}{h} = a_0 + a_1 h \tag{4.22}$$

where a_0 is a constant describing the frictional resistance, and a_1 is a coefficient related to the load-independent micro-hardness. The fitting values for a_0 at loading rates of 0.01, 0.1 and 1 mN/s are respectively 9.53×10^{-3}, 8.95×10^{-3} and 9.8×10^{-3} mN/nm, which are independent of loading rates and indicate that the frictional effect on indentation load should be remarkably small. As the thin films in this work have a very low frictional effect coefficient, the friction is thought not to contribute to the ISE. One can notice that, even without the frictional effect, the curve can be well fitted by a linear function. The fitting values for a_1 at the above loading rates are respectively 99, 121, and 126 GPa. This increasing trend is in good agreement with the results in Figs. 4.9g and 4.10b.

4.5.3 Elevated temperature

Rather than discuss the mechanical properties with respect to the temperature, it is more useful to describe them in relation to the indentation depth at various temperatures. The mechanical properties of the amorphous thin films $Cu_{50}Zr_{50}$ were calculated with the Oliver-Pharr method and their temperature dependence is illustrated in Fig. 4.14. The contact compliance is generally defined as the ability of materials to resist the indentation load at the surface contact point, which is contributed by both the materials being tested and the instrument itself. It decreases nonlinearly with increasing indentation depth. The thin films, as they heat up, exhibit a larger compliance, smaller hardness and modulus, which is related to the thermal expansion and increasing amplitude of atomic vibration. Apparently, the hardness holds almost constant throughout the depth range at all the test temperatures, while the reduced modulus remains nearly invariable and decreases with increasing depth more significantly at higher temperatures. The H/E_r with respect to $1/h$ at elevated temperatures is calculated and presented in Fig. 4.14d. Unlike the trend predicted by the SGP model where H/E increases with an increasing depth [80], the ratio attenuates inappreciably at room temperature and moderately at higher temperatures, which may imply that there should remain some other mechanisms contributing to the ISE.

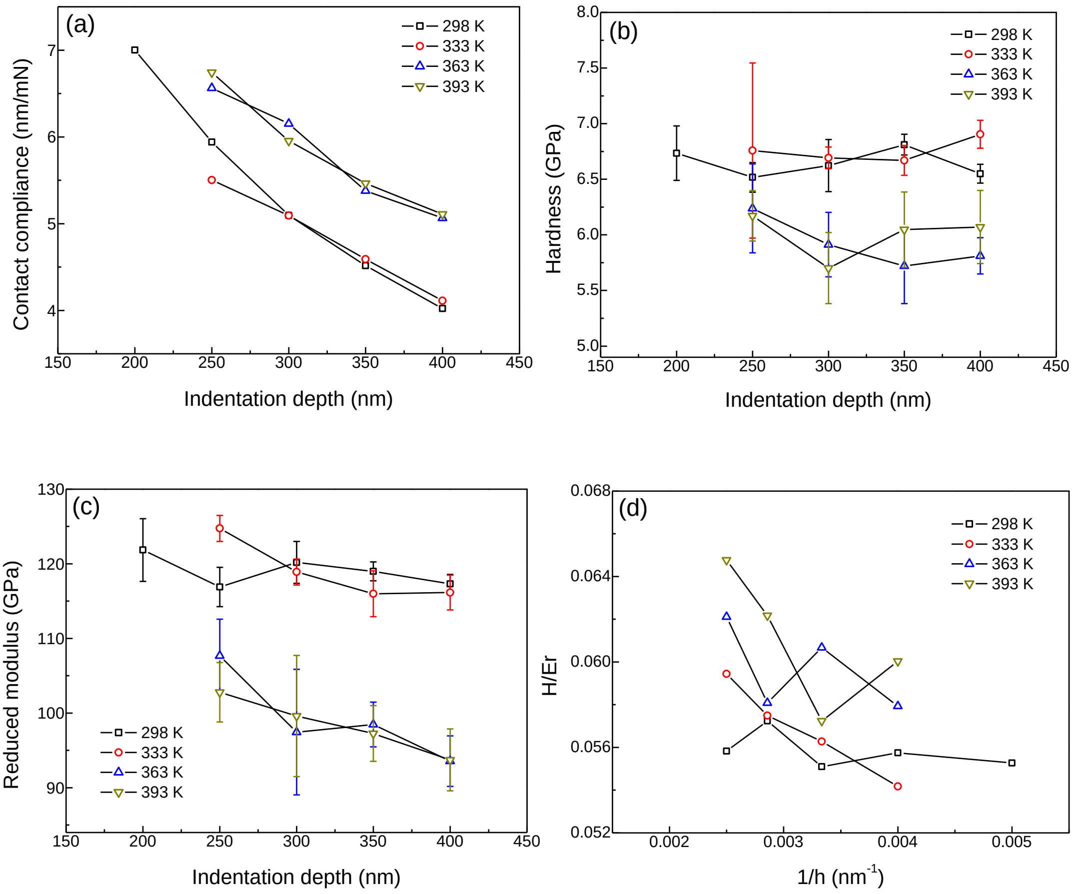

Figure 4.14 Temperature effects on (a) contact compliance, (b) hardness, and (c) reduced modulus. (d) Hardness/modulus ratio as the function of the inverse of the indentation depth.

4.5.3.2 Substrate effect

The thin films were grown on Si (100) substrates and then attached to an aluminum stage with a high-temperature ceramic adhesive. The measured hardness and Young's modulus for Si (100) at room temperature are 12 (±0.5) and 179 (±8) GPa respectively, significantly larger than the thin films (~6.8 and ~120 GPa). The substrate effect from Si can thus be excluded because otherwise the composite hardness and modulus may increase as the substrate effect becomes more significant at steeper indentations. Could the substrate effect arise from the adhesive? If that is the case and the adhesive is softer than the thin films, the composite hardness and modulus could both decrease with increasing depth. To survey the soft substrate effect, thin films on cover glasses (6.4 GPa for hardness and 72 GPa for modulus) were fabricated. The hardness and modulus were continuously and repeatedly measured five times on an MTS Nanoindenter® XP system, which is shown in Fig. 4.15. It is observed that both hardness and modulus hold constant below 500 nm, implying the insignificant substrate effect. Hence, the constant hardness and reducing modulus at high temperatures in Figs. 4.14b and c suggest the negligible influence of the substrates.

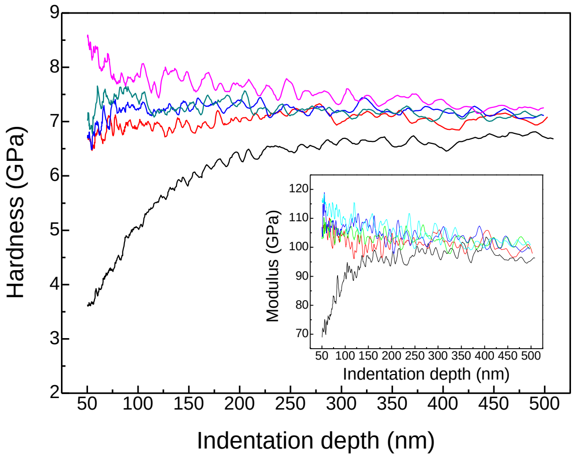

Figure 4.15 Depth dependence of hardness and modulus of the thin film specimen deposited on a glass cover.

4.5.3.3 Surface effect

As early as in 2002 [210], it was realized that the SGP might not be sufficient to explain the ISE especially at very shallow indentation depths, because the surface effect would play a pivotal role at such small length scales. The source of this effect can be either surface friction, or surface-to-volume ratio, hence leading to two various models. One model is termed as the PSR where the surface friction between the indenter facets and the material test is considered to play some part in ISE. This frictional effect has been experimentally proven to exist in metals and introduced here to understand the ISE in MGs. As the model suggests, the ratio of indentation load to displacement (P/h) is positively proportional to the indentation displacement. Presented in Fig. 4.16 are the curves of P/h vs h at elevated temperatures, which can be well fitted with Eq. 4.22. Although the frictional term a_0 apparently increases as the temperature ascends, its remarkably small value may suggest that the surface friction should have a negligible influence on the ISE. The insignificant frictional effect is attributed to the good surface quality of the thin films.

The other model takes into account the surface-to-volume ratio, i.e., the projected contact surface to the volume of the plastic deformation zone. The plastic zone beneath the indenter is assumed to have a hemispherical geometry, the radius δ of which is well described by Johnson's spherical cavity model as expressed in Eq. 4.19.

For plastic contacts of a spherical tip, Gerberich *et al* [210] naturally arrived at the ISE. Following their concept while replacing the spherical contact area with the Berkovich contact area, the surface-to-volume ratio is defined as:

$$\frac{S}{V}=\frac{24.5h_c^2}{(2/3)\pi\delta^3} \tag{4.23}$$

where h_c is the contact depth beneath a Berkovich indenter, the projected contact area of a perfect Berkovich tip is $24.5h_c^2$. The volume of the plastic deformation zone is $(2/3)\pi\delta^3$.

By using the projected contact area, the mean contact pressure or hardness H is determined as:

$$H=\frac{P}{A}=\frac{P}{24.5h_c^2} \tag{4.24}$$

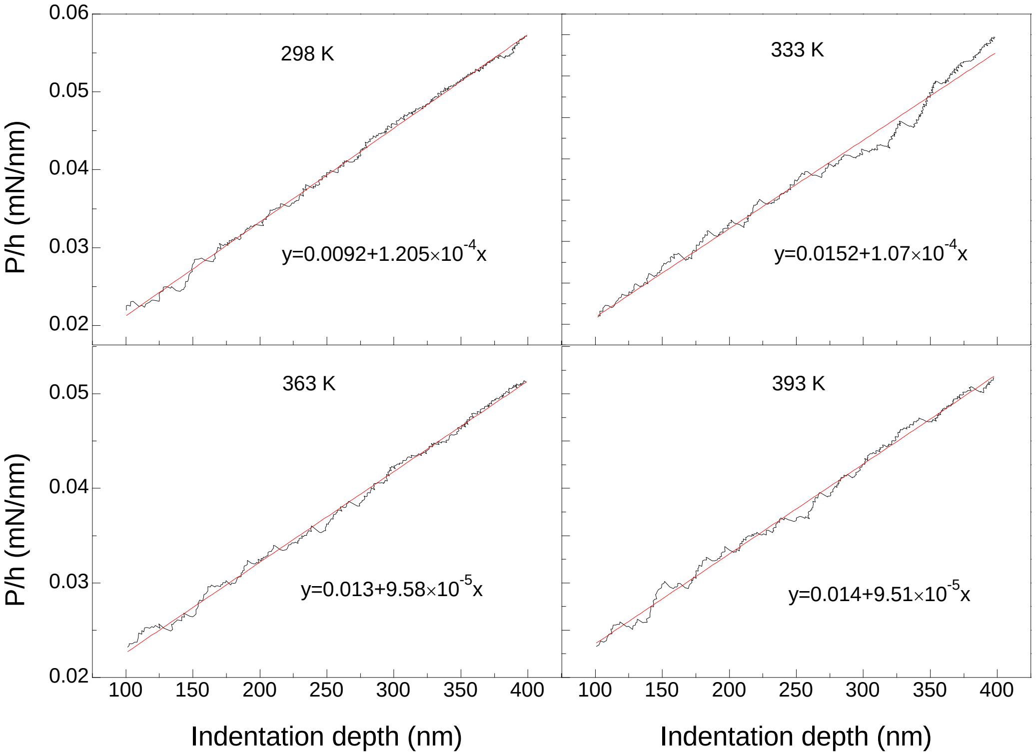

Figure 4.16 The ratios of load to depth with respect to the indentation depth at elevated temperatures.

Based on these equations, load P is eliminated and hardness H rewritten as:

$$H = \frac{1.28\sigma_y}{\left(\frac{S}{V}\right)^{2/3}} \times \frac{1}{(24.5h_c)^{2/3}} \tag{4.25}$$

It can be seen that hardness is related to both indentation depth and surface-to-volume ratio. Gerberich *et al* [210] reformulated the ratio as a function of a/c (a is the contact radius under a spherical contact, a/c is considered to remain constant) and thus the surface-to-volume ratio could be constant through a few hundred nanometers in their single crystalline specimens. Taking the assumption as correct for MGs, hardness definitely falls off as the depth increases. The two-third power is approximate to the squared root of the depth as predicted by Yang *et al* [80]. This effect results in an ISE and is insufficient to interpret the decreasing modulus because the minimum indentation depth is 200 nm, which is large enough to rule out the effect of surface atoms on the modulus. Could the modulus be artificially measured because the area function is only calibrated at room temperature? To avoid this problem, H/E_r^2 as the function of the indentation depth is plotted in Fig. 4.17. This ratio does not depend on the area and is considered to depict the true hardness variation in the case of constant modulus [211]. Clearly, the ratio increases negligibly at room temperature and more significantly at higher temperatures.

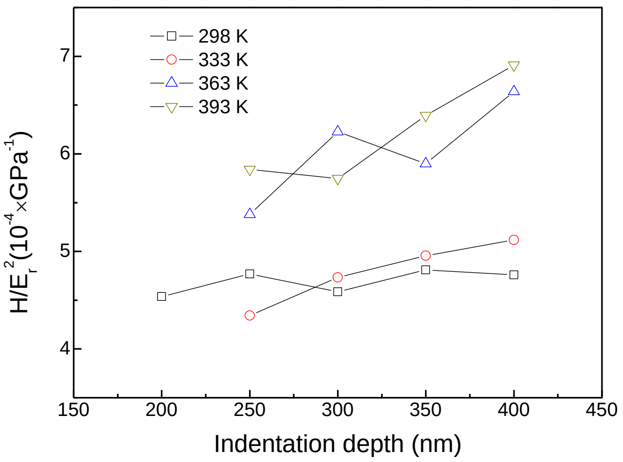

Figure 4.17 Variation of H/E_r^2 with indentation depth.

4.5.3.4 <u>Nanocrystallization effect</u>

As discussed above, the substrate and surface effects cannot satisfactorily explain the variation in hardness and modulus. Nanocrystallization could contribute to the ISE inversely, i.e., hardness most commonly increases as nanocrystallites form beneath the indent [82, 212]. The hardening mechanism in MGs, as in crystalline materials where it is largely determined by the dislocation mobility, lies in the shear banding activity. The precipitated nanocrystallites or the residual glassy matrix can enhance the hardness by either interrupting the shear banding paths or improving their shear resistance. The occurrence of nanocrystallization is made possible by either local thermal events or mechanical stress. In this study, with the assistance of both heat and stress, the region below the indentation is more prone to crystallization at a higher temperature. Moreover, the volume fraction of the crystallites increases at a greater depth. Fig. 4.18 refers to the residual impression made at the indentation depth of 2500 nm by room-temperature nanoindentation. The white particles emerge on both the indent surface and the edges of the SBs, one of which denoted by a circle in Fig. 4.18 takes on an EDX pattern similar to the designed composition. Besides, the peripheral area of the indent is all clear of particles. From these facts it is inferred that the particles are not contaminants but most possibly nanocrystallites. Therefore, the hardness increase is the result of precipitation strengthening against the deformation-induced softening [213]. Temperature rise favors atomic diffusion and free volume annihilation. The softening effect can be attenuated at higher temperatures, which in turn makes the hardening effect more noticeable.

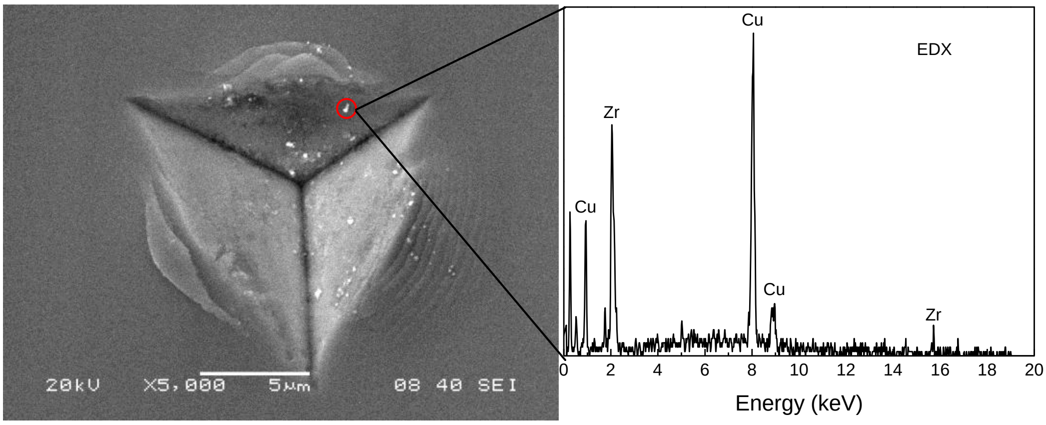

Figure 4.18 SEM image of an indent remaining after load removal at the indentation depth of 2500 nm. The nanoindentation testing is operated at room temperature. The white particles located on the indent surface or the edges of the SBs are supposed to be nanocrystallites, one of which encircled is analyzed by EDX (given on the right) and shows the composition similar to the as-prepared specimen.

4.6 Effects on creep behavior

The flow stress or hardness varies with strain rate, which is expected as the consequence of the time-dependent properties of materials. Creep testing, which subjects the materials to a fixed load for a period of time, is widely used to characterize this time-dependent behavior. Compared with the other creep techniques, indentation creep is especially useful in two respects: on the one hand, it is readily performed on a small length scale; on the other hand, it can be applied particularly to hard, brittle materials without making cracks or fracture.

4.6.1 Loading rate dependence

Given in Fig. 4.19 are the representative *P-h* curves at various loading rates with a holding time of 100 s, which are displaced from each other for clarity. Looking at the hold portion of the *P-h* curves, it is noted that as the load is held constant, the displacement appears to increase as a function of time and loading rate, i.e., the higher the loading rate is, and so will be the hold displacement, when the total hold period remains fixed. Later it is realized that the total creep displacement is somewhat affected by the *instantaneous plasticity* [198] in the first 1-3 s of the hold segment. The instantaneous deformation is most likely due to the loading ramp [198] and becomes more significant at higher loading rates. The comparison of the creep displacements before and after correction of such effect is shown in Fig. 4.20. The insets in Fig. 4.20 describe the corrected loading rate dependence of hold displacement at the peak loads, where the difference in the hold displacement between the lowest and highest loading rates is about 1.3 nm for Zr-based alloy and 2.0 nm for $Cu_{49.3}Zr_{50.7}$. For Zr-based sample, except at the lowest loading rate, the hold displacement remains almost constant, which results from the insignificant viscoelasticity, in agreement with the hardness tests discussed in Figs. 4.9d and 4.10a. For $Cu_{49.3}Zr_{50.7}$, even though the instantaneous effect is removed, the hold displacement still increases as the loading rate is increased. This creep-like behavior has been revealed in a Pd-based BMG, where a large difference of about 10 nm in the creep displacement was observed [214]. The hold displacement appears to be linearly proportional to the logarithm of loading rates, similar to the trend discovered in the creep-time relationship [198].

The plastic deformation of MGs is a very local event occurring in shear bands which is associated with free volumes. As proposed by Spaepen [55], the free volume is created under a high shear stress by squeezing atoms from one position into another, and tends to be annihilated by the subsequent relaxation process due to atomic diffusion. In the steady state, the equilibrium defect concentration is reached because the creation rate of the free volume is equal to the annihilation rate of the free volume. The two competing processes are kinetic and thus influenced by the loading conditions, for example, the loading rates. As the concentration reaches a critical amount, the free volume accumulates into a shear band.

As for the indentation tests under the load control mode, the amount of free volume and thus plastic deformation during loading segment is related to the loading rates. At the lowest loading rate, the necessary excessive free volume is created to accommodate the strain, and the plastic deformation can be mostly achieved in the loading process. Therefore, the displacement in the holding segment is hardly observed. At higher loading rates, the creation rate of the free volume is much larger than its annihilation rate, while the time is less than sufficient to bring the system into the equilibrium defect concentration, and thus the equilibrium plastic deformation conditions. In addition, free volume is restricted from coalescing into a shear band at high loading rates. For these reasons, at higher loading rates, a smaller amount of time-dependent plastic deformation takes place during the loading segment, and a larger amount recovers during the holding segment.

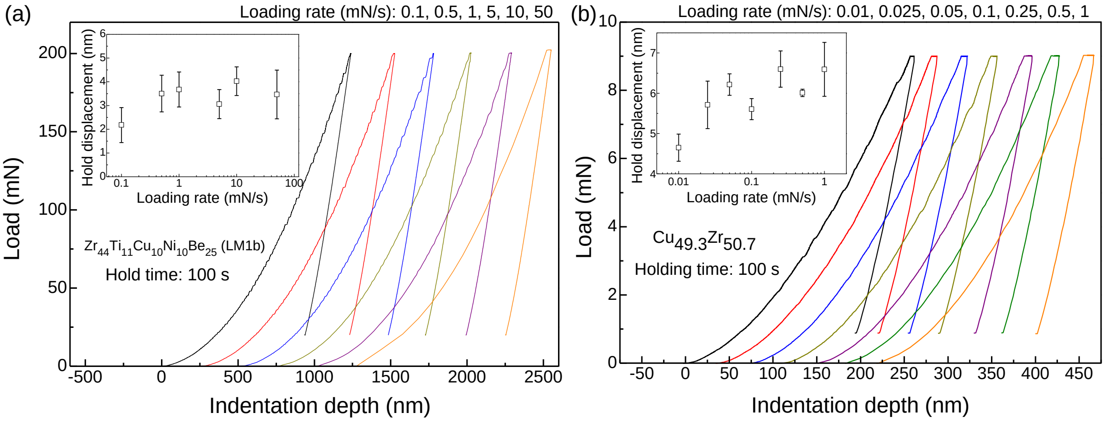

Figure 4.19 The load-displacement curves at various loading rates for (a) $Zr_{44}Ti_{11}Cu_{10}Ni_{10}Be_{25}$ (LM1b) and (b) $Cu_{49.3}Zr_{50.7}$. The insets show the loading rate dependence of the corrected hold displacement by excluding the *instantaneous plasticity*.

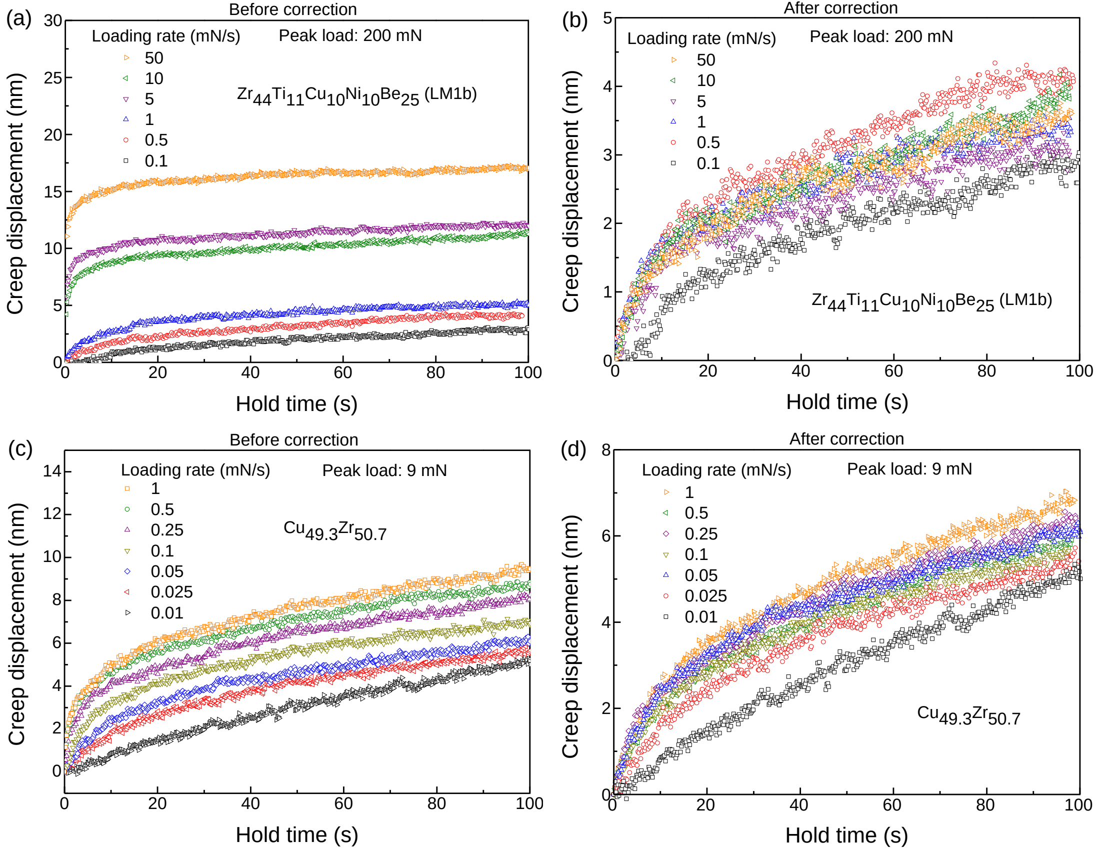

Figure 4.20 The creep displacement as a function of holding time before and after correction of the *instantaneous plasticity* in the first 1-3 s of the holding segment.

The viscoelastic flow (accurately, the anelastic component [198, 215]; however, the viscoplastic component [198, 215] is not able to be distinguished in this study and thus the term *viscoelastic* is used) during the constant-load portion can be approximated as one single process [184]:

$$h(t) = h_0\left[1 - \exp\left(-\frac{t}{\tau_0}\right)\right] \tag{4.26}$$

where t is the time, h_0 and τ_0 are respectively the indentation depth at $t \to +\infty$ and the characteristic relaxation time. Applying the equation to the corrected creep displacement curves in Figs. 4.20b and d, the good fit parameters are generated and cited in Table 4.2. To ensure a good fit, the parameters are initialized, followed by iteration until the fit is converged. For each composition, no matter what the loading rate is, τ_0 remains alike for all the creep tests, implying the same flow mechanism [184]. The ultimate penetration depth, h_0, is also similar for all the tests. The relaxation time at room temperature for Zr-based MG is slightly shorter than that for $Cu_{49.3}Zr_{50.7}$, suggesting the approximate activation energy for both of alloys (for interpretation, refer to the discussion in the following section on elevated temperature). This finding is in accord with the similar STZ activation energy for the two glasses (131 kJ/mol for Zr-based alloy, and 122.7 kJ/mol for $Cu_{49.3}Zr_{50.7}$, quoted in Table 5.3), as the anelastic deformation at low temperature is driven by the mechanism analogous to the reversible relaxation upon annealing below the glass transition temperature which is determined by the STZ operation [216]. The penetration depth at the infinite time for Zr-based MG is almost twofold smaller than that for $Cu_{49.3}Zr_{50.7}$, which is attributable to the larger elastic modulus of the former than that of the latter.

Table 4.2 The parameters derived by fitting the corrected creep displacement curves with Eq. 4.26. The values at the lowest loading rate are not given because they are unreliably large.

Composition	Loading rate (mN/s)	Fitting parameters	
		τ_0 (s)	h_0 (nm)
$Zr_{44}Ti_{11}Cu_{10}Ni_{10}Be_{25}$ (LM1b)	0.5	24.2±7.0	3.4±0.7
	1	23.1±7.6	3.3±0.7
	5	23.3±5.7	2.8±0.6
	10	26.0±2.6	3.6±0.5
	50	25.4±2.5	3.2±0.7
$Cu_{49.3}Zr_{50.7}$	0.025	33.8±4.1	5.7±0.7
	0.05	29.8±2.8	5.6±0.6
	0.1	30.9±3.3	5.2±0.4
	0.25	29.5±5.3	6.1±0.4
	0.5	28.1±3.6	5.8±0.6
	1	30.8±3.3	6.0±0.5

Although the one-single-process model can reveal useful information (i.e., relaxation time), it does not well describe the overall creep behavior especially at larger depths (see the solid fitting lines in Fig. 4.21). The generalized Kelvin model, which simplifies the viscoelastic flow as a series of springs and dashpots and has been successfully applied to MGs [198, 215], is an alternative to fitting the creep data:

$$h(t) = h_e + \sum_{i=1}^{n} h_i \left[1 - \exp\left(-\frac{t}{\tau_i} \right) \right] \tag{4.27}$$

where h_e is the displacement of the first spring, h_i and τ_i (i=1, 2) correspond to the displacement and relaxation time of the i-th process. Apparently, this model recognizes the multiple processes during the viscoelastic flow and can do a perfect fit to the experimental curves as indicated by the dashed lines in Fig. 4.20. The fitting parameters are not shown because they are independent of loading rates as reported in Table 4.2.

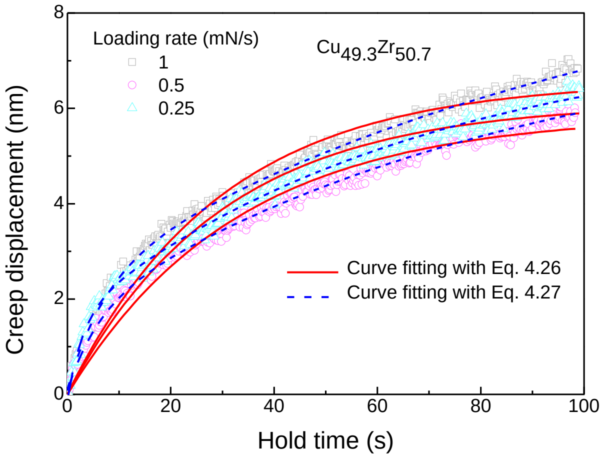

Figure 4.21 Fitting of the creep displacement curves with two equations. The dashed curves calculated from Eq. 4.27 appear to fit the experimental data better than the solid curves from Eq. 4.26.

Based on Eq. 4.27, the spectra of relaxation times can be inferred:

$$L(\tau)=\sum_{i=1}^{n}\left[\left(1+\frac{t}{\tau_i}\right)\frac{h_i}{\tau_i}\exp\left(-\frac{t}{\tau_i}\right)\right]\frac{A_0}{P_0 h_\mathrm{m}}\Bigg|_{t=2\tau} \tag{4.28}$$

where A_0/P_0 is the inverse of the hardness, and h_m is the maximum indentation depth. Each anelastic flow is characterized by a relaxation time and connected to the activation of local shearing movements at defective regions (e.g., STZs) [198, 217]. Fig. 4.22 illustrates the spectra of the two MGs. Each composition has two broad peaks, indicating the distributed anelastic deformations and among them two primary ones. The peak positions of Zr-based alloy (i.e., 10.2 and 109.8 s) are lower than the corresponding ones of $Cu_{49.3}Zr_{50.7}$ (i.e., 16.8 and 174.6 s), in agreement with the results calculated from Eq. 4.26. The lower peak intensity for Zr-based MG than for $Cu_{49.3}Zr_{50.7}$ may suggest that the former is in a more relaxed state. This is the natural outcome of the different manufacturing processes, i.e., the liquid quenching for Zr-based MG and the sputtering deposition for $Cu_{49.3}Zr_{50.7}$; the latter is usually expected to have a faster cooling rate than the former and therefore a larger number of defects would be trapped by the sputtering process. It is already agreed that the structural relaxation should reduce the defect concentration and then embrittle the MGs. In other words, the high defect concentration favors the plasticity (also refer to Section 5.6 in Chapter 5 for more details).

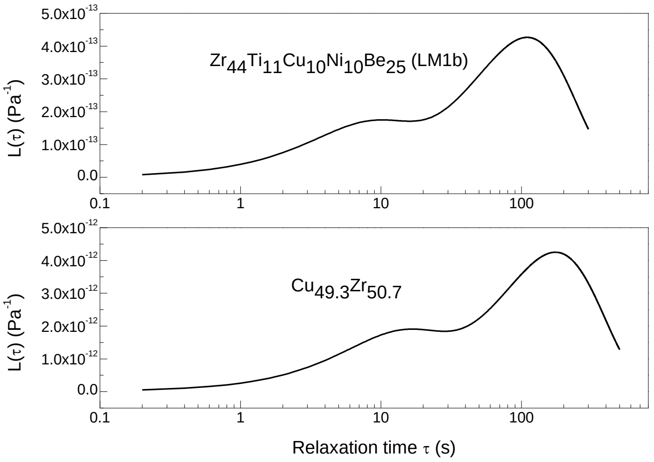

Figure 4.22 The relaxation time spectra for the two glasses. The Zr-based alloy is lower in peak intensity than $Cu_{49.3}Zr_{50.7}$, suggesting that the former is more relaxed.

Besides the use in relating the relaxation spectrum to the microscopic process, the creep testing can also measure the strain rate sensitivity of the hardness:

$$m_H = \frac{\partial \ln H}{\partial \ln \dot{\varepsilon}} \tag{4.29}$$

This quantity is of great use in the way of estimating the STZ size and then correlating it with the plasticity of MGs [67, 218] (also refer to Section 5.6.1 in Chapter 5). The measurement is realized according to the knowledge that the hardness and strain rate both change continuously during the creep. The hardness and strain rate are measured when either the indentation area or the depth is known. However, it is not straightforward for the creep to calculate the area with the Oliver-Pharr method because the method does not hold true during the creep, specifically, the depth dependence of area for the creep does not follow the square-root relation as found for the loading but the power law relation with an exponent depending on hardness/modulus [219]. Nevertheless, it is easy and acceptable to keep using the square-root formulation in this work, and the sensitivity here qualitatively characterizes the ability of materials to resist the creep deformation. In calculating the area, the contact depth is used and the strain rate at each creep depth is the derivative of the fitting curves for the experimental creep data shown in Figs. 4.20b and d. Given in Fig. 4.23 is the strain rate dependence of the hardness on a log-log scale for the steady-state creep. The m_H has remarkably small values, close to that of the other MGs measured at room temperature [67] and consistent with the unidentified loading-rate-dependence of the hardness investigated above. This implies the almost perfect plastic deformation in the inhomogeneous flow. The sensitivity remains unchanged for different loading rates. Zr-based alloy has a far smaller m_H than $Cu_{49.3}Zr_{50.7}$, indicating that the former is less viscoelastic and more creep-resistant than the latter.

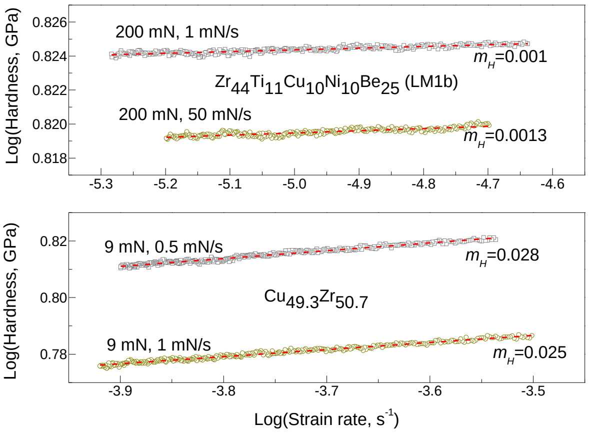

Figure 4.23 Strain rate dependence of the hardness for the two glasses at various loading rates. The m_H values are extremely low and do not vary with loading rate.

4.6.2 Indentation size effect

As the penetration is pushed on, the volume of plastic deformation grows and more defects would be involved. Thus, the indent size could affect the creep deformation. The ISE on creep behaviors is presented in Fig. 4.24, where the insets describe the depth dependence of the corrected hold displacement by excluding the *instantaneous plasticity*. For the Zr-based alloy, the little size effect within the experimental error can be observed, which is the result of the unnoticeable viscoelasticity; while for $Cu_{49.3}Zr_{50.7}$, a significant ISE occurs, i.e., the specimen creeps more at higher loads. These findings agree well with the prior reports of this chapter. It is worth noting that the creep deformation at the lowest load is not fully developed particularly for $Cu_{49.3}Zr_{50.7}$. This can be interpreted in terms of fewer defects covered at smaller loads and thus fewer anelastic processes activated. The strain rate dependence of the hardness only for $Cu_{49.3}Zr_{50.7}$ is plotted in Fig. 4.25, because the ISE in the Zr-based alloy is fairly weak. Interestingly, although the creep displacement exhibits a clear size effect, the strain rate sensitivity is not strongly influenced by the indent size. The difference between the low and high loads may arise from the not-well-developed steady-state creep at high loads due to the insufficient holding time. Puthoff *et al* [218] have looked into the broadband nanoindentation creep on two BMGs and found their strain rate sensitivity to be similar across the load range.

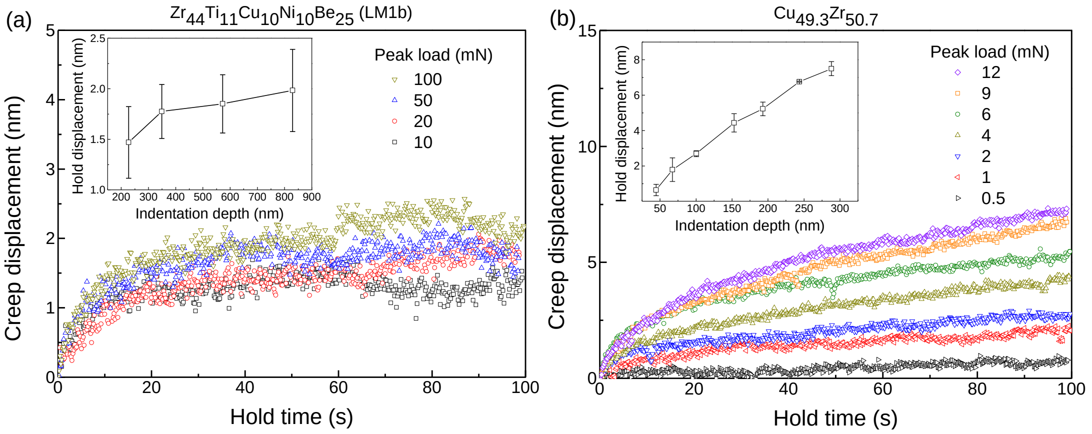

Figure 4.24 Creep displacement versus hold time at various loads corrected by eliminating the *instantaneous plasticity*. The loading/unloading rates for all the tests are 1 mN/s. Insets: total hold displacement as a function of indentation depth. Due to the absence of viscoelasticity, the Zr-based alloy has little size effect within the load range; while $Cu_{49.3}Zr_{50.7}$ shows a significant ISE.

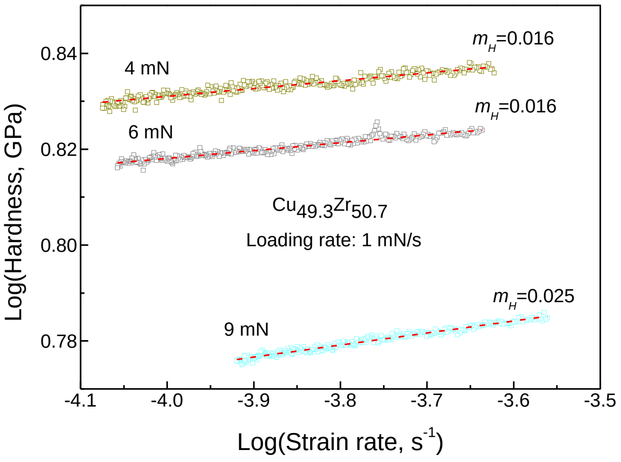

Figure 4.25 Strain rate dependence of the hardness at various loads for $Cu_{49.3}Zr_{50.7}$.

4.6.3 Elevated temperature

The plastic flow at low homologous temperatures is thermally activated. The activation process takes place by the hopping of elementary units (e.g., STZ) from one energy configuration to another and undergoes a characteristic time length, termed relaxation time. According to the activation energy spectrum model [184, 217], the relaxation time for the process is exponentially related to the activation energy:

$$\tau = \tau_0 \exp\left(\frac{Q}{k_B T}\right) \tag{4.30}$$

where τ_0 is a reverse attempt frequency, k_B is the Boltzmann constant, Q is the activation energy, and T is the absolute temperature. Straightforwardly, the longer τ corresponds to the larger Q and the relaxation time drops as the temperature is increased. The creep deformations at elevated temperatures are surveyed by holding the indenter at different maximum indentation depths (300, 350, and 400 nm) for 60 s, of which the ones at 400 nm are shown in Fig. 4.26 and fitted with Eq. 4.26. The fitting parameters for all the tests are listed in Table 4.3. Not surprisingly, since the viscoelastic flow becomes easier at higher temperatures, the final indentation depth h_0 increases as the temperature rises, in agreement with the experimental values. However, in the work by Concustell *et al* [184], the contrary results were reported, which was explained by them in terms of less relaxation times at higher temperatures and therefore larger portion of anelastic recovery in the loading. The reason for the discrepancy is believed to lie in the thermodynamic state of the as-prepared samples and the testing conditions, for example, it is a bulk material prepared by copper mould casting and 150 s for the holding duration in the literature work [184] while here it is a thin film deposited by magnetron sputtering and 60 s for the holding duration. It is already known that the anelastic flow covers a spectrum of activation energies and short loading time (<100 s) results in a poorly developed spectrum because the anelastic processes with long relaxation time are not all activated and thus they do not contribute to the creep deformation. This interpretation may also be applicable to the similar characteristic relaxation times in Table 4.3, regardless of the indentation depth and test temperature.

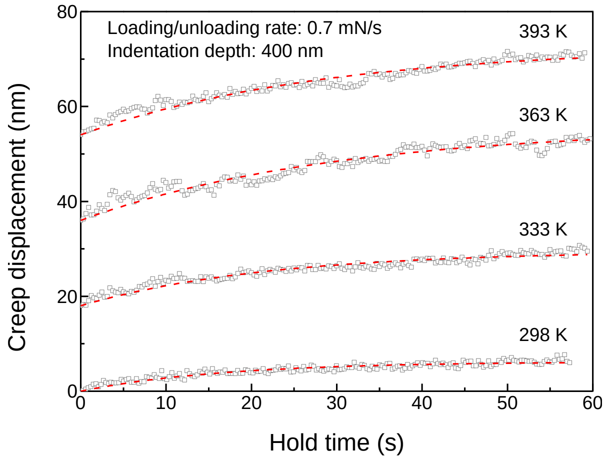

Figure 4.26 The creep displacements of $Cu_{50}Zr_{50}$ thin films at elevated temperatures recorded at the maximum indentation depth of 400 nm. The experimental curves are fitted with Eq. 4.26.

Table 4.3 Effects of temperature and the maximum indentation depth (300, 350, and 400 nm) on the relaxation time τ_0 and the ultimate penetration depth h_0 during the creep testing.

Temperature (K)	Fitting parameters					
	τ_0 (s)			h_0 (nm)		
	300 nm	350 nm	400 nm	300 nm	350 nm	400 nm
298	24.8±9.1	16.1±1.7	17.7±4.7	6.9±1.8	6.4±1.8	6.4±0.6
333	20.3±6.5	19.1±1.3	25.6±4.2	9.0±1.4	10.5±1.8	10.0±2.1
363	23.0±7.4	19.2±3.0	25.3±9.2	15.3±8.6	13.3±2.6	17.1±2.5
393	21.1±4.8	18.3±6.4	21.7±7.0	23.0±4.1	15.6±3.8	13.6±5.6

4.7 Summary

As MGs consist of both solid-like and liquid-like regions, they exhibit viscoelasticity. A viscoelastic model was first formulated, which definitely states that the elastic behavior and mechanical properties of MGs could be influenced especially by low loading rates (0.1 mN/s in this study). Following this model, the effects of loading rate, indentation size and elevated temperature are fully investigated by instrumented nanoindentation on three MGs (i.e., $La_{65}Al_{14}(Cu_{5/6}Ag_{1/6})_{11}Ni_5Co_5$, $Zr_{44}Ti_{11}Cu_{10}Ni_{10}Be_{25}$, and $Cu_{49.3}Zr_{50.7}$) chosen from the nine compositions surveyed in Chapter 3. These compositions are expected to be representative because they sweep a range of glass transition temperatures from low ones close to 100 ℃ to high ones around 450 ℃. It should be added that the high-temperature nanoindentaion was performed only on $Cu_{50}Zr_{50}$ (similar to $Cu_{49.3}Zr_{50.7}$ and within the instrumental error for EDX attached on SEM) because it is somewhat time-consuming (load zeroing, calibration, and temperature equilibration *etc*.) and not always available for research use (the facility was built to first serve the industrial projects).

The load-displacement (*P*-*h*) curves for all the three MGs show resemblance in the following aspects. Firstly, the loading traces at the lowest loading rates are interrupted by displacement bursts, and this discontinuous behavior is commonly referred to as serrated flow, which has been related to the shearing movement of single shear bands in the literature. Secondly, the serrated flow is strongly dependent on the loading rates, specifically, it becomes more prominent as the loading rate decreases. There exists a critical loading rate differing across the composition, above which the serrated flow does not occur. Two reasons may account for the absence of the load serrations: one is the limited instrumental resolution and the other is the deformation mechanisms changing from the operation of single shear bands at the lowest loading rate to the concurrent operation of multiple shear bands at the highest loading rate. Thirdly, the pile-up height and the shear band zone size are both independent of loading rates, indicating that the pile-up effect might contribute equally to the measurement and that the mechanical properties are not sensitive to the loading rates. Lastly, the displacement burst length generally increases as the indent size grows. However, the bursts with small length can be found even at large depths, which is likely due to the fewer defects remaining after the annihilation of more defects in the previous shear band operation. High-temperature nanoindentation reveals that the loading profiles appear more serrated with rising temperature because the strain rate mismatch at higher temperatures between the matrix and the shear banding zone is more difficult to be developed.

The loading rate dependence of mechanical properties such as hardness and modulus differs from one composition to another. For the La- and Zr-based alloys, their mechanical properties lack loading rate effect over the loading rate range; for $Cu_{49.3}Zr_{50.7}$, the hardness and modulus both increase as the loading rate increases up to 0.1 mN/s and then remain almost constant. Thus, it is concluded that the loading rate effect is not present above a critical indentation rate because the viscoelastic effect is not significant. To further ensure the nanoindentation results, AFM was used to calculate the hardness for the La- and Zr-based alloys by imaging the residual area, and again found no variation in hardness. In contrast to the loading rate influence, the indentation size effect, manifested as the enhanced hardness with decreasing indentation depth, is present in the La- and Zr-based alloys, and absent in $Cu_{49.3}Zr_{50.7}$. The La-based MG has a more significant ISE than the Zr-based MG, resulting from the different characteristic material length scales which could be determined by the size of the STZs. AFM measurements reconfirm the presence of the ISE in the La-based MG. It is worth noting that the AFM hardness is usually lower that that by nanoindentation, which is thought to stem from the pile-up effect. Moreover, the pile-up height and shear band zone size both show the positive ISE, while the pile-up height ratio does not. The depth-dependent behavior for the shear band zone size clearly deviates from the Johnson's spherical cavity model, because the model was built without considering the ISE. In regard to the temperature, its impact on the mechanical behaviors is seen by the high-temperature nanoindentation tests on $Cu_{50}Zr_{50}$, specifically, the hardness (exactly, the ratio of hardness over squared modulus H/E^2) remains almost constant over the depth range at room temperature and increases more significantly at higher temperatures. By excluding the effects from the substrate and surface, the nanocrystallization is most likely responsible for the phenomenon, as it can be induced by heat and influence the activity of shear bands.

The nanoindentation creep, determined by the composition, does have dependence on the above-mentioned testing conditions. For the Zr-based MG, due to the insignificant viscoelasticity, the effects of loading rate and indentation size appear to be negligible; while for $Cu_{49.3}Zr_{50.7}$, the creep displacement explicitly increases as either the loading rate or the indent size grows. The creep flow can be well fitted by the one-single-process model or the Kelvin model which recognizes the multiple processes during the creep. Based on the one-single-process model, the relaxation times are estimated. The two alloys have similar relaxation times, suggesting the approximate activation energies for the anelastic flow. Based on the Kelvin model, the relaxation time spectra are derived. Two peaks occur on the spectra, suggesting two primary anelastic processes. The Zr-based MG has a more relaxed state than $Cu_{49.3}Zr_{50.7}$ because the former has lower peak intensity than the latter. The elevated temperature tests on $Cu_{50}Zr_{50}$ reveal the larger creep displacement at higher temperatures. However, the temperature and indentation depth both appear not to affect the relaxation times, which is due to the short holding time (60 s) and thus the anelastic recovery with longer relaxation time is not activated. Besides calculating the relaxation spectrum, the creeping technique here can also qualitatively measure the strain rate sensitivity which characterizes how resistant a material is to the creep deformation. It is found that the test MGs, especially the Zr-based alloy, have remarkably small strain rate sensitivity, in good line with the prior results by normal nanoindentation that MGs are independent of the loading rates. In addition, the strain rate sensitivity remains unaffected by the loading rates and peak loads.

Chapter 5 Correlation between Thermal and Mechanical Properties

5.1 Introduction

It has long been recognized that the thermal and mechanical properties are both interrelated [2], because they are determined by atomic cohesion energy. In addition, the two processes are activated by the movement of atomic clusters. Based on these pioneering studies and by including the other physical factors (e.g., molar volume), their relationship is already quantified in the literature work [94, 178, 220, 221].

In this chapter, based on the work described in Chapter 3 and 4, the correlation between thermal and mechanical properties is explored at first. By referring to a large quantity of literature, the VED effect is observed on the mechanical properties of BMGs covering Mg-, Ca- , Cu-, Ti-, Zr-, Hf-, Fe-, Ni-, Pd- and RE-based (RE for rare earth) systems. More interestingly, plasticity (here, subjected to compressive loading) appears somewhat VED-dependent, i.e., the maximum plasticity preferentially occurs within a certain intermediate VED region, beyond which MGs exhibit very limited or even no plasticity (see Fig. 5.3). Such dependence relation is understood by introducing STZs, based on which, amorphous plasticity near glass transition temperature was established recently [222].

The work in the following sections has been published in [223]

5.2 Correlation between thermal and mechanical properties

Fig. 5.1 presents the relationship between the thermal (i.e., glass transition temperature and fragility index) and mechanical properties (i.e., hardness and shear modulus). Not surprisingly, as predicted in the literature, the positive correlation between the properties is found, exactly, the hardness or shear modulus is enhanced as the glass transition temperature or fragility increases. The scattering of the data points indicates that there exist some other effects (i.e., the molar volume) governing the properties. Nevertheless, the definite relation confirms that the thermal and mechanical processes share the similar mechanisms. In what follows, this relationship is discussed from the viewpoint of valence electron density (VED).

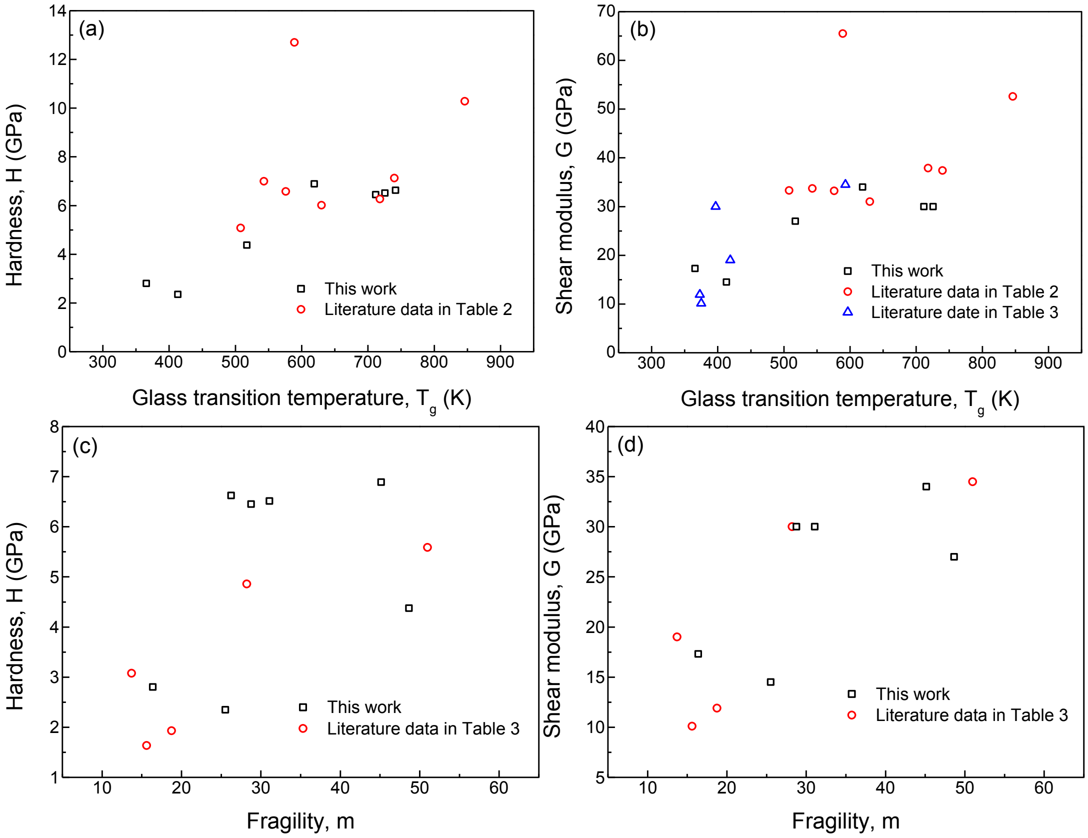

Figure 5.1 Relationship between thermal and mechanical properties: (a) hardness *vs* glass transition temperature, (b) shear modulus *vs* glass transition temperature, (c) hardness *vs* fragility and (d) shear modulus *vs* fragility.

5.3 Correlation between properties and valence electron density

Since discovery in 1960, metallic glasses (MGs) have attracted increasing attention and lots of issues still exist to be explored, the hottest of which might be their mechanical properties because MGs generally have yield strength approaching the theoretical value, large elastic limit (~2%) and very limited plasticity. These unique characteristics are thought to be derived from the unique structure. Unlike crystals, MGs consist of randomly close-packing atoms and thus do not involve crystallographic symmetry and defects. The structural simplicity implies that their properties might be governed only by a few underlying factors—chemical/geometrical short-range orders (SROs), atomic volume, electron density and the likes. Recently a distinct composition dependence of their mechanical properties has been revealed [48, 224-226]. For example, in Cu_xZr_{100-x} amorphous alloys, both the Young's modulus and yield strength gradually increase until the Cu content goes up to 65 at.% and then drop with further addition of Cu, while the plasticity does inversely [226]. This composition-mechanical property trend follows that of the composition dependence of atomic packing density which is an indicator of the structural stability and determined by the SRO atomic configurations [226]. Building on potential energy landscape (PEL), Cheng *et al* [48] provided a physical insight into the structure-property correlation as a result of the evolution of icosahedral ordering, a structure-stabilizing factor for BMGs. As such, the mechanical properties are regarded to be closely related to SRO structures or structural stability.

In conventional crystalline alloys, stability of certain intermediate phases is significantly dependent on valence electron concentration—the number of valence electrons per unit cell, which is known as one of the Hume-Rothery rules. In addition, according to the universal binding energy relation, Rose *et al* [227] and Banerjea *et al* [228] found, for metallic and covalent bonds in a wide range of chemical situations, that the important parameter in determining the bond strength and thus elastic properties is the valence electron density (VED)—the number of valence electrons per atomic volume. Despite the small difference, both concepts are usually interchangeable; the latter will be used throughout this article. In light of these earlier studies, the correspondence relationship between structural stability and mechanical properties of MGs suggests a possible link between VED and mechanical properties.

Table 5.1 presents the summarized data on elastic properties and compressive plasticity of BMGs. The compressive plasticity is characterized by excluding the elastic component from the total strain. All of samples chosen underwent generally similar test conditions (e.g., sample geometry, aspect ratio and strain rate) so as to minimize the extrinsic effects on plasticity.

VED of a metallic glass is calculated by

$$d = \frac{\sum_i x_i e_i}{\sum_i x_i \Omega_i} \tag{5.1}$$

where x_i is the atomic concentration, e_i and Ω_i are respectively the number of valence electrons and atomic volume of pure element i. The e_i values available in [229, 230] are calculated according to the relationship between ionic and atomic radius. The atomic volumes equal those of corresponding elements by assuming that alloys are ideal solid solution. This assumption, although simple, is sufficient to capture the varying behavior of VED with composition [231]. Fig. 5.2 displays the VED dependence of Young's modulus (E), shear modulus (G) and bulk modulus (B), respectively. Not fully surprisingly, these elastic properties scale linearly with increasing VED as observed in metals and compounds [232]. Generally mechanical properties of solids are determined by their elastic properties. Both yield strength and hardness of MGs were found to be linearly proportional to elastic moduli [201]. Hence, it can be expected that these mechanical properties are strongly dependent on VED. Glass transition temperature (T_g) is a key factor indicating the glass forming ability of MGs and can be predicted roughly from the equation $T_g \propto 2.5E$ [201]. This relation demonstrates that T_g is VED-dependent as well.

Table 5.1 Collected data on elastic properties (E, G, B and ν stand respectively for Young's modulus, shear modulus, bulk modulus and Poisson's ratio) and compressive plasticity (ε_p) of BMGs. The compressive plasticity is defined as a portion of the total strain excluding the elastic component. Due to the similarities in test conditions (i.e., sample geometry, aspect ratio and strain rate), their effects on plasticity are minimized.

Alloy	E (GPa)	G (GPa)	B (GPa)	ν	ε_p (%)	Sample geometry, diameter (mm), aspect ratio and strain rate (s^{-1})	Ref.
$Mg_{65}Cu_{25}Y_{10}$	50.1	18.9	48.8	0.329			[233]
$Mg_{65}Cu_{25}Y_9Gd_1$	49.2	19.5	34.3	0.261	0	Rod, Φ2, 2:1	[233]
$Mg_{58.5}Cu_{30.5}Y_{11}$	53.9	20.4	49.4	0.318	0.35	Rod, Φ3, 2:1, 1×10^{-4}	[234]
$Mg_{58}Cu_{27}Zn_5Y_{10}$	55.2	21.3	44.8	0.295	0	Rod, Φ3, 2:1, 1×10^{-4}	[234]
$Mg_{58}Cu_{25}Zn_7Y_{10}$	54.1	20.85	44.57	0.297	0	Rod, Φ3, 2:1, 1×10^{-4}	[234]
$Mg_{75}Cu_{14.5}Zn_{3.5}Y_7$					0.4	Rod, Φ3, 2:1, 1×10^{-4}	[234]
$Mg_{60}Cu_{25}Zn_5Gd_{10}$	54	20.64	46.7	0.307			[234]

$Mg_{65}Cu_{25}Tb_{10}$	51.3	19.6	44.7	0.309	0		[235]
$Mg_{65}Cu_{25}Gd_{10}$	50.6	19.3	45.1	0.313	0		[94]
$Mg_{75}Cu_{15}Gd_{10}$	50				0	Rod, Φ2, 2:1, 5×10^{-4}	[236]
$Mg_{70}Cu_{15}Ni_{5}Gd_{10}$					0.15	Rod, Φ2, 2:1, 5×10^{-4}	[237]
$Mg_{75}Cu_{5}Ni_{10}Gd_{10}$	54				0.2	Rod, Φ2, 2:1, 5×10^{-4}	[237]
$Mg_{65}Cu_{20}Ni_{5}Gd_{10}$					0.15	Rod, Φ2, 2:1, 5×10^{-4}	[237]
$Ca_{48}Mg_{27}Cu_{25}$	29.8	12.1	18.4	0.230	0	Rod, Φ4, 2:1, 1×10^{-4}	[238]
$Ca_{50}Mg_{20}Cu_{30}$	33.2	12.7	29.2	0.311			[239]
$Ca_{65}Mg_{15}Zn_{20}$	26.4	10.1	22.6	0.306			[239]
$Ca_{55}Mg_{18}Zn_{11}Cu_{16}$	31	11.9	26.5	0.305	0	Rod, Φ4, 2:1, 1×10^{-4}	[239, 240]
$Ti_{45}Zr_{20}Be_{35}$	96.8	35.7	111.4	0.36	0.2	Rod, Φ3, 2:1, 1×10^{-4}	[241]
$Ti_{40}Zr_{25}Be_{35}$	99.6	37.2	102.7	0.34			[241]
$Ti_{30}Zr_{35}Be_{35}$	98.5	36.4	111.5	0.35			[241]
$Ti_{50}Ni_{42}Cu_{8}$					0	Rod, Φ2, 2:1, 3×10^{-4}	[242]
$Ti_{39.6}Zr_{9.9}Cu_{35.64}Pd_{13.86}Nb_{1}$					13.9	Rod, Φ2, 2:1, 5×10^{-4}	[243]
$Ti_{38}Zr_{9.5}Cu_{34.2}Pd_{13.3}Nb_{5}$					1.8		[243]
$Zr_{45}Cu_{45}Al_{10}$		35.4	113.3	0.359	0~0.5	2:1, 8×10^{-4}	[244]
$Zr_{47.5}Cu_{47.5}Al_{5}$	88.7	33	113.7	0.365	16.36	Rod, Φ2, 2:1, 8×10^{-4}	[245]
$Zr_{64}Cu_{26}Al_{10}$				0.373	6~7.5	Rod, Φ1.5, 2:1, 1×10^{-4}	[225]
$Zr_{65}Cu_{15}Ni_{10}Al_{10}$	82.96	30.27	106.65	0.355	0.12	Rod, Φ3, 1.5:1, 1×10^{-5}	[224, 246]
$Zr_{62}Cu_{15.5}Ni_{12.5}Al_{10}$	79.65	28.89	109.03	0.378	20	Rod, Φ2, 2:1, 5×10^{-4}	[224]
$Zr_{53}Cu_{20}Ni_{12}Al_{10}Ti_{5}$	87.58	32.12	106.78				[247]
$Zr_{55}Cu_{20}Ni_{10}Al_{10}Ti_{5}$	85	31	118				[248]
$Zr_{57}Cu_{20}Ni_{8}Al_{10}Ti_{5}$	82	30.1	99.2	0.362	1.1	Rod, Φ3, 2:1, 1×10^{-4}	[249]
$Zr_{59}Cu_{20}Ni_{8}Al_{10}Ti_{3}$					0.6	Rod, Φ3, 2:1, 4.5×10^{-5}	[70]
$Zr_{59}Ta_{5}Cu_{18}Ni_{8}Al_{10}$	84.3	30.9	102	0.364	4.5	Rod, Φ3, 2:1, 1×10^{-4}	[249]

$Zr_{57}Nb_5Cu_{15.4}Ni_{12.6}Al_{10}$	87.3	31.98	107.67				[250]
$Hf_{50}Ni_{25}Al_{25}$	125.6	47	127.8	0.336	1.2	Rod, Φ1.5, 2:1, 1×10^{-4}	[225]
$Hf_{53}Ni_{25}Al_{22}$	116.5	43.3	125.3	0.345			[225]
$Hf_{55}Ni_{25}Al_{20}$	117.6	43.7	127.2	0.346	1.5	Rod, Φ1.5, 2:1, 1×10^{-4}	[225]
$Hf_{58}Ni_{25}Al_{17}$	111.7	41.3	125.5	0.351			[225]
$Hf_{60}Ni_{25}Al_{15}$	110.2	40.8	122.8	0.350			[225]
$Hf_{62}Ni_{25}Al_{13}$	111.9	41.3	128.8	0.355	7.3	Rod, Φ1.5, 2:1, 1×10^{-4}	[225]
$Cu_{68}Zr_{32}$	89.6	32	149	0.40			[251]
$Cu_{64}Zr_{36}$	92.0	34	104.3	0.352	0	Rod, Φ2, 2:1, 1×10^{-4}	[252]
$Cu_{50}Zr_{50}$	83.2	30	119.9	0.384	6.58	Rod, Φ2, 2:1, 8×10^{-4}	[245, 252]
$Cu_{46}Zr_{54}$	83.5	30	89	0.392	1.1		[252, 253]
$Cu_{60}Zr_{30}Ti_{10}$	93	33.8	124.6				[254]
$Cu_{60}Zr_{32.5}Ti_{7.5}$	90	32.8	115	0.372	0	Rod, Φ3, 1.5:1, 1×10^{-5}	[246]
$Cu_{54}Zr_{42.5}Al_{3.5}$	81.3	29.2	125.6				[255]
$Cu_{53.2}Zr_{41.8}Al_5$	85.6	30.9	126				[255]
$Cu_{51.5}Zr_{40.5}Al_8$	87.4	31.6	127.2				[255]
$Cu_{50}Zr_{45}Al_5$	84	31	111	0.355	0.9	Rod, Φ3, 1.5:1, 1×10^{-5}	[246]
$Cu_{57.5}Hf_{27.5}Ti_{15}$	103	37.3	117.5				[4]
$Cu_{47}Zr_{11}Ti_{34}Ni_8$					0.2	Rod, Φ3, 1.5:1, 1×10^{-5}	[246]
$Cu_{60}Zr_{20}Hf_{10}Ti_{10}$	101.1	36.93	128.23	0.369	0		[256]
$Pt_{57.5}Cu_{14.7}Ni_{5.3}P_{22.5}$	94.8	33.3	198.7	0.420	20	Bar, 3×3×6, 2:1, 1×10^{-4}	[257]
$Ag_{60}Cu_{40}$	39	12	85				[258]
$Co_{74}Fe_6B_{20}$	175.4	66.4	162	0.32			[259]
$Co_{60}Fe_{20}B_{20}$	174.1	65.7	166	0.325			[259]
$Fe_{60}Co_{20}B_{20}$	172.6	65.1	164	0.325			[259]
$Fe_{40}Co_{40}B_{20}$	174.2	65	182	0.34			[259]

$Fe_{71}Nb_6B_{23}$					1.6	Rod, Φ1, 2:1, 1×10^{-4}	[260]
$Fe_{56.05}Co_{13.45}Nb_{5.5}B_{25}$					0.6	Rod, Φ2, 2:1, 5×10^{-4}	[261]
$Fe_{65}Mo_{14}C_{15}B_6$	195	73	192		0.8	Rod, Φ1.5~2, 2:1, 1×10^{-4}	[262]
$Fe_{66}Mo_{10}P_{12}C_{10}B_2$	176	66.1	176	0.333	1.7	Rod, Φ1.5, 2:1, 1×10^{-4}	[263]
$Fe_{75}Mo_5P_{10}C_{7.5}B_{2.5}$					2.5	Rod, Φ2, 2:1, 4.2×10^{-4}	[264]
$Fe_{63}Cr_3Mo_{12}P_{10}C_7B_5$	183	68.8	179	0.33	0.9		[263]
$Fe_{75.924}Si_{9.5904}B_{8.3916}P_{5.994}Cu_{0.1}$					3.1	Rod, Φ1.5, 2:1, 5×10^{-4}	[265]
$Ni_{60}Nb_{15}Zr_{20}Al_5$					2.5	Rod, Φ2, 2:1, 5×10^{-4}	[266]
$Ni_{45}Ti_{20}Zr_{25}Al_{10}$	109.3	40.2	129.6	0.359	0		[256]
$Ni_{60}Nb_{12.5}Zr_{20}Al_5Ti_{2.5}$					1.8	Rod, Φ2, 2:1, 5×10^{-4}	[266]
$Ni_{60}Nb_{10}Zr_{20}Al_5Ti_5$					0	Rod, Φ2, 2:1, 5×10^{-4}	[266]
$Ni_{40}Ti_{17}Zr_{28}Al_{10}Cu_5$	127.6	47.3	140.7	0.349	0		[256]
$Ni_{62.5}Zr_{20}Nb_{15}Pd_{2.5}$					0.5	Rod, Φ2, 2:1, 5×10^{-4}	[267]
$Ni_{60}Zr_{20}Nb_{15}Pd_5$					2	Rod, Φ2, 2:1, 5×10^{-4}	[267]
$Ni_{52.5}Zr_{20}Nb_{15}Pd_{12.5}$					0.5	Rod, Φ2, 2:1, 5×10^{-4}	[267]
$Ni_{53}Nb_{20}Ti_{10}Zr_8Co_6Cu_3$					0.28	4.8×10^{-4}	[268]
$Pd_{77.5}Cu_6Si_{16.5}$	89.7	31.8	166	0.411	10.4	Rod, Φ3, 1.5:1, 1×10^{-5}	[246]
$Pd_{40}Cu_{40}P_{20}$	93	33.2	158	0.402	2	Rod, Φ2.5, 2:1, 3.3×10^{-5}	[269]
$Pd_{79}Cu_6Si_{10}P_5$					3.5		[270]
$Pd_{42.5}Cu_{30}Ni_{7.5}P_{20}$	101.9	36.5	162.1	0.40	0	Rod, Φ3, 2:1, 5×10^{-4}	[271, 272]
$La_{66}Al_{14}Cu_{10}Ni_{10}$	35.72	13.44	34.91	0.330	0		[273]
$La_{55}Al_{25}Cu_{10}Ni_5Co_5$	41.9	15.6	44.2				[94]
$Ce_{70}Al_{10}Ni_{10}Cu_{10}$	30.3	11.5	27	0.313	0		[273]
$Er_{50}Y_6Al_{24}Co_{20}$	71.1	26.98	65.07	0.318			[274]

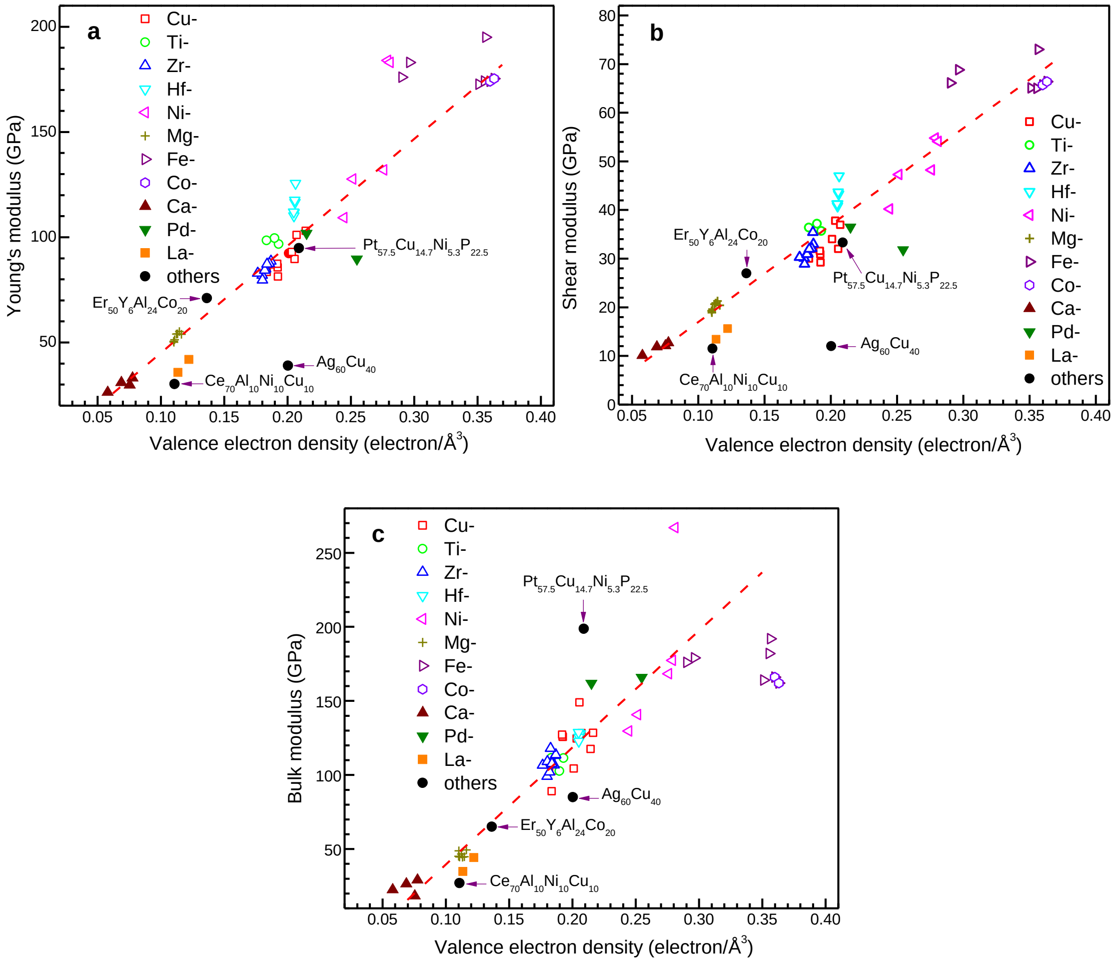

Figure 5.2 Valence electron density dependence of (a) Young's modulus, (b) shear modulus and (c) bulk modulus, respectively for various BMGs. These elastic moduli scale linearly as VED increases. The dashed fitting lines are given as a guide.

5.4 Plasticity of BMGs

The plot of compressive plasticity versus VED is given in Fig. 5.3. Unlike the moduli, the compressive plasticity is a little complicated with respect to VED. Typically MGs, due to the absence of crystalline periodicity, cannot sustain dislocations and thus do not assume macroscopic plasticity. This is evident from the summarized data because in the whole VED range, MGs with little or even no plastic strain can be found. A large number of ductile MGs have so far been developed which can be seen from Fig. 5.3. Interestingly, the compressive plasticity appears to be somewhat VED-dependent; the most plastic MGs such as Zr-, Pt-, Cu-based alloys usually sit within the VED region (0.17, 0.23) included by the two vertical dashed lines, while in the left region MGs such as Mg-, Ca-based alloys present little plasticity and in the right region MGs such as Fe-, Ni-based alloys present limited plasticity. It should be noted that the whole region appears to be separated into two zones: the first one consists of Mg-, Ca-, and RE-based MGs; the second one consists of the rest of MGs. In addition, there seems to remain a statistical trend in Zone 2 that the plasticity increases with decreasing VED. The separation and trend can be more readily distinguished in Fig. 5.4a. A few extra points need to be noted. Firstly, brittle MGs can be observed in the region denoted by the vertical dashed lines in Fig. 5.3, which indicates that there exist other mechanisms (i.e., short-range atomic configurations [253]) besides electronic effect determining the plasticity in MGs. Secondly, addition of non-metallic elements like B, Si, P in Pd-, Fe-based MGs render the plastic behavior more complicated, i.e., those metalloid-containing MGs have plasticity over a more broad VED region, which is possibly due to the change of bonding nature from a more metallic one to a more covalent one [275].

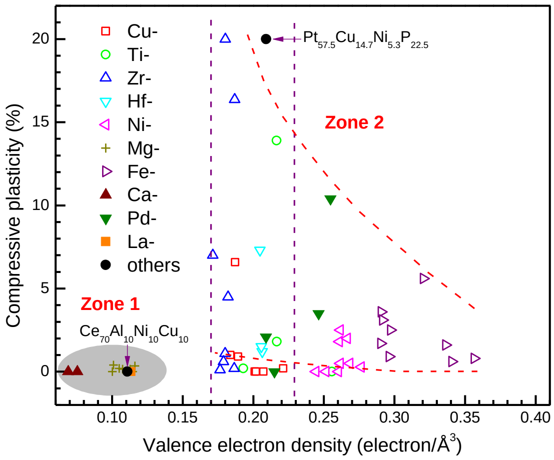

Figure 5.3 The plot of compressive plasticity with respect to VED for various BMGs. Zone 1 consists of Mg-, Ca-, and RE-based MGs; Zone 2 consists of the rest of MGs. In Zone 2, included by the red dashed lines is the statistical trend that plasticity increases as VED decreases.

Careful analysis shows that Ti-, Zr-, and Hf-based systems are among the most compressively plastic MGs, and Cu, Ni are usually the second majority elements in these alloys. Therefore, it may be argued that the occurrence of the maximum plasticity region is not the result of the electron density effect, but just reflects much research effort on these chemically similar alloys. This opinion is not completely true because it does not explain the little plastic deformability in those amorphous alloys beyond the region. Another concern is about the artefacts likely to exist in the data for compressive plasticity. As it is well known, the experimental artefacts are unavoidable but can be minimized to an acceptable range. The sources of artefacts with compression of BMGs involve aspect ratio, sample parallelism, sample tilt, bending load, and so on [276]. To exclude these artificial effects, it is useful to refer to other reliable factors (e.g., Poisson's ratio) representing the plasticity of BMGs and see if these factors are correlated with the VED.

5.5 Poisson's ratio of BMGs

B/*G* or Poisson's ratio (ν) has been considered as a good indicator of plasticity or brittleness [256, 275]. In crystalline alloys, plastic deformation at low temperatures is governed by dislocations which are initiated by critical shear stress proportional to the shear modulus *G*. In contrast, brittle fracture takes place through crack propagation which requires the tensile separation of loosely packed atomic planes. The resistance to the separation is proportional to the bulk modulus *B* [250]. Thus, higher *B*/*G* favors larger plasticity. Poisson's ratio is equivalent to this ratio. These quantities are usually measured with a more reliable method, resonant ultrasound spectroscopy.

The variation of Poisson's ratio as a function of VED is given in Fig. 5.4a. Explicitly the maximum value of ν emerges within an intermediate region, similar to that of plasticity. In addition, two zones can be clearly identified. In Zone 2, from a statistical viewpoint, Poisson's ratio decreases as VED increases, which can be verified by the inset of Fig. 5.4a regarding the correlation between shear modulus and Poisson's ratio. Presented in Fig. 5.4b is the compressive plasticity with respect to Poisson's ratio, showing that they generally have a direct relationship. Besides the statistical trend in Fig. 5.4a, there seems to be a similar trend for each type of MGs (see Figs. 5.4c-e). Poisson's ratios of some chemically similar systems, such as Ti-, Zr-, and Hf-based alloys, are plotted along with respect to VED. It is worth noting that, even in Zone 1 where MGs are commonly macroscopically brittle, the change of Poisson's ratio conforms to the statistical trend, which may imply that MGs in Zone 1 with lower VED should be more microscopically ductile.

In view of these evidences, there arises a question about the connection between VED and plasticity. In the following, a viewpoint is proposed to understand the plasticity of MGs and thus the connection.

5.6 Analysis of plasticity from the viewpoint of energy dissipation

MGs are typically brittle due to the rapid propagation of a single shear band (SB), which is a localized plastic deformation zone [277]. With assistance of thermal softening, SBs are able to travel through the glassy body at an approximate velocity of sound, resulting in the abrupt fracture of MGs [277]. Therefore, the elimination of thermal effect should improve the ductility of BMGs, that is, BMGs yield more plastically if a larger fraction of deformation work applied on the system is converted into other forms of energy rather than heat (to be discussed in the following paragraph). To understand this point, it is necessary to review the mechanism of SB formation.

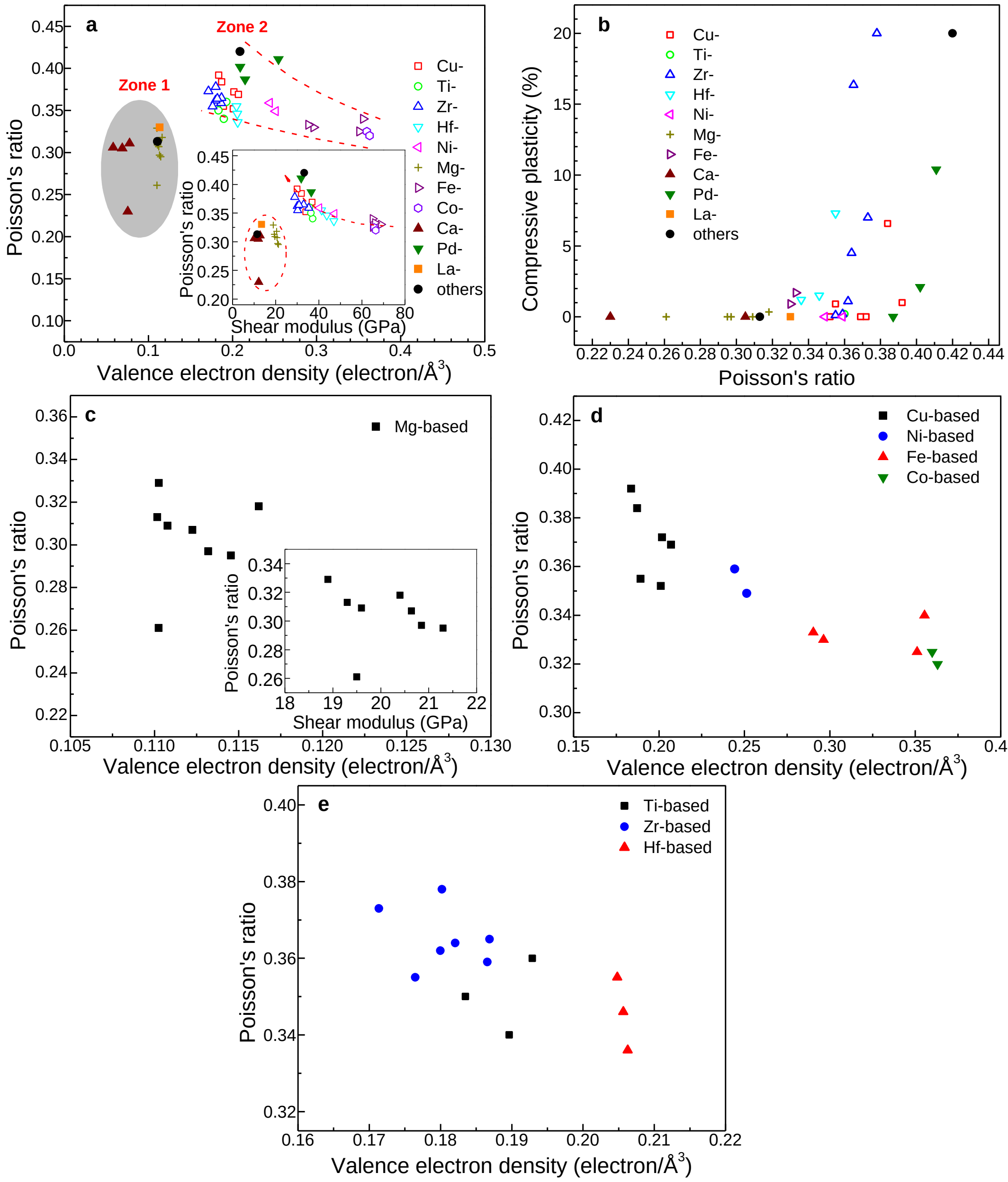

Figure 5.4 (a) Variation of Poisson's ratio as a function of VED, where in Zone 2 the Poisson's ratio generally decreases as the VED increases. Inset: correlation between shear modulus and Poisson's ratio. Two zones can as well be distinguished, supporting the correlation between VED and Poisson's ratio. (b) Compressive plasticity versus Poisson's ratio, showing that they have a correspondence relationship. (c)-(e) VED dependence of Poisson's ratio for each type of MGs, where some chemically similar systems are put together. The inset in Fig. 5.4c shows a further evidence of the correlation for Mg-based MGs.

A single SB generally takes place in order of two processes: nucleation and growth. According to the traditional mechanistic theory, the nucleation of SBs is completed through the collection of small atomic clusters termed shear transformation zones (STZs), which are the underlying structural units carrying the applied shear stress and their cooperative operation leads to the plastic deformation of metallic glasses. STZs are commonly activated at the free-volume sites due to the favorable energetics. As shear strain continues, the cumulative STZs combine into an embryotic SB. In the case that the strain reaches a critical value, the shear band stops nucleating and grows rapidly because the strain rate in the shear banding zone becomes infinite with respect to that in the glass matrix. Following the STZ model, it is evident that BMGs may show much ductility if the deformation work is transformed effectively into the energy creating STZs, exactly, the configurational entropy [222].

Recently, Langer [222] reformulated the amorphous plasticity theory by the effective disorder temperature and entropy flow, in which a term called energy dissipation rate per unit volume is proposed:

$$\vartheta = \frac{\sigma_0 \Omega_m}{k_B \nu_Z}\left(\frac{dS_c}{dt}\right)_{mech} = \frac{\sigma_0 \Omega_Z}{k_B C_f \nu_Z^2}\left(\frac{dS_c}{dt}\right)_{mech} \tag{5.2}$$

where ϑ is the total energy dissipation rate per unit volume, $(dS_c/dt)_{mech}$ is the generation rate for configurational entropy in the form of STZs during mechanical deformation, σ_0 is a factor in the dimensions of stress, k_B is the Boltzmann constant, ν_Z is the number of molecules in an STZ, Ω_m is the volume per molecule, and Ω_Z is the volume of an STZ. $\Omega_Z = C_f \nu_Z \Omega_m$, C_f is a volume correction factor due to the presence of free volume in an STZ and thereby less dense atomic packing in the STZ than in the surrounding area. Thus, the fraction of the total energy dissipated for configurational disorder is expressed as

$$\frac{\vartheta_S}{\vartheta} = \frac{k_B C_f \nu_Z^2}{\sigma_0 \Omega_Z} T_{eff} \tag{5.3}$$

where ϑ_S is the energy dissipation rate for configurational disorder of STZs, T_{eff} is the effective disorder temperature defined as the inverse of the derivative of the configurational entropy with respect to configurational energy.

Langer estimates $\sigma_0 \sim G/\nu_Z$, G as the shear modulus. Hence, Eq. 5.3 is rewritten as

$$\frac{\vartheta_S}{\vartheta} \sim \frac{k_B C_f \nu_Z^3}{G \Omega_Z} T_{eff} \tag{5.4}$$

Obviously, the dissipation fraction for configurational disorder is governed by a few factors—number of constituent molecules, molecular volume, STZ volume, shear modulus, and effective disorder temperature. To understand what this equation says about amorphous plasticity, it is good to revisit some opinions made by Langer [222]. He has argued that the amorphous plasticity is closely related to the molecular rearrangements which are enabled by the STZs as transition states. The STZs are created or annihilated by thermally or mechanically generated fluctuations. Below the glass transition temperature, the molecular rearrangements are largely propelled by the applied mechanical stress. If the STZs exist in a large amount and are oriented randomly, the material can accommodate the external strain in all directions through the shear deformation of STZs, while otherwise the material would become jammed due to the alignment of STZs along the direction of shear stress and no plastic deformation occurs any more. This stress-driven transition between flowing and jammed states could be associated not only with the STZ populations but—more importantly—with their rates of change during deformation which are determined by the generation rate of configurational disorder described in Eq. 5.4. In this equation, T_{eff} characterizes the thermal fluctuations of nonequilibrium systems and might be relevant to glass transition temperature T_g at a low ambient temperature [278]. As glass transition temperature T_g does not vary much in most of MGs, and especially full knowledge of T_{eff} is absent, the effect of T_{eff} will not be considered here. Nonetheless, it is manifest in Eq. 5.4 that the energy dissipation for configurational disorder grows as either ν_Z increases or the product of $G\Omega_Z$ decreases, of which ν_Z may play the more significant role in determining the conversion efficiency because it is a powered term in the equation. It should be noted that the product of $G\Omega_Z$ implies the activation energy for operation of STZs. In what follows, both of effects on plasticity will be discussed separately in some detail.

5.6.1 STZ volume and plasticity

The size of an STZ is measured by either STZ volume or the number of molecules in an STZ; the former one is used in this article if without specifying. Table 5.2 presents the summarized data on the affecting factors mentioned in Eq. 5.4 [67, 94, 108]. It should be noted that the STZ volume and size are different in amount from that in Ref. [67] because the atomic volume in this study is assumed to be that of pure elements and the variation in yield shear strain is taken into consideration. However, it does not influence the propensity of v_Z with composition, and thus the conclusions in Ref. [67] are valid. Shown in Fig. 5.5 is the curve of STZ volume versus VED, where a larger volume normally corresponds to a higher ductility. For example, $Co_{69.5}Fe_{4.5}Cr_1Si_8B_{17}$ with the lowest volume should have the poorest plasticity among those MGs, which is verified by its approximate zero plastic strain. This correspondence relation between STZ volume and ductility was interpreted in Ref. [67] as the result of that lesser number of STZs with a large size are necessary for nucleation of a SB and thus benefit the formation of multiple SBs. Within the framework of energy dissipation, large STZs promote the production rate of configurational disorder and reduce the memory of their prior orientation which improves the capability of holding the shear strain. Although these two opinions may not be exactly the same, they both predict the strengthening of shear capability.

Does the STZ volume help in understanding the relationship between VED and ductility discussed in Section 5.4? In Fig. 5.5, the large values of Ω_Z emerge within the VED region (0.20, 0.24), while beyond that region are small ones. However, there seems to be no specific relationship between VED and STZ volume.

It has to be addressed that whether the STZ volume facilitates the ductility of BMGs is still an open question and therefore the correlation among VED, STZ volume and ductility remains inconclusive.

Table 5.2 Summary of data on factors controlling the dissipation fraction for configurational disorder. T_g, H, G, γ_c, Ω_Z, ν_Z, Φ_0, and W_{0Z} respectively represent glass transition temperature, hardness, shear modulus, yield shear strain, STZ volume, STZ size, the activation energy density and activation energy both at zero stress.

Composition	VED (electron/Å^3)	T_g (K)	H (GPa)	G (GPa)	γ_c[a]	Ω_Z (nm^3)	ν_Z (atom)	Φ_0 (kJ/mol/nm^3)	W_{0Z} (kJ/mol)
$Pd_{40}Ni_{40}P_{20}$	0.238	576	6.58	33.2	0.033	6.57	375	53	348.5
$Pt_{57.5}Cu_{14.7}Ni_{5.3}P_{22.5}$	0.209	508	5.08	33.3	0.0254	10.4	545	31.5	327.8
$Cu_{60}Hf_{25}Ti_{15}$	0.216	740	7.13	37.4	0.0318	4.31	255	55.3	238.5
$Zr_{55}Cu_{25}Ni_{10}Al_{10}$	0.184	630	6.01	31.0	0.0323	3.98	195	47.4	188.8
$Zr_{53.7}Ni_{9.4}Cu_{28.5}Al_{8.4}$	0.186	543	7	33.7	0.0346	1.22	60	59.1	72
$Ni_{53}Nb_{20}Ti_{10}Zr_8Co_6Cu_3$	0.276	846	10.28	52.6[b]	0.0326	2.72	176	81.7	222.3
$Zr_{44}Cu_{44}Al_6Ag_6$	0.186	718	6.27	37.9[b]	0.0276	3.38	175	42.2	142.6
$Co_{69.5}Fe_{4.5}Cr_1Si_8B_{17}$	0.339	589	12.7	65.5	0.0323	0.68	54	100.2	67.7
$Zr_{45}Cu_{49}Al_6$[c]	0.189			35.4	0.041	1.73	100	87	150.5
$Zr_{54}Cu_{38}Al_8$[c]	0.180			32.9	0.041	2.95	160	81.1	239.3

[a] The shear yield strain is calculated from $\gamma_c=\tau_c/G\approx H/6G$.

[b] denotes that the value for shear modulus is calculated from $G=E/2(1+\nu)$, E and ν are respectively the Young's modulus and Poisson's ratio, both of which are available in Ref. [67].

[c] The data such as G and γ_c are derived from the broadband nanoindentaion creep measurements [218, 279].

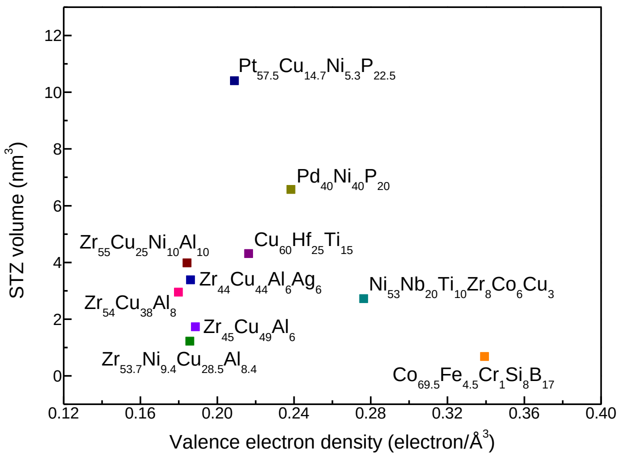

Figure 5.5 VED dependence of the STZ volume.

5.6.2 STZ activation energy and plasticity

Plasticity of BMGs is found in lab-based experiments usually when multiple SBs occur. As discussed above, larger STZ volume could promote the formation of multiple SBs. Besides that, the activation energy or potential energy barrier for an STZ [280] is also recognized to play an important part in the generation of multiple SBs. The activation energy of an STZ can be expressed within the framework of a cooperative shear model (CSM) [94] as

$$W = \frac{8}{\pi^2}\gamma_c^2 \zeta G_{0T}\Omega_Z \quad \text{at } \tau=0 \tag{5.5}$$

and

$$W = 4R\gamma_c^2\left(1-\frac{\tau}{\tau_c}\right)^{3/2} \zeta G_{0T}\Omega_Z \quad \text{at } 0<\tau<\tau_c \tag{5.6}$$

where τ, γ_c and τ_c are respectively the applied stress, the critical yield stress and yield strain. G_{0T} is the shear modulus at zero stress which exhibits a weak dependence on T.

ζ and R are both constants, the former one depending on the strain fluctuation and material properties [281, 282], and the latter one depending on the stress. It is worth noting that Eqs. 5.5 and 5.6 include the term $G_{0T}\Omega_Z$ which firstly emerges in Eq. 5.4 and verify the prior statement that $G\Omega_Z$ matters in activation energy for STZ movement. Later on, without specifying, the activation energy is always equivalent to the one at zero stress.

Small activation energy leads to a low energy barrier for flow initiation and yields more flow regions and shear transformation events globally. The large fraction of these so-called fertile regions benefits the global distribution of plastic strain and increases the possibility of occurrence of multiple SBs [225]. This interpretation is consistent with the prediction of the energy dissipation model where the smaller product of $G\Omega_Z$ denotes the higher efficiency of deformation-to-configurational energy conversion and encourages the generation of configurational disorder. Moreover, lower activation energy makes easier configurational rearrangement and then in-situ nanocrystallization during shear deformation. This shear-induced nanocrystallization has been explored in [283] where nanocrystals are observed to nucleate along the SBs and expected to effectively enhance the strength of shear banding regions so that the rapid propagation of these regions is obstructed. These nanocrystals, when otherwise introduced by pre-quenching or post-annealing processes and distributed all over the amorphous matrix, may also act as a site triggering the multiplication and branching of SBs [245, 284, 285]. Furthermore, atomic-scale structural heterogeneity is regarded to be responsible for large ductility in some MGs [245]. Whether structural inhomogeneity is related to activation energy has so far not been understood. Nevertheless, most of experimental evidence shows indirectly the definite relationship between STZ activation energy and plasticity of BMGs.

It should be added that the tendency for crystallization of MGs can be measured by the activation energy for crystallization, i.e., the smaller activation energy for crystallization indicates the less deformation or thermal energy for amorphous-to-crystal phase transformation. Recent studies have revealed that amorphous alloys with a low activation energy of crystallization exhibit larger ductility than those with a high activation energy of crystallization [284, 286]. Such similar effect on plasticity as that of STZ activation energy may suggest that the two quantities are interrelated. Furthermore, it is reasonable to speculate that the activation energy for glass transition should be correlated to STZ activation energy. To see if there exists a correspondence relation, the activation energies of a number of MGs are given in Table 5.3, some of which were measured by the author and some searched out through the literature. The activation energy for phase transitions such as glass transition (E_g) and crystallization (E_x and E_p are respectively the activation energies at the onset of crystallization and the first crystallization peak) is calculated with the Kissinger method [287]. Assuming that the number of molecules in an STZ is constant and approximately equal to 200 [288], the activation energy for STZ operation is worked out according to Eq. 5.5 where the critical yield strain $\gamma_c \approx 0.027$ and the constant $\zeta \approx 3$. The detailed principles of selecting these parameters comply with up-to-date knowledge of MGs in the articles [94, 288]. Presented in Fig. 5.6 is the STZ activation energy with respect to activation energy for phase transitions. Obviously, the low/high STZ activation energy generally corresponds to the low/high activation energy for both glass transition and crystallization, which justifies our previous assumption and enhances the comprehension of embrittling or plasticizing mechanism by STZ activation energy. The Mg-, Ca-, and RE-based BMGs normally have lower activation energies in comparison to the other BMGs. It is pointed out that the activation energy for phase transitions is larger than the STZ activation energy, which implies that the cooperative movement of STZs could be induced more easily than crystallization. At first sight, this could not make sense because otherwise the STZ events would be anticipated to assemble into a mature SB prior to crystallization, leading to rapid failure of MGs. However, the accompanying heat at the later deformation stage is likely to assist in crystallization.

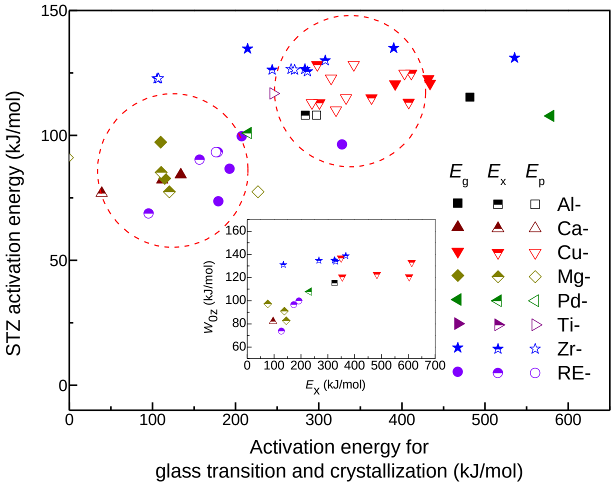

Figure 5.6 Relationship between STZ activation energy and activation energy for phase transformations. Given in the inset picture is the STZ activation energy alongside activation energy for crystallization at the onset point. As a whole, the STZ activation energy scales with the activation energy for crystallization, although, in the area enclosed by the dashed circle, no specific correlation can be observed.

Table 5.3 Summarized data on activation energies of MGs for glass transition (E_g), crystallization (E_x and E_p), and STZ operation (W_{0Z}) at an unsheared state.

Alloy	ρ (g/cm^3)	E_g (kJ/mol)	E_x (kJ/mol)	E_p (kJ/mol)	Ω_m (Å^3)	G (GPa)	W_{0Z} (kJ/mol)	Ref.
$Al_{86.5}Ni_{4.5}Y_9$[a]	3.103	482	326	348.7	18.19	27	115.3	This work
$Mg_{67}Zn_{28}Ca_5$[a]	2.983	114.8	145		20.38	17.3	82.8	This work
$La_{65}Al_{14}(Cu_{5/6}Ag_{1/6})_{11}Ni_5Co_5$[a]	6.120	207.4	193.7	191.4	29.24	14.5	99.6	This work
$Zr_{44}Ti_{11}Cu_{10}Ni_{10}Be_{25}$ (LM1b)	6.059	535.5	134.8	136	16.41	~34	131	This work
$Cu_{46.6}Zr_{53.4}$[b]	7.09	392	354.4	339	17.11	~30	120.6	This work
$Cu_{49.3}Zr_{50.7}$[b]	~7.4	431.8	483.3	415.4	17.41	~30	122.7	This work
$Cu_{53.8}$ $Zr_{46.2}$[b]	6.76	372.7	469.1	389.2	18.79			This work
$Cu_{59.7}Zr_{40.3}$[b]	7.66		612.6	588.6	16.19	~35	133.1	This work
$Mg_{65}Cu_{25}Y_{10}$	3.284		138		20.52	18.9	91.1	[289, 290]
$Mg_{61}Cu_{28}Gd_{11}$	~3.8	110	77	79	21.81	~19	97.3	[291]
$Ca_{65}Mg_{15}Zn_{20}$	2.050	112	97		34.65	10.1	82.2	[181]
$Ca_{55}Mg_{18}Zn_{11}Cu_{16}$	2.411	134			30.15	11.9	84.3	[181]
$Ti_{50}Zr_{10}Be_{40}$	4.13			269	14.74	~36	124.6	[292]
$Ti_{50}Cu_{50}$	6.25		230.6	207				[293]
$Ti_{50}Ni_{30}Cu_{20}$			366.1	406		54.4		[293]
$Ti_{50}Ni_{25}Cu_{25}$				306				[294]
$Ti_{45}Zr_5Ni_{45}Cu_5$			380					[295]
$Zr_{47.5}Cu_{47.5}Al_5$	7.195		330		17.28	33	133.9	[283]
$Zr_{45}Cu_{45}Al_{10}$	7.204		367		16.68	35.4	138.6	[283]
$Zr_{47}Cu_{44}Al_9$	~7.2	390.2	325.1	299.5	16.9	~34	134.9	[296]
$Zr_{61.5}Cu_{13.65}Ni_{14.15}Al_{10.7}$	~6.6	214.56	267.42	305.69	19.11	~30	134.7	[297]
$Cu_{64}Zr_{36}$	8.07	433.7	603		15.13	34	120.8	[298]
$Cu_{50}Zr_{43}Al_7$	~7.5			391.36	16.14	~31	117.5	[299]
$Cu_{60}Hf_{25}Ti_{15}$	9.9			380	15.08	~37	131.1	[300]
$Cu_{60}Zr_{20}Hf_{10}Ti_{10}$	8.315		350	435	15.78	36.93	136.9	[301, 302]
$Pd_{40}Cu_{30}Ni_{10}P_{20}$	~9.2	578.9	231.6		13.3	34.5	107.8	[303]
$La_{62}Al_{14}(Cu_{5/6}Ag_{1/6})_{14}Ni_5Co_5$	6.19	193			28.36	13	86.6	[154]
$La_{55}Al_{25}Ni_{20}$	6.14	328	173.7		25.66	~16	96.4	[303, 304]
$Ce_{60}Al_{10}Ni_{10}Cu_{20}$	~6.7	179.4	128.3		26.11	12	73.6	[305]

[a] The shear moduli for these materials are determined by assuming $G \approx H/6\gamma_c$ and $\gamma_c \approx 0.027$ after measuring the hardness on an MTS Nanoindenter® XP system.

[b] These materials are grown on glass covers in the form of thin films. The amorphous nature was identified by XRD and TEM. The compositions were determined by EDX equipped on JEOL-SEM. Upon measurement of the volume for glass covers and the thickness for both glass covers and thin films, the densities are directly calculated by mass over volume given the uniform distribution of thin films over the area.

Note: The values with a preceding notation (~) are derived from the chemically similar compositions.

5.7 Connection between VED and plasticity

The remaining question is how the above discussion in Section 5.6.2 provides a physical implication on VED-related plasticity of BMGs. As known, the overall crystallization process involves crystal nucleation and subsequent growth, both of which are connected to the thermally activated atomic diffusion events across an energy barrier. The height of the barrier is proportional to the cohesive energy, i.e., the higher the cohesion energy and the higher the energy barrier for atomic diffusion, because the diffusion process requires de-binding and reorganization of atoms. It has been known that the cohesion energy at least in some fcc transition metals is linearly proportional to VED [306] (wherein the total electron density is defined as the probability of finding a particle at some point). Thus, the activation energy for crystallization is thought to exhibit similar dependence on VED. Based on Table 5.3, the activation energies for both glass transition and crystallization as a function of electron density are given in Fig. 5.7, where, for clarity purpose, E_x alongside VED is embedded. This visual observation definitely confirms our expectation that activation energy is VED dependent. In addition, their relationship seems not to be described simply by linear fitting. Further discussion of the accurate relationship goes beyond the ability of this study.

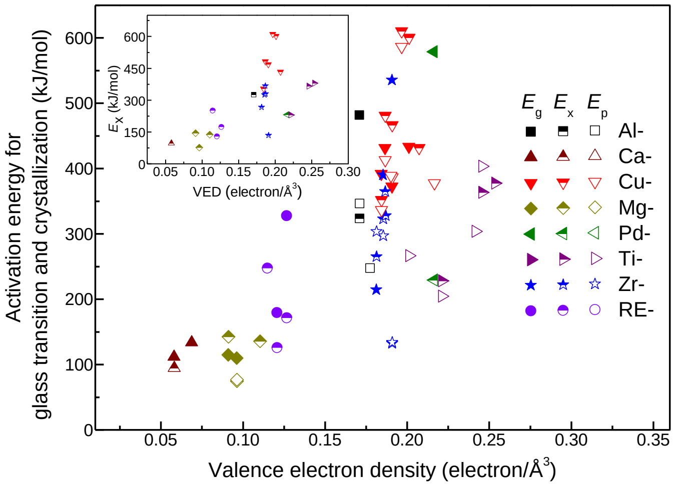

Figure 5.7 Activation energies for phase transformations as a function of VED. The inset picture shows the relationship between E_x and VED.

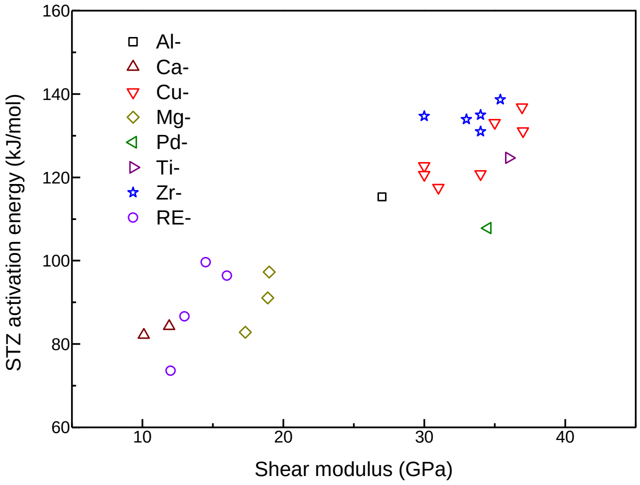

Figure 5.8 Relationship between STZ activation energy and shear modulus, which reconfirms that activation energy is VED dependent since shear modulus is proportional to VED as described in Fig. 5.2b.

Looking at Figs. 5.3 and 5.4a, in Zone 2, MGs on the right side have a high valence electron density and thus high activation energies for crystallization and STZ operation, which does not benefit the generation of configurational disorder or nanocrystallization. As a consequence, limited plasticity or a small Poisson's ratio is usually encountered in these amorphous systems. As the VED decreases into the intermediate region, larger plasticity or Poisson's ratio can take place due to the decreasing activation energies. In

Zone 1, MGs have a low valence electron density and low corresponding activation energies, and are supposed to present good plasticity and large Poisson's ratio; however, compressive tests unambiguously show that Mg-, Ca- and RE-based MGs are typically brittle. Yu *et al* [288] attributed this brittle behavior to the low glass transition temperature and/or low oxidation resistance, while Senkov *et al* [307] suggested that the absence of ductility in Ca-based MGs originates from low Poisson's ratio, dominant covalent bonding nature and low fragility. Despite the extrinsic or intrinsic effects, Poisson's ratio of MGs in Zone 1 is related to activation energy for STZ operation, as that of MGs in Zone 2.

The covalent bonds can as well prevail in some Mg-based MGs by analyzing the data available in [236] (wherein the average radius of the first coordination unit is about 0.25 nm, approaching the covalent bonding lengths of 0.272 nm for Mg-Mg and 0.253 nm for Mg-Cu). When applying the analysis to La-based MGs [154], the same conclusion may not be drawn because the calculated average atomic separation (ranging from ~0.282 to ~0.289 nm) based on the XRD data is notably larger than the covalent bonding distances (0.25 nm for La-La and 0.243 nm for La-Al) but close to the atomic bonding distances (0.276 nm for La-La and 0.281 nm for La-Al). Although the origin of the brittleness in these low-activation-energy MGs, especially in La-based MGs, is not conclusive, the VED effect does exist and provides an easy way in which to find potentially ductile MGs.

Finally, another question remains: is there a relationship between STZ activation energy and STZ volume? This seems to become straightforward in Eqs. 5.5 and 5.6

where the STZ activation energy is linearly proportional to STZ volume. It could lead to a contradictory situation: an amorphous system has a larger STZ volume and as well larger activation energy; the former one may favor the ductility while the latter one does not. Enlightened by the work [275], it is considered that the activation energy density should be the more fundamental quantity governing the ductility.

Presented in Fig. 5.9 is the variation of activation energy density with respect to STZ volume, where the energy density in general reduces as the STZ volume grows, thereby enhancing the propensity of plastic deformation through initiation of STZs [275]. A close look at the figure suggests that MGs, when having STZ volume larger than ~4 nm^3 or activation energy density lower than 60 kJ/mol/nm^3, tend to show more ductility than the inverse others. The STZ volume-energy density diagram proposes a two-parameter criterion distinguishing the ductile MGs from the brittle ones. For example, albeit there are no reported compressive data for $Zr_{45}Cu_{49}Al_6$ and $Zr_{54}Cu_{38}Al_8$, they are both explicitly envisioned to behave in a brittle manner while the latter shows less brittleness due to the relatively large STZ volume and low potential energy density. More recently, structural relaxation effect on the STZ volume of a Zr-based BMG has been systematically investigated [308], where the more brittle behavior was observed in the more relaxed samples. The increasing icosahedra short-range order confirmed by synchrotron X-ray scattering was explained as the mechanism and corresponds to smaller STZ volume and steeper potential energy barrier. In view of these pioneering studies, STZ activation energy (density) and its volume/size are believed to be interdependent.

It may be questioned that the VED-related plasticity cannot be correctly understood from the standpoint of activation energy density because the energy density could be reversely proportional to VED if the activation energy scales with VED. In fact, by sampling a large range of MGs (Table 5.3), it is observed that the activation energy density stays in positive correlation with activation energy although the measured STZ volumes for most MGs are not available, and thus the constant number of molecules in an STZ is assumed.

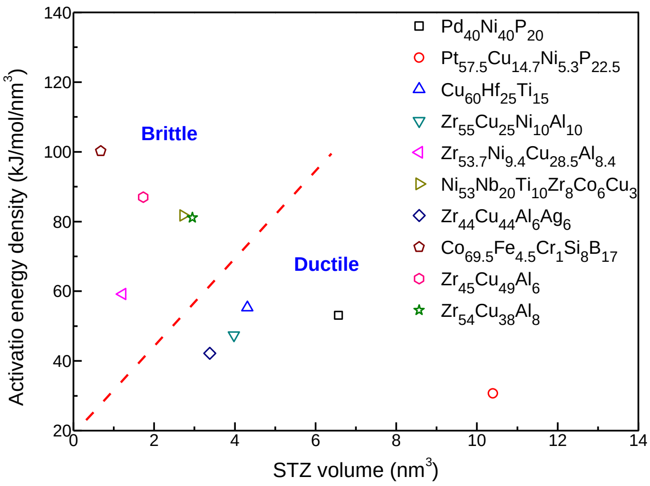

Figure 5.9 STZ volume dependence of STZ activation energy density. It suggests a two-parameter criterion distinguishing the ductile MGs from the brittle MGs.

5.8 Summary

Metallic glasses (MGs) consist of randomly close-packing atoms and do not involve crystalline defects. Their properties are governed by valence electron density (VED) as in conventional crystalline alloys. By thorough search among a large quantity of literature, the VED dependence of their mechanical and thermal properties was verified; these properties are linearly related to VED. More interestingly, the plasticity and Poisson’s ratio of MGs are found dependent on VED as well. The whole VED region can be classified into two zones: Zone 1 is made up of Mg-, Ca-, and RE-based (RE for rare earth) alloys; Zone 2 is made up of the rest of MGs. In either zone, for each type of MGs, Poisson’s ratio commonly decreases as VED increases.

From the energy dissipation viewpoint, the amorphous plasticity is closely related to shear-transformation-zone (STZ) activation energy. The lower STZ activation energy implies the higher ductility because STZs with lower activation energy are able to convert deformation work more efficiently into the configurational energy rather than heat which yields mechanical softening and advances the growth of shear bands. Whether there exists a relationship among STZ volume and thus ductility is still under investigation.

Starting from this model, the VED was found to display an intrinsic correlation with activation energies for both crystallization and STZ operation, i.e., the activation energies ascend with increasing VED. The smaller/larger VED implies the weaker/stronger atomic bonding and then easier/more difficult atomic motion for STZ activation and crystallization. In Zone 2, MGs on the left region have a smaller VED and therefore lower activation energies for both crystallization and STZ movement which are experimentally revealed to promote the ductility and Poisson's ratio. In Zone 1, MGs have the lowest VED but unexpectedly brittleness, which could be attributed either to low glass transition temperature and poor oxidation resistance, or to the dominant covalent bonds especially in Mg- and Ca-based amorphous alloys. Nevertheless, the VED-related plasticity suggests a simple method for designing the ductile MGs.

Chapter 6 Conclusions

Metallic glasses (MGs), also known as amorphous alloys, are a new class of glassy materials which, as the term suggests, consist of random packing atoms and thus do not sustain crystalline defects. The unique structure leads to the unique physical properties, among which the thermal and mechanical properties are most interesting to both material scientists and engineers. As for the thermal properties, MGs are thermodynamically metastable alloys, which exhibit structural relaxation, glass transition and crystallization upon heating. As for the mechanical properties, MGs have the yield strength approaching the theoretical value, large elastic limit (~2%) and very limited plasticity. Due to the lacking of defects, the thermal and mechanical properties are thought to be directly related to the atomic bonding strength. In addition, the microscopic processes in the annealing-induced structural relaxation and mechanical deformation are similar. In view of these facts, the thermal and mechanical properties are expected to be interrelated.

In this project, nine types of MGs have been obtained or prepared in bulk forms by copper mold casting or in thin film forms by magnetron sputtering or in ribbon forms by melt spinning. The thermal and mechanical properties have been investigated in a systematical manner. The relationship between these properties have been established and explained from the viewpoint of valence electron density. Based on these results, the following conclusions can be made:

1. The amorphous structures are verified by experimental and computational

methods. The imaging by transmission electron microscopy (TEM) shows that atoms are randomly packed in glasses, while X-ray diffraction (XRD) and electron diffraction both indicate that there indeed exist short-to-medium-range orders. Molecular dynamics simulation confirms the existence of such order structures, and at the same time suggests that the amorphous structure consists of diverse polyhedral types, among which some types are dominant (e.g., icosahedral and bcc clusters in $Ti_{50}Cu_{50}$). These clusters form a five-fold symmetry in the medium range distance.

2. The thermal properties of MGs are studied by continuous differential scanning calorimetry (DSC). For each glassy alloy, the glass transition temperature, crystallization temperature, and the width of the glass transition region unambiguously exhibit dependence on heating rate, i.e., they increase with an increase in heating rate; in contrast, the heat enthalpy at crystallization appears to be independent of heating rate except for the Zr-based sample. Nevertheless, the larger glass transition temperatures generally correspond to the larger heat enthalpy and the wider glass transition region. Moreover, the relaxation time for glass transition of La- and Zr-based specimens is temperature dependent, which can be well fitted by the Arrhenius-type equation (Vogel–Fulcher–Tamman equation). As these thermal properties are correlated, they can be used to characterize the thermal stability and glass-forming ability of MGs.

3. The instrumented nanoindentation was performed on MGs to characterize the mechanical properties especially at various loading rates and indent sizes. For all

the compositions tested, the load-displacement (*P*-*h*) curves undergo a transition from a more serrated flow at low loading rates to a less serrated flow at high loading rates. For the La- and Zr-based specimens, the pile-up height and the shear band zone size are imaged by atomic force microscopy (AFM) and found to be independent of loading rates, in a good agreement with the absence of loading rate dependence of mechanical properties. However, they both show the indentation size effect (ISE), specifically, the hardness is enhanced at smaller indents, which is well described by the cluster model. In contrast, for $Cu_{49.3}Zr_{50.7}$, the mechanical properties are influenced by the loading rate, i.e., they increase as the loading rate increases from the lowest one up to a critical one. However, it does not have an ISE below the depth of 500 nm. The degree of structural relaxation, which can be represented by the relaxation time spectrum, determines the mechanical response of MGs to the loading rates. This spectrum is derived from the nanoindentation creep, and reveals that the Zr-based specimen is in a more relaxed state than $Cu_{49.3}Zr_{50.7}$ because the former has lower peak intensity than the latter. In other words, the Zr-based specimen is less viscoelastic than $Cu_{49.3}Zr_{50.7}$.

4. The elevated-temperature nanoindentaion on $Cu_{50}Zr_{50}$ reveals the temperature effect on the deformation behaviors. Firstly, the serrated flow becomes more prominent at higher temperatures because the critical strain rate mismatch, between the glass matrix and shear band, is generated at larger strain. Secondly, the mechanical properties such as contact stiffness, hardness and modulus are reduced with increasing temperature. As the nanocrystallization may occur during indentation, the hardness is enhanced with increasing indentation depth. Lastly, the

higher temperature causes the larger creep displacement. However, the temperature and indentation depth both appear not to affect the relaxation times, which is due to the short holding time (60 s) and thus the anelastic recovery with longer relaxation time is not activated.

5. Based on the experimental work of this study, a proportional relationship between the thermal and mechanical properties is identified, which is determined by the valence electron density (VED)—the number of valence electrons per atomic volume. Furthermore, the plasticity and Poisson’s ratio of MGs are found to be dependent on VED as well. The whole VED region can be classified into two zones: Zone 1 is made up of Mg-, Ca-, and RE-based (RE for rare earth) alloys; Zone 2 is made up of the rest of MGs. In either zone, for each type of MGs, Poisson’s ratio commonly decreases as VED increases. From the energy dissipation viewpoint, the amorphous plasticity is closely related to the shear-transformation-zone (STZ) activation energy. The lower STZ activation energy implies the higher ductility because STZs with lower activation energy are able to convert deformation work more efficiently into the configurational energy rather than heat. Using this model, the VED was found to display an intrinsic correlation with activation energies for both crystallization and STZ operation, i.e., the activation energies ascend with increasing VED. The smaller VED implies the weaker atomic bonding and then easier atomic motion for STZ activation and crystallization. Therefore, the VED-related plasticity suggests a simple method for designing the ductile MGs.

Chapter 7 Recommendations for Future Work

The work demonstrated in this thesis has shed some light on the relationship between the thermal and mechanical properties of metallic glasses, which could give indication for the designing of ductile amorphous alloys. Moreover, it could motivate the further studies in the following respects:

1. Isothermal differential scanning experiments of MGs. Although non-isothermal DSC has been carried out to measure the thermal properties of MGs, isothermal DSC is a complementary method in the sense of providing information on crystallization processes: nucleation-to-growth mode or grain growth mode. The clarification of the crystallization processes is important in controlling the microstructure and thus tailoring the mechanical properties of MGs.
2. Indentation size effect (ISE) at small indents. When the indentation depth falls into the range below a few hundred nanometers, the volume of the material probed by Berkovich indenter tip is too small to involve a large number of defects. From this fact, it could be interesting to see if the ISE at small indents can still follow the classical description (e.g., the Nix-Gao model). In addition, unlike Berkovich indentation, spherical indentation is able to identify the load for the initial plastic yielding. Since the defect number may vary with a change of the indentation volume, it deserves further investigation whether the yielding load correlates with the radius of the spherical tip, which can give some indication for the plastic deformation mechanism of MGs.

3. Origin of brittleness for Mg-based MGs, *etc*.. In this study, Mg-, Ca-, and La-based MGs are special in comparison with other MGs because they are totally brittle. The brittleness is attributed to oxidation or covalent bonds. It will be useful to clarify, with experimental and computational methods, the extent to which these intrinsic or extrinsic effects contribute to the brittle behaviors. Therefore, optimization methods can be figured out to improve their mechanical properties, especially the plasticity.

List of Publications

1. **J. J. Pang**, M. J. Tan and K. M. Liew, *On valence electron density, energy dissipation and plasticity of bulk metallic glasses*. (Journal of Alloys and Compounds, 2012)

2. **J. J. Pang**, M. J. Tan, K. M. Liew, and C. Shearwood, *Nanoindentation study of size effect and loading rate effect on mechanical properties of a thin film metallic glass* $Cu_{49.3}Zr_{50.7}$. (Physica B, 2012)

3. **J. J. Pang**, M. J. Tan and K. M. Liew, *Structural evolution of* $Ti_{50}Cu_{50}$ *on rapid cooling by molecular dynamics simulation*. (Applied Physics A, 2012)

4. **J. J. Pang**, Y. C. Liu, and M. J. Tan, *Elevated temperature effect on mechanical behaviors of thin film metallic glass* $Cu_{50}Zr_{50}$ *by nanoindentation*, East Asian Postgraduate Workshop on Nanoscience and Technology, Hong Kong, 2011.

5. **J. J. Pang**, M. J. Tan and K. M. Liew, *Computational study of tensile deformation of a contrained nanoscale metallic glass*, International Journal of Modern Physics B, vol 24, p 305-310, 2010, ICMAT 2009.

6. **J. J. Pang**, M. J. Tan, A. Jarfors and P. D. Chuang, *Glass formation and structural study of* $Ti_{50}Cu_{50}$ *alloy by molecular dynamics*, Materials Science Forum, vol 638-642, p 1665-1670, 2010, THEMEC 2009.

References

[1] W. Buckel, "Electron diffraction diagrams of thin metal films at low temperatures", Zeitschrift fur Physik, 138 (1954) 136.

[2] H.S. Chen, "Glassy metals", Rep Prog Phys, 43 (1980) 353.

[3] A.L. Greer, "Metallic glasses", Science, 267 (1995) 1947.

[4] M. Chen, "Mechanical behavior of metallic glasses: Microscopic understanding of strength and ductility", Annu Rev Mater Res, 38 (2008) 445.

[5] T.L. Hill, An introduction to statistical thermodynamics, Dover Pub., New York, 1986.

[6] A. Revesz, E. Schafler, Z. Kovacs, "Structural anisotropy in a $Zr_{57}Ti_5Cu_{20}Al_{10}Ni_8$ bulk metallic glass deformed by high pressure torsion at room temperature", Appl Phys Lett, 92 (2008) 011910.

[7] R. Tarumi, A. Shibata, H. Ogi, M. Hirao, K. Takashima, Y. Higo, "Elastic anisotropy of an $Fe_{79}Si_{12}B_9$ amorphous alloy thin film studied by ultrasound spectroscopy", J Appl Phys, 101 (2007) 53519.

[8] M.J. Kramer, R.T. Ott, D.J. Sordelet, "Anisotropic atomic structure in a homogeneously deformed metallic glass", J Mater Res, 22 (2007) 382.

[9] X. Hui, H.Z. Fang, G.L. Chen, S.L. Shang, Y. Wang, Z.K. Liu, "Icosahedral ordering in $Zr_{41}Ti_{14}Cu_{12.5}Ni_{10}Be_{22.5}$ bulk metallic glass", Appl Phys Lett, 92 (2008) 201913.

[10] X.D. Wang, S. Yin, Q.P. Cao, J.Z. Jiang, H. Franz, Z.H. Jin, "Atomic structure of binary $Cu_{64.5}Zr_{35.5}$ bulk metallic glass", Appl Phys Lett, 92 (2008) 011902.

[11] W.K. Luo, E. Ma, "EXAFS measurements and reverse Monte Carlo modeling of atomic structure in amorphous $Ni_{80}P_{20}$ alloys", J Non-Cryst Solids, 354 (2008) 945.

[12] G.S. Cargill, F. Spaepen, "Description of chemical ordering in amorphous alloys", J Non-Cryst Solids, 43 (1981) 91.

[13] J. Hafner, "Theory of the formation of metallic glasses", Phys Rev B, 21 (1980) 406.

[14] T. Egami, K. Maeda, V. Vitek, "Structural defects in amorphous solids. A computer simulation study", Philos Mag A, 41 (1980) 883.

[15] T. Egami, D. Srolovitz, "Local structural fluctuations in amorphous and liquid metals: a simple theory of the glass transition", Journal of Physics F (Metal Physics), 12 (1982) 2141.

[16] J.D. Bernal, J. Mason, "Packing of Spheres: Co-ordination of Randomly Packed Spheres", Nature, 188 (1960) 910.

[17] M.H. Cohen, D. Turnbull, "Metastability of amorphous structures", Nature, 203 (1964) 964.

[18] G.S. Cargill, "Dense random packing of hard spheres as a structural model for noncrystalline metallic solids", J Appl Phys, 41 (1970) 2248.

[19] P.K. Leung, J.G. Wright, "Structural investigations of amorphous transition element films: scanning electron diffraction study of Cobalt", Philos Mag, 30 (1974) 185.

[20] J.L. Finney, "Modelling the structures of amorphous metals and alloys", Nature, 266 (1977) 309.

[21] A. Inoue, "Stabilization and high strain-rate superplasticity of metallic supercooled liquid", A267 (1999) 171.

[22] G.S. Cargill Iii, "Structural Investigation of Noncrystalline Nickel-Phosphorus Alloys", J Appl Phys, 41 (1970) 12.

[23] P.H. Gaskell, "A new structural model for transition metal-metalloid glasses", Nature, 276 (1978) 484.

[24] D.B. Miracle, T. Egami, K.M. Flores, K.F. Kelton, "Structural aspects of metallic glasses", MRS Bulletin, 32 (2007) 629.

[25] D.B. Miracle, "A structural model for metallic glasses", Nat Mater, 3 (2004) 697.

[26] D.B. Miracle, "The efficient cluster packing model - An atomic structural model for metallic glasses", Acta Mater, 54 (2006) 4317.

[27] D.B. Miracle, O.N. Senkov, "A geometric model for atomic configurations in amorphous Al alloys", J Non-Cryst Solids, 319 (2003) 174.

[28] H.W. Sheng, W.K. Luo, F.M. Alamgir, J.M. Bai, E. Ma, "Atomic packing and short-to-medium-range order in metallic glasses", Nature, 439 (2006) 419.

[29] A. Inoue, N. Nishiyama, "New bulk metallic glasses for applications as magnetic-sensing, chemical, and structural materials", MRS Bulletin, 32 (2007) 651.

[30] M.H. Cohen, D. Turnbull, "Molecular transport in liquids and glasses", J Chem Phys, 31 (1959) 1164.

[31] M.H. Cohen, D. Turnbull, "Composition requirements for glass formation in metallic and ionic systems", Nature, 189 (1961) 131.

[32] D. Turnbull, M.H. Cohen, "Free-volume model of the amorphous phase: glass transition", J Chem Phys, 34 (1961) 120.

[33] H.A. Davies, B.G. Lewis, "A generalised kinetic approach to metallic glass formation", Scripta Metall, 9 (1975) 1107.

[34] M. Marcus, D. Turnbull, "On the correlation between glass-forming tendency and liquidus temperature in metallic alloys", Mater Sci Eng, 23 (1976) 211.

[35] I.W. Donald, H.A. Davies, "Prediction of glass-forming ability for metallic systems", J Non-Cryst Solids, 30 (1978) 77.

[36] S.H. Whang, "New prediction of glass-forming ability in binary alloys using a temperature-composition map", Mater Sci Eng, 57 (1983) 87.

[37] R.W. Cahn, P. Haasen, E.J. Kramer, Materials Science and Technology, 1991.

[38] J. Langer, "The Mysterious Glass Transition", Phys Today, 60 (2007) 8.

[39] A.S. Argon, H.Y. Kuo, "Plastic flow in a disordered bubble raft (an analog of a metallic glass)", Mater Sci Eng, 39 (1979) 101.

[40] U. Bengtzelius, W. Gotze, A. Sjolander, "Dynamics of supercooled liquids and the glass transition", J Phys C, 17 (1984) 5915.

[41] P.G. Debenedetti, F.H. Stillinger, "Supercooled liquids and the glass transition", Nature, 410 (2001) 259.

[42] W.L. Johnson, M.D. Demetriou, J.S. Harmon, M.L. Lind, K. Samwer, "Rheology and ultrasonic properties of metallic glass- forming liquids: a potential energy landscape perspective", MRS Bulletin, 32 (2007) 644.

[43] S.G. Mayr, "Relaxation kinetics and mechanical stability of metallic glasses and supercooled melts", Phys Rev B, 79 (2009) 060201.

[44] B. Doliwa, A. Heuer, "What Does the Potential Energy Landscape Tell Us

about the Dynamics of Supercooled Liquids and Glasses?", Phys Rev Lett, 91 (2003) 2355011.

[45] N. Mattern, U. Kuhn, J. Eckert, "Structural behavior of amorphous and liquid metallic alloys at elevated temperatures", J Non-Cryst Solids, 353 (2007) 3327.

[46] Y. Zhao, X. Bian, J. Qin, X. Qin, X. Hou, "Structural evolution in the solidification process of Cu-Sn alloys", J Non-Cryst Solids, 353 (2007) 4845.

[47] X.J. Han, H. Teichler, "Liquid-to-glass transition in bulk glass-forming $Cu_{60}Ti_{20}Zr_{20}$ alloy by molecular dynamics simulations", Phys Rev E, 75 (2007) 061501.

[48] Y.Q. Cheng, H.W. Sheng, E. Ma, "Relationship between structure, dynamics, and mechanical properties in metallic glass-forming alloys", Phys Rev B, 78 (2008) 014207.

[49] J.J. Lewandowski, A.L. Greer, "Temperature rise at shear bands in metallic glasses", Nat Mater, 5 (2006) 15.

[50] W.H. Wang, C. Dong, C.H. Shek, "Bulk metallic glasses", Mater Sci Eng R, R44 (2004) 45.

[51] F. Spaepen, "Metallic glasses: Must shear bands be hot?", Nat Mater, 5 (2006) 7.

[52] C.A. Schuh, T.C. Hufnagel, U. Ramamurty, "Mechanical behavior of amorphous alloys", Acta Mater, 55 (2007) 4067.

[53] D. Turnbull, M.H. Cohen, "On free-volume model of liquid-glass transition", J Chem Phys, 52 (1970) 3038.

[54] J.J. Gilman, "Mechanical behavior of metallic glasses", J Appl Phys, 46 (1975) 1625.

[55] F. Spaepen, "A microscopic mechanism for steady state inhomogeneous flow in metallic glasses", Acta Metall, 25 (1977) 407.

[56] A.S. Argon, "Plastic deformation in metallic glasses", Acta Metall, 27 (1979) 47.

[57] M.L. Falk, J.S. Langer, "Dynamics of viscoplastic deformation in amorphous solids", Phys Rev E, 57 (1998) 7192.

[58] F. Delogu, "Molecular dynamics of shear transformation zones in metallic glasses", Intermetallics, 16 (2008) 658.

[59] R. Matsumoto, N. Miyazaki, "The critical length of shear bands in metallic glass", Scripta Mater, 59 (2008) 107.

[60] E.O. Hall, "The deformation and aging of mild steel: 3 Discussion of results", Proc Phys Soc B, 64 (1951) 747.

[61] N.J. Petch, "The cleavage strength of polycrystals", J Iron Steel Inst, 174 (1953) 25.

[62] H. Bei, Z.P. Lu, S. Shim, G. Chen, E.P. George, "Specimen Size Effects on Zr-Based Bulk Metallic Glasses Investigated by Uniaxial Compression and Spherical Nanoindentation", Metall Mater Trans A, 41A (2010) 1735.

[63] Y.J. Huang, J. Shen, J.F. Sun, "Bulk metallic glasses: Smaller is softer", Appl Phys Lett, 90 (2007).

[64] H. Bei, S. Xie, E.P. George, "Softening caused by profuse shear banding in a bulk metallic glass", Phys Rev Lett, 96 (2006).

[65] M.Q. Jiang, W.H. Wang, L.H. Dai, "Prediction of shear-band thickness in metallic glasses", Scripta Mater, 60 (2009) 1004.

[66] Y. Zhang, A.L. Greer, "Thickness of shear bands in metallic glasses", Appl Phys Lett, 89 (2006).

[67] D. Pan, A. Inoue, T. Sakurai, M.W. Chen, "Experimental characterization of shear transformation zones for plastic flow of bulk metallic glasses", Proc Natl Acad Sci U S A, 105 (2008) 14769.

[68] D.C. Jang, C.T. Gross, J.R. Greer, "Effects of size on the strength and deformation mechanism in Zr-based metallic glasses", Int J Plasticity, 27 (2011) 858.

[69] C.A. Volkert, A. Donohue, F. Spaepen, "Effect of sample size on deformation in amorphous metals", J Appl Phys, 103 (2008).

[70] Z.F. Zhang, J. Eckert, L. Schultz, "Difference in compressive and tensile fracture mechanisms of $Zr_{59}Cu_{20}Al_{10}Ni_8Ti_3$ bulk metallic glass", Acta Mater, 51 (2003) 1167.

[71] F.F. Wu, Z.F. Zhang, S.X. Mao, "Size-dependent shear fracture and global tensile plasticity of metallic glasses", Acta Mater, 57 (2009) 257.

[72] H. Guo, P.F. Yan, Y.B. Wang, J. Tan, Z.F. Zhang, M.L. Sui, E. Ma, "Tensile ductility and necking of metallic glass", Nat Mater, 6 (2007) 735.

[73] J.H. Luo, F.F. Wu, J.Y. Huang, J.Q. Wang, S.X. Mao, "Superelongation and Atomic Chain Formation in Nanosized Metallic Glass", Phys Rev Lett, 104 (2010).

[74] E.P.M. Amorim, A.J.R. Da Silva, A. Fazzio, E.Z. Da Silva, "Short linear atomic chains in copper nanowires", Nanotechnology, 18 (2007) 145701.

[75] E.Z. da Silva, A.J.R. da Silva, A. Fazzio, "How do gold nanowires break?", Phys Rev Lett, 87 (2001) 256102.

[76] A.I. Yanson, G.R. Bollinger, H.E. van den Brom, N. Agrait, J.M. van Ruitenbeek, "Formation and manipulation of a metallic wire of single gold atoms", Nature, 395 (1998) 783.

[77] J.J. Pang, M.J. Tan, K.M. Liew, "Computational study of tensile deformation of a constrained nanoscale metallic glass", Int J Mod Phys B, 24 (2010) 305.

[78] F. Delogu, "Molecular dynamics study of size effects in the compression of metallic glass nanowires", Phys Rev B, 79 (2009) 184109 (12 pp.).

[79] G. Kumar, A. Desai, J. Schroers, "Bulk Metallic Glass: The Smaller the Better", Adv Mater, 23 (2011) 461.

[80] F.Q. Yang, K.B. Geng, P.K. Liaw, G.J. Fan, H. Choo, "Deformation in a $Zr_{57}Ti_5Cu_{20}Ni_8Al_{10}$ bulk metallic glass during nanoindentation", Acta Mater, 55 (2007) 321.

[81] N. Li, K.C. Chan, L. Liu, "The indentation size effect in $Pd_{40}Cu_{30}Ni_{10}P_{20}$ bulk metallic glass", J Phys D, 41 (2008) 155415.

[82] R. Sahu, S. Chatterjee, K.L. Sahoo, "Mechanical Properties and Nanocrystallization Behavior of Al-Ni-La Alloys", Metall Mater Trans A, 41A (2010) 861.

[83] H.J. Leamy, H.S. Chen, T.T. Wang, "Plastic flow and fracture of metallic glasses", Metall Trans, 3 (1972) 699.

[84] C.A. Pampillo, "Flow and fracture in amorphous alloys", J Mater Sci, 10 (1975) 1194.

[85] W.J. Wright, R.B. Schwarz, W.D. Nix, "Localized heating during serrated

plastic flow in bulk metallic glasses", Mater Sci Eng A, 319 (2001) 229.

[86] J.J. Kim, Y. Choi, S. Suresh, A.S. Argon, "Nanocrystallization during nanoindentation of a bulk amorphous metal alloy at room temperature", Science, 295 (2002) 654.

[87] K.M. Flores, R.H. Dauskardt, "Local heating associated with crack tip plasticity in Zr-Ti-Ni-Cu-Be bulk amorphous metals", J Mater Res, 14 (1999) 638.

[88] B. Yang, P.K. Liaw, G. Wang, M. Morrison, C.T. Liu, R.A. Buchanan, Y. Yokoyama, "In-situ thermographic observation of mechanical damage in bulk-metallic glasses during fatigue and tensile experiments", Intermetallics, 12 (2004) 1265.

[89] Y.Q. Cheng, Z. Han, Y. Li, E. Ma, "Cold versus hot shear banding in bulk metallic glass", Phys Rev B, 80 (2009).

[90] D.B. Miracle, A. Concustell, Y. Zhang, A.R. Yavari, A.L. Greer, "Shear bands in metallic glasses: Size effects on thermal profiles", Acta Mater, 59 (2011) 2831.

[91] Y.J. Huang, J. Shen, J.F. Sun, Z.F. Zhang, "Enhanced strength and plasticity of a Ti-based metallic glass at cryogenic temperatures", Mater Sci Eng A, 498 (2008) 203.

[92] K.S. Yoon, M. Lee, E. Fleury, J.C. Lee, "Cryogenic temperature plasticity of a bulk amorphous alloy", Acta Mater, 58 (2010) 5295.

[93] A. Kawashima, Y.Q. Zeng, G.Q. Xie, N. Nishiyama, A. Inoue, "Microstructure in a $Ni_{60}Pd_{20}P_{17}B_3$ bulk metallic glass compressively fractured at cryogenic temperature", Mater Sci Eng A, 528 (2010) 391.

[94] W.L. Johnson, K. Samwer, "A universal criterion for plastic yielding of metallic glasses with a $(T/Tg)^{2/3}$ temperature dependence", Phys Rev Lett, 95 (2005) 195501.

[95] B. Yang, J. Wadsworth, T.G. Nieh, "Thermal activation in Au-based bulk metallic glass characterized by high-temperature nanoindentation", Appl Phys Lett, 90 (2007).

[96] C.A. Schuh, A.C. Lund, T.G. Nieh, "New regime of homogeneous flow in the deformation map of metallic glasses: elevated temperature nanoindentation experiments and mechanistic modeling", Acta Mater, 52 (2004) 5879.

[97] D. Klaumunzer, R. Maass, F.H. Dalla Torre, J.F. Loffler, "Temperature-dependent shear band dynamics in a Zr-based bulk metallic glass", Appl Phys Lett, 96 (2010).

[98] Q.S. Zhang, H.F. Zhang, B.Z. Ding, Z.Q. Hu, "Compressive fracture of $Zr_{55}Al_{10}Ni_5Cu_{30}$ bulk amorphous alloy at high temperatures", Mater Sci Eng A, 360 (2003) 280.

[99] L.A. Deibler, J.J. Lewandowski, "Effects of changes in strain rate and test temperature on $Mg_{85}Ca_5Cu_{10}$ metallic glass ribbons", Mater Sci Eng A, 527 (2010) 2214.

[100] M. Weifeng, K. Hongchao, L. Jinshan, C. Hui, Z. Lian, "Effect of strain rate on compressive behavior of Ti-based bulk metallic glass at room temperature", J Alloy Compd, 472 (2009) 214.

[101] F.H. Dalla Torre, A. Dubach, J. Schallibaum, J.F. Loffler, "Shear striations and deformation kinetics in highly deformed Zr-based bulk metallic glasses", Acta Mater, 56 (2008) 4635.

[102] L.F. Liu, L.H. Dai, Y.L. Bai, B.C. Wei, G.S. Yu, "Strain rate-dependent

compressive deformation behavior of Nd-based bulk metallic glass", Intermetallics, 13 (2005) 827.

[103] M.I. Mendelev, R.T. Ott, M. Heggen, M. Feuerebacher, M.J. Kramer, D.J. Sordelet, "Deformation behavior of an amorphous $Cu_{64.5}Zr_{35.5}$ alloy: a combined computer simulation and experimental study", J Appl Phys, 104 (2008) 123532.

[104] Q.-K. Li, M. Li, "Molecular dynamics simulation of intrinsic and extrinsic mechanical properties of amorphous metals", Intermetallics, 14 (2006) 1005.

[105] Z.H. Melgarejo, P.J. Resto, D.S. Stone, O.M. Suarez, "Study of particle-matrix interaction in Al/AlB_2 composite via nanoindentation", Mater Charact, 61 (2010) 135.

[106] J. Sort, J. Fornell, W. Li, S. Surinach, M.D. Baro, "Influence of the loading rate on the indentation response of Ti-based metallic glass", J Mater Res, 24 (2009) 918.

[107] D. Pan, M.W. Chen, "Rate-change instrumented indentation for measuring strain rate sensitivity", J Mater Res, 24 (2009) 1466.

[108] Y. Wu, H.X. Li, G.L. Chen, X.D. Hui, B.Y. Wang, Z.P. Lu, "Nonlinear tensile deformation behavior of small-sized metallic glasses", Scripta Mater, 61 (2009) 564.

[109] F.X. Liu, Y.F. Gao, P.K. Liaw, "Rate-dependent deformation behavior of Zr-based metallic-glass coatings examined by nanoindentation", Metall Mater Trans A, 39 (2008) 1862.

[110] www.metglas.com (accessed July 2008).

[111] www.liquidmetal.com (accessed July 2008).

[112] H. Kakiuchi, A. Inoue, M. Onuki, Y. Takano, T. Yamaguchi, "Application of Zr-based bulk glassy alloys to golf clubs", Mater Trans, 42 (2001) 678.

[113] M. Telford, "The case for bulk metallic glass", Mater Today, 7 (2004) 36.

[114] J. Schroers, B. Lohwongwatana, W.L. Johnson, A. Peker, "Precious bulk metallic glasses for jewelry applications", Mater Sci Eng A, 449-451 (2007) 235.

[115] N. Nishiyama, K. Amiya, A. Inoue, "Recent progress of bulk metallic glasses for strain-sensing devices", Mater Sci Eng A, 449-451 (2007) 79.

[116] J. Schroers, Q. Pham, A. Desai, "Thermoplastic forming of bulk metallic glass-a technology for MEMS and microstructure fabrication", J Microelectromech Syst, 16 (2007) 240.

[117] G. Fiore, L. Battezzati, "Engraving of a $Pd_{77.5}Cu_6Si_{16.5}$ bulk metallic glass", Adv Eng Mater, 9 (2007) 509.

[118] E. Fleury, J. Jayaraj, Y.C. Kim, H.K. Seok, K.Y. Kim, K.B. Kim, "Fe-based amorphous alloys as bipolar plates for PEM fuel cell", J Power Sources, 159 (2006) 34.

[119] M. Ylonen, T. Vaha-Heikkila, H. Kattelus, "Amorphous metal alloy based MEMS for RF applications", Sens Actuator A-Phys, 132 (2006) 283.

[120] N. Kawasegi, N. Morita, S. Yamada, N. Takano, T. Oyama, K. Ashida, J. Taniguchi, I. Miyamoto, S. Momota, H. Ofune, "Rapid nanopatterning of a Zr-based metallic glass surface utilizing focused ion beam induced selective etching", Appl Phys Lett, 89 (2006) 143115.

[121] D. Wang, C. Nordman, J.M. Daughton, Z. Qian, J. Fink, "70% TMR at

room temperature for SDT sandwich junctions with CoFeB as free and reference layers", IEEE Trans Magn, 40 (2004) 2269.

[122] S. Hata, T. Kato, T. Fukushige, A. Shimokohbe, "Integrated conical spring linear actuator", Microelectron Eng, 67-68 (2003) 574.

[123] T. Fukushige, Y. Yokoyama, S. Hata, K. Masu, A. Shimokohbe, "Fabrication and evaluation of an on-chip micro-variable inductor", Microelectron Eng, 67-68 (2003) 582.

[124] H.-W. Jeong, S. Hata, A. Shimokohbe, "Microforming of three-dimensional microstructures from thin-film metallic glass", J Microelectromech Syst, 12 (2003) 42.

[125] L.A. French, Jr., T.B. Pollard, G. Bernhardt, M. Call, L.D. Doucette, M.P. da Cunha, R.J. Lad, J.F. Vetelino, 2002 IEEE Ultrasonics Symposium, IEEE, Munich, Germany, 2002, pp. 127.

[126] M. Lohndorf, M. Lohndorf, T.A. Duenas, A. Ludwig, M.A.R.M. Ruhrig, J.A.W.J. Wecker, D.A.B.D. Burgler, P.A.G.P. Grunberg, E.A.Q.E. Quandt, "Strain sensors based on magnetostrictive GMR/TMR structures", IEEE Trans Magn, 38 (2002) 2826.

[127] S. Hata, K. Sato, A. Shimokohbe, Proceedings of SPIE - The International Society for Optical Engineering, 1999, pp. 97.

[128] C.A. Grimes, D. Kouzoudis, K.G. Ong, R. Crump, "Thin-film magnetoelastic microsensors for remote query biomedical monitoring", Biomed Microdevices, 2 (1999) 51.

[129] S. Ishihara, H. Soejima, S. Komaba, H. Takehisa, M. Shimanuki, W. Xin-min, A. Inoue, "Production of glassy coil springs by warm coiling of Zr-based glassy alloy wires", Mater Trans, 45 (2004) 2788.

[130] A. Basu, A.N. Samant, S.P. Harimkar, J.D. Majumdar, I. Manna, N.B. Dahotre, "Laser surface coating of Fe-Cr-Mo-Y-B-C bulk metallic glass composition on AISI 4140 steel", Surf Coat Technol, 202 (2008) 2623.

[131] A. Kobayashi, S. Yano, H. Kimura, A. Inoue, "Mechanical property of Fe-base metallic glass coating formed by gas tunnel type plasma spraying", Surf Coat Technol, 202 (2008) 2513.

[132] A. Fels, E. Hornbogen, K. Friedrich, "A study of reinforcement by prestressed metallic glass ribbons", J Mater Sci Lett, 3 (1984) 639.

[133] R.U. Vaidya, K.N. Subramanian, "Metallic glass ribbon-reinforced glass-ceramic matrix composites", J Mater Sci, 25 (1990) 3291.

[134] S. Scudino, K. Surreddi, S. Sager, M. Sakaliyska, J. Kim, W. Löser, J. Eckert, "Production and mechanical properties of metallic glass-reinforced Al-based metal matrix composites", J Mater Sci, 43 (2008) 4518.

[135] S. Yoshida, T. Mizushima, T. Hatanai, A. Inoue, "Preparation of new amorphous powder cores using Fe-based glassy alloy", IEEE Trans Magn, 36 (2000) 3424.

[136] A. Inoue, "Bulk glassy and nonequilibrium crystalline alloys by stabilization of supercooled liquid: fabrication, functional properties and applications. Part 2", Proceedings of the Japan Academy, Series B (Physical and Biological Sciences), 81 (2005) 172.

[137] K. Asami, H. Kimura, A. Inoue, "Corrosion resistance of metallic glasses", Funtai Oyobi Fummatsu Yakin/Journal of the Japan Society of Powder and Powder Metallurgy, 54 (2007) 795.

[138] J.J. Oak, A. Inoue, "Formation, mechanical properties and corrosion resistance of Ti-Pd base glassy alloys", J Non-Cryst Solids, 354 (2008) 1828.

[139] B.D. Cunningham, J. Huang, D.G. Baird, "Review of materials and processing methods used in the production of bipolar plates for fuel cells", Int Mater Rev, 52 (2007) 1.

[140] H. Tsuchiya, O. Kobayashi, "Mass production cost of PEM fuel cell by learning curve", Int J Hydrog Energy, 29 (2004) 985.

[141] J. Jayaraj, Y.C. Kim, H.K. Seok, K.B. Kim, E. Fleury, "Development of metallic glasses for bipolar plate application", Mater Sci Eng A, 449-451 (2007) 30.

[142] A. Inoue, T. Shimizu, S.-I. Yamaura, Y. Fujita, S. Takagi, H. Kimura, "Development of glassy alloy separators for a proton exchange membrane fuel cell (PEMFC)", Mater Trans, 46 (2005) 1706.

[143] R.W. Cahn, A.L. Greer, Metastable States of Alloys, in: R.W. Cahn, H. Peter (Eds.) Physical Metallurgy, North-Holland, The Netherlands, 1996.

[144] W.N. Myung, H.G. Kim, T. Masumoto, "Glass transition behaviour of Zr- and Ti-based binary amorphous alloys", Mater Sci Eng A, 179-180 (1994) 252.

[145] X.W. Zhou, H.N.G. Wadley, R.A. Johnson, D.J. Larson, N. Tabat, A. Cerezo, A.K. Petford-Long, G.D.W. Smith, P.H. Clifton, R.L. Martens, T.F. Kelly, "Atomic scale structure of sputtered metal multilayers", Acta Mater, 49 (2001) 4005.

[146] M.S. Daw, M.I. Baskes, "Embedded-atom method: derivation and application to impurities, surfaces, and other defects in metals", Phys Rev B, 29 (1984) 6443.

[147] J.L. Finney, "Random packings and the structure of simple liquids. I. The geometry of random close packing", Proceedings of the Royal Society of London, Series A (Mathematical and Physical Sciences), 319 (1970) 479.

[148] J.L. Finney, "Random packings and the structure of simple liquids. II. The molecular geometry of simple liquids", Proceedings of the Royal Society of London, Series A (Mathematical and Physical Sciences), 319 (1970) 495.

[149] H.P. Klug, L.E. Alexander, X-ray diffraction procedures for polycrystalline and amorphous materials, 2 ed., John Wiley & Sons, New York, 1974, pp. 848.

[150] A. Guinier, X-ray diffraction in crystals, imperfect crystals, and amorphous bodies, Dover Publications, Inc., New York, 1994, pp. 63.

[151] H.W. Yang, J. Gong, R.D. Li, J.Q. Wang, "Thermal variation of electrical resistance of an $Al_{85}Ni_5Y_8Co_2$ metallic glass free of quenched-in nuclei", J Non-Cryst Solids, 355 (2009) 2205.

[152] C.A. Schuh, T.G. Nieh, "A survey of instrumented indentation studies on metallic glasses", J Mater Res, 19 (2004) 46.

[153] E. Matsubara, Y. Waseda, A. Inoue, H. Ohtera, T. Masumoto, "Anomalous X-ray scattering on amorphous $Al_{87}Y_8Ni_5$ and $Al_{90}Y_{10}$ alloys", Z Naturfors Sect A-J Phys Sci, 44 (1989) 814.

[154] Q.K. Jiang, G.Q. Zhang, L. Yang, X.D. Wang, K. Saksl, H. Franz, R. Wunderlich, H. Fecht, J.Z. Jiang, "La-based bulk metallic glasses with critical diameter up to 30 mm", Acta Mater, 55 (2007) 4409.

[155] H.S. Chen, Y. Waseda, "Structure of glassy Zr-Cu and Nb-Ni alloys", Phys Status Solidi A-Appl Res, 51 (1979) 593.

[156] T. Kudo, K. Suzuki, M. Misawa, T. Mizoguchi, N. Watanabe, N. Niimura, "Partial structure factor of amorphous $Cu_{0.57}Zr_{0.43}$ alloy determined

by TOF pulsed neutron diffraction", J Phys Soc Jpn, 45 (1978) 1773.

[157] J.J. Pang, M.J. Tan, K.M. Liew, "Structural evolution of $Ti_{50}Cu_{50}$ on rapid cooling by molecular dynamics simulation", Appl Phys A, 106 (2012) 597.

[158] N.P. Bailey, J. Schitz, K.W. Jacobsen, "Simulation of Cu-Mg metallic glass: thermodynamics and structure", Phys Rev B, 69 (2004) 144205.

[159] A.S. Clarke, H. Jonsson, "Structural changes accompanying densification of random hard-sphere packings", Phys Rev E, 47 (1993) 3975.

[160] X.D. Wang, Q.K. Jiang, Q.P. Cao, J. Bednarcik, H. Franz, J.Z. Jiang, "Atomic structure and glass forming ability of $Cu_{46}Zr_{46}Al_8$ bulk metallic glass", J Appl Phys, 104 (2008) 093519.

[161] X.H. Yi, R.S. Liu, Z.A. Tian, Z.Y. Hou, X.Y. Li, Q.Y. Zhou, "Formation and evolution properties of clusters in liquid metal copper during rapid cooling processes", Trans Nonferr Metal Soc Chi, 18 (2008) 33.

[162] H.Z. Fang, X. Hui, G.L. Chen, R. Ottking, Y.H. Liu, J.A. Schaefer, Z.K. Liu, "Ab initio molecular dynamics simulation for structural transition of Zr during rapid quenching processes", Comput Mater Sci, 43 (2008) 1123.

[163] D. Srolovitz, K. Maeda, S. Takeuchi, T. Egami, V. Vitek, "Local structure and topology of a model amorphous metal", J Phys F, 11 (1981) 2209.

[164] A. Hirata, Y. Hirotsu, T. Ohkubo, E. Matsubara, A. Makino, "Local structure studies of Fe-Nb-B metallic glasses using electron diffraction", J Microsc, 223 (2006) 191.

[165] F.C. Frank, "A discussion on theory of liquids: Supercooling of liquids", Proc R Soc London, Ser A, 215 (1952) 43.

[166] M. Iwamatsu, S.K. Lai, "Lowest-energy structures of 13-atom binary clusters: Do icosahedral clusters exist in binary liquid alloys?", J Non-Cryst Solids, 353 (2007) 3698.

[167] L.V. Meisel, P.J. Cote, "Structure factors in amorphous and disordered harmonic Debye solids", Phys Rev B, 16 (1977) 2978.

[168] S. Sinha, P.L. Srivastava, R.N. Singh, "Temperature-dependent structure and electrical transport in liquid metals", J Phys-Condes Matter, 1 (1989) 1695.

[169] U. Mizutani, N. Akutsu, T. Mizoguchi, "Electronic properties of Cu-Ti metallic glasses", J Phys F, 13 (1983) 2127.

[170] J.J. Pang, M.J. Tan, A. Jarfors, P.D. Chuang, "Glass Formation and Structural Study of $Ti_{50}Cu_{50}$ Alloy by Molecular Dynamics", Mater Sci Forum, 638-642 (2010) 1665.

[171] A. Hirata, Y. Hirotsu, T. Ohkubo, N. Tanaka, T.G. Nieh, "Local atomic structure of Pd-Ni-P bulk metallic glass examined by high-resolution electron microscopy and electron diffraction", Intermetallics, 14 (2006) 903.

[172] V. Yu Kazimirov, D. Louca, M. Widom, X.J. Gu, S.J. Poon, G.J. Shiflet, "Local organization and atomic clustering in multicomponent amorphous steels", Phys Rev B, 78 (2008) 054112.

[173] M.D. Ediger, C.A. Angell, S.R. Nagel, "Supercooled liquids and glasses", J Phys Chem, 100 (1996) 13200.

[174] L.C. Chen, F. Spaepen, "Analysis of calorimetric measurements of grain growth", J Appl Phys, 69 (1991) 679.

[175] D.V. Louzguine, A. Inoue, "Comparison of the long-term thermal stability of

various metallic glasses under continuous heating", Scripta Mater, 47 (2002) 887.

[176] O.N. Senkov, "Correlation between fragility and glass-forming ability of metallic alloys", Phys Rev B, 76 (2007).

[177] E.S. Park, J.H. Na, D.H. Kim, "Correlation between fragility and glass-forming ability/plasticity in metallic glass-forming alloys", Appl Phys Lett, 91 (2007) 31907.

[178] M.Q. Jiang, L.H. Dai, "Intrinsic correlation between fragility and bulk modulus in metallic glasses", Phys Rev B, 76 (2007).

[179] R. Bohmer, K.L. Ngai, C.A. Angell, D.J. Plazek, "Nonexponential relaxations in strong and fragile glass formers", J Chem Phys, 99 (1993) 4201.

[180] D.N. Perera, "Compilation of the fragility parameters for several glass-forming metallic alloys", J Phys-Condes Matter, 11 (1999) 3807.

[181] O.N. Senkov, D.B. Miracle, "Relaxation behavior of Ca-based bulk metallic glasses", Metall Mater Trans A, 41 (2010) 1677.

[182] J.C. Ye, J. Lu, C.T. Liu, Q. Wang, Y. Yang, "Atomistic free-volume zones and inelastic deformation of metallic glasses", Nat Mater, 9 (2010) 619.

[183] C.E. Packard, E.R. Homer, N. Al-Aqeeli, C.A. Schuh, "Cyclic hardening of metallic glasses under Hertzian contacts: Experiments and STZ dynamics simulations", Philos Mag, 90 (2010) 1373.

[184] A. Concustell, J. Sort, A.L. Greer, M.D. Baro, "Anelastic deformation of a $Pd_{40}Cu_{30}Ni_{10}P_{20}$ bulk metallic glass during nanoindentation", Appl Phys Lett, 88 (2006).

[185] N. Li, L. Liu, K.C. Chan, Q. Chen, J. Pan, "Deformation behavior and indentation size effect of $Au_{49}Ag_{5.5}Pd_{2.3}Cu_{26.9}Si_{16.3}$ bulk metallic glass at elevated temperatures", Intermetallics, 17 (2009) 227.

[186] W.C. Oliver, G.M. Pharr, "An Improved technique for determing hardness and elastic-modulus using load and displacement sensing indentation experiments", J Mater Res, 7 (1992) 1564.

[187] Y.C. Liu, J.W.R. Teo, S.K. Tung, K.H. Lam, "High-temperature creep and hardness of eutectic 80Au/20Sn solder", J Alloy Compd, 448 (2008) 340.

[188] A.C. Fischer-Cripps, "A review of analysis methods for sub-micron indentation testing", Vacuum, 58 (2000) 569.

[189] Y.Q. Cheng, E. Ma, "Atomic-level structure and structure-property relationship in metallic glasses", Prog Mater Sci, 56 (2011) 379.

[190] G. Feng, A.H.W. Ngan, "Effects of creep and thermal drift on modulus measurement using depth-sensing indentation", J Mater Res, 17 (2002) 660.

[191] W.H. Jiang, G.J. Fan, F.X. Liu, G.Y. Wang, H. Choo, P.K. Liaw, "Rate dependence of shear banding and serrated flows in a bulk metallic glass", J Mater Res, 21 (2006) 2164.

[192] C.A. Schuh, T.G. Nieh, "A nanoindentation study of serrated flow in bulk metallic glasses", Acta Mater, 51 (2003) 87.

[193] J.I. Jang, B.G. Yoo, J.Y. Kim, "Rate-dependent inhomogeneous-to-homogeneous transition of plastic flows during nanoindentation of bulk metallic glasses: Fact or artifact?", Appl Phys Lett, 90 (2007).

[194] A. Gouldstone, H.J. Koh, K.Y. Zeng, A.E. Giannakopoulos, S. Suresh,

"Discrete and continuous deformation during nanoindentation of thin films", Acta Mater, 48 (2000) 2277.
[195] U. Ramamurty, S. Jana, Y. Kawamura, K. Chattopadhyay, "Hardness and plastic deformation in a bulk metallic glass", Acta Mater, 53 (2005) 705.
[196] T. Burgess, K.J. Laws, M. Ferry, "Effect of loading rate on the serrated flow of a bulk metallic glass during nanoindentation", Acta Mater, 56 (2008) 4829.
[197] R. Saha, W.D. Nix, "Effects of the substrate on the determination of thin film mechanical properties by nanoindentation", Acta Mater, 50 (2002) 23.
[198] A. Castellero, B. Moser, D.I. Uhlenhaut, F.H. Dalla Torre, J.F. Loffler, "Room-temperature creep and structural relaxation of Mg-Cu-Y metallic glasses", Acta Mater, 56 (2008) 3777.
[199] A.H.W. Ngan, B. Tang, "Viscoelastic effects during unloading in depth-sensing indentation", J Mater Res, 17 (2002) 2604.
[200] K.L. Johnson, Contact Mechanics, Cambridge University Press, 1985.
[201] W.H. Wang, "Elastic moduli and behaviors of metallic glasses", J Non-Cryst Solids, 351 (2005) 1481.
[202] H. Li, R.C. Bradt, "Microhardness indentation load/size effect in rutile and cassiterite single crystals", J Mater Sci, 28 (1993) 917.
[203] H. Shi, M. Atkinson, "Friction effect in low-load hardness testing of copper and aluminium", J Mater Sci, 25 (1990) 2111.
[204] W.D. Nix, H.J. Gao, "Indentation size effects in crystalline materials: A law for strain gradient plasticity", J Mech Phys Solids, 46 (1998) 411.
[205] D.C.C. Lam, A.C.M. Chong, "Model and experiments on strain gradient hardening in metallic glass", Mater Sci Eng A, 318 (2001) 313.
[206] H.S. Chou, J.C. Huang, L.W. Chang, T.G. Nieh, "Structural relaxation and nanoindentation response in Zr-Cu-Ti amorphous thin films", Appl Phys Lett, 93 (2008) 191901.
[207] J.C. Lee, K.W. Park, K.H. Kim, E. Fleury, B.J. Lee, M. Wakeda, Y. Shibutani, "Origin of the plasticity in bulk amorphous alloys", J Mater Res, 22 (2007) 3087.
[208] Q.A. Guo, L. Zhang, A.S. Zeiger, Y. Li, K.J. Van Vliet, C.V. Thompson, "Compositional dependence of Young's moduli for amorphous Cu-Zr films measured using combinatorial deposition on microscale cantilever arrays", Scripta Mater, 64 (2011) 41.
[209] Y. Fuqian, G. Kebin, P.K. Liaw, F. Guojiang, H. Choo, "Deformation in a $Zr_{57}Ti_5Cu_{20}Ni_8Al_{10}$ bulk metallic glass during nanoindentation", Acta Materialia, 55 (2007) 321.
[210] W.W. Gerberich, N.I. Tymiak, J.C. Grunlan, M.F. Horstemeyer, M.I. Baskes, "Interpretations of indentation size effects", J Appl Mech-T ASME, 69 (2002) 433.
[211] R. Bhowmick, R. Raghavan, K. Chattopadhyay, U. Ramamurty, "Plastic flow softening in a bulk metallic glass", Acta Mater, 54 (2006) 4221.
[212] T. Burgess, M. Ferry, "Nanoindentation of metallic glasses", Mater Today, 12 (2009) 24.
[213] J. Fornell, E. Rossinyol, S. Surinach, M.D. Baro, W.H. Li, J. Sort, "Enhanced mechanical properties in a Zr-based metallic glass caused by

deformation-induced nanocrystallization", Scripta Mater, 62 (2010) 13.

[214] A. Concustell, J. Sort, G. Alcala, S. Mato, A. Gebert, J. Eckert, M.D. Baro, "Plastic deformation and mechanical softening of $Pd_{40}Cu_{30}Ni_{10}P_{20}$ bulk metallic glass during nanoindentation", J Mater Res, 20 (2005) 2719.

[215] A.I. Taub, F. Spaepen, "Ideal elastic, anelastic and viscoelastic deformation of a metallic glass", J Mater Sci, 16 (1981) 3087.

[216] A. Kursumovic, B. Cantor, "Anelastic crossover and creep recovery spectra in Fe40Ni40B20 metallic glass", Scripta Mater, 34 (1996) 1655.

[217] V. Ocelik, K. Csach, A. Kasardova, V.Z. Bengus, "Anelastic deformation processes in metallic glasses and activation energy spectrum model", Mater Sci Eng A, 226 (1997) 851.

[218] J.B. Puthoff, J.E. Jakes, H. Cao, D.S. Stone, "Investigation of thermally activated deformation in amorphous PMMA and Zr-Cu-Al bulk metallic glasses with broadband nanoindentation creep", J Mater Res, 24 (2009) 1279.

[219] D.S. Stone, J.E. Jakes, J. Puthoff, A.A. Elmustafa, "Analysis of indentation creep", J Mater Res, 25 (2010) 611.

[220] B. Yang, C.T. Liu, T.G. Nieh, "Unified equation for the strength of bulk metallic glasses", Appl Phys Lett, 88 (2006).

[221] T. Egami, D. Srolovitz, "Local structural fluctuations in amorphous and liquid metals: a simple theory of the glass transition", J Phys F, 12 (1982) 2141.

[222] J.S. Langer, "Shear-transformation-zone theory of plastic deformation near the glass transition", Phys Rev E, 77 (2008) 021502.

[223] J.J. Pang, M.J. Tan, K.M. Liew, "On valence electron density, energy dissipation and plasticity of bulk metallic glasses", J Alloy Compd.

[224] Y.H. Liu, G. Wang, R.J. Wang, D.Q. Zhao, M.X. Pan, W.H. Wang, "Super plastic bulk metallic glasses at room temperature", Science, 315 (2007) 1385.

[225] L. Zhang, Y.Q. Cheng, A.J. Cao, J. Xu, E. Ma, "Bulk metallic glasses with large plasticity: Composition design from the structural perspective", Acta Mater, 57 (2009) 1154.

[226] K.W. Park, J. Jang, M. Wakeda, Y. Shibutani, J.C. Lee, "Atomic packing density and its influence on the properties of Cu-Zr amorphous alloys", Scripta Mater, 57 (2007) 805.

[227] J.H. Rose, J. Ferrante, J.R. Smith, "Universal binding energy curves for metals and bimetallic interfaces", Phys Rev Lett, 47 (1981) 675.

[228] A. Banerjea, J.R. Smith, "Origins of the universal binding-energy relation", Phys Rev B, 37 (1988) 6632.

[229] Q. Jiang, B.Q. Chi, J.C. Li, "A valence electron concentration criterion for glass-formation ability of metallic liquids", Appl Phys Lett, 82 (2003) 2984.

[230] F. Riccardo, S. Adriana, Structure of intermetallic compounds and phases, in: R.W. Cahn, P. Haasen (Eds.) Physical metallurgy, North-Holland, The Netherlands, 1996, pp. 350.

[231] I. Bakonyi, "Atomic volumes and local structure of metallic glasses", Acta Mater, 53 (2005) 2509.

[232] J. Gilman, Bulk Modulus, in: J. Gilman (Ed.) Electronic Basis of the Strength of Materials, Cambridge University Press, United Kingdom, 2005, pp. 110.

[233] J.Q. Wang, P. Yu, H.Y. Bai, "Minor addition induced enhancement of strength of Mg-based bulk metallic glass", J Non-Cryst Solids, 354 (2008) 5440.

[234] Z.G. Li, X. Hui, C.M. Zhang, G.L. Chen, "Formation of Mg-Cu-Zn-Y bulk metallic glasses with compressive strength over gigapascal", J Alloy Compd, 454 (2008) 168.

[235] X.K. Xi, R.J. Wang, D.Q. Zhao, M.X. Pan, W.H. Wang, "Glass forming Mg-Cu-RE (RE=Gd, Pr, Nd, Tb, Y, and Dy) alloys with strong oxygen resistance in manufacturability", J Non-Cryst Solids, 344 (2004) 105.

[236] G.Y. Yuan, C.L. Qin, A. Inoue, "Mg-based bulk glassy alloys with high strength above 900 MPa and plastic strain", J Mater Res, 20 (2005) 394.

[237] G.Y. Yuan, K. Amiya, A. Inoue, "Structural relaxation, glass-forming ability and mechanical properties of Mg-Cu-Ni-Gd alloys", J Non-Cryst Solids, 351 (2005) 729.

[238] D. Okai, M. Inoue, T. Mori, T. Fukami, E. Kobayashi, T. Yamasaki, H.M. Kimura, A. Inoue, The 13th International Conference on Rapidly Quenched and Metastable Materials, IOP Publishing Ltd., UK, 2009, pp. 012029.

[239] Z.Y. Zhang, V. Keppens, O.N. Senkov, D.B. Miracle, "Elastic properties of Ca-based bulk metallic glasses studied by resonant ultrasound spectroscopy", Mater Sci Eng A, 471 (2007) 151.

[240] O.N. Senkov, D.B. Miracle, J.M. Scott, "Development and characterization of Ca-Mg-Zn-Cu bulk metallic glasses", Intermetallics, 14 (2006) 1055.

[241] G. Duan, A. Wiest, M.L. Lind, A. Kahl, W.L. Johnson, "Lightweight Ti-based bulk metallic glasses excluding late transition metals", Scripta Mater, 58 (2008) 465.

[242] X.F. Wu, Z.Y. Suo, Y. Si, L.K. Meng, K.Q. Qiu, "Bulk metallic glass formation in a ternary Ti-Cu-Ni alloy system", J Alloy Compd, 452 (2008) 268.

[243] F.X. Qin, X.M. Wang, G.Q. Xie, A. Inoue, "Distinct plastic strain of Ni-free Ti-Zr-Cu-Pd-Nb bulk metallic glasses with potential for biomedical applications", Intermetallics, 16 (2008) 1026.

[244] Y. Peng, H.Y. Bai, "Poisson's ratio and plasticity in CuZrAl bulk metallic glasses", Mater Sci Eng A, 485 (2008) 1.

[245] J. Das, M.B. Tang, K.B. Kim, R. Theissmann, F. Baier, W.H. Wang, J. Eckert, ""work-hardenable" ductile bulk metallic glass", Phys Rev Lett, 94 (2005) 205501.

[246] J.D. Plummer, I.A. Figueroa, R.J. Hand, H.A. Davies, I. Todd, "Elastic properties of some bulk metallic glasses", J Non-Cryst Solids, 355 (2009) 335.

[247] W.H. Wang, "Correlations between elastic moduli and properties in bulk metallic glasses", J Appl Phys, 99 (2006) 93506.

[248] Y. Zhang, D.Q. Zhao, R.J. Wang, W.H. Wang, "Formation and properties of $Zr_{48}Nb_8Cu_{14}Ni_{12}Be_{18}$ bulk metallic glass", Acta Mater, 51 (2003) 1971.

[249] L.Q. Xing, Y. Li, K.T. Ramesh, J. Li, T.C. Hufnagel, "Enhanced plastic strain in Zr-based bulk amorphous alloys", Phys Rev B, 64 (2001) 180201.

[250] J.J. Lewandowski, W.H. Wang, A.L. Greer, "Intrinsic plasticity or brittleness of metallic glasses", Philos Mag Lett, 85 (2005) 77.

[251] L.A. Davis, Y.T. Yeow, P.M. Anderson, "Bulk stiffnesses of metallic glasses", J Appl Phys, 53 (1982) 4834.

[252] G. Duan, K. De Blauwe, M.L. Lind, J.P. Schramm, W.L. Johnson, "Compositional dependence of thermal, elastic, and mechanical properties in Cu-Zr-Ag bulk metallic glasses", Scripta Mater, 58 (2008) 159.

[253] Y.Q. Cheng, A.J. Cao, E. Ma, "Correlation between the elastic modulus and the intrinsic plastic behavior of metallic glasses: the roles of atomic configuration and alloy composition", Acta Mater, 57 (2009) 3253.

[254] R. Tarumi, M. Hirao, T. Ichitsubo, E. Matsubara, J. Saida, H. Kato, "Low-temperature acoustic properties and quasiharmonic analysis for Cu-based bulk metallic glasses", Phys Rev B, 76 (2007) 1.

[255] P. Li, J. Hao, J. Tan, Q. Wang, "The effect of Al on the elastic properties of $(Cu_{0.56}Zr_{0.44})_{100-x}Al_x$ bulk metallic glasses", Mater Sci Eng A, 518 (2009) 16.

[256] Y. Liu, H. Wu, C.T. Liu, Z. Zhang, V. Keppens, "Physical factors controlling the ductility of bulk metallic glasses", Appl Phys Lett, 93 (2008) 151915.

[257] J. Schroers, W.L. Johnson, "Ductile bulk metallic glass", Phys Rev Lett, 93 (2004) 255506.

[258] L. Ju, F. Shimizu, S. Ogata, "Yield point of metallic glass", Acta Mater, 54 (2006) 4293.

[259] C.P. Chou, L.A. Davis, R. Hasegawa, "Elastic constants of Fe(Ni,Co)-B glasses", J Appl Phys, 50 (1979) 3334.

[260] J.H. Yao, J.Q. Wang, Y. Li, "Ductile Fe-Nb-B bulk metallic glass with ultrahigh strength", Appl Phys Lett, 92 (2008) 251906.

[261] Z.Y. Chang, X.M. Huang, L.Y. Chen, M.Y. Ge, Q.K. Jiang, X.P. Nie, J.Z. Jiang, "Catching Fe-based bulk metallic glass with combination of high glass forming ability, ultrahigh strength and good plasticity in Fe-Co-Nb-B system", Mater Sci Eng A, 517 (2009) 246.

[262] X.J. Gu, A.G. McDermott, S.J. Poon, G.J. Shiflet, "Critical Poisson's ratio for plasticity in Fe-Mo-C-B-ln bulk amorphous steel", Appl Phys Lett, 88 (2006) 211905.

[263] X.J. Gu, S.J. Poon, G.J. Shiflet, M. Widom, "Ductility improvement of amorphous steels: roles of shear modulus and electronic structure", Acta Mater, 56 (2008) 88.

[264] F. Liu, Q. Yang, S. Pang, T. Zhang, "Effect of Mo element on the properties of Fe-Mo-P-C-B bulk metallic glasses", J Non-Cryst Solids, 355 (2009) 1444.

[265] A. Makino, L. Xue, K. Yubuta, C. Chuntao, T. Kubota, A. Inoue, "The effect of Cu on the plasticity of Fe-Si-B-P-based bulk metallic glass", Scripta Mater, 60 (2009) 277.

[266] J.B. Qiang, W. Zhang, A. Inoue, "Effects of Al and Ti additions on the thermal stability, glass-forming ability and mechanical properties of $Ni_{60}Nb_{20}Zr_{20}$ glassy alloy", Mater Sci Eng B, 148 (2008) 114.

[267] J.B. Qiang, W. Zhang, A. Inoue, "Formation and compression mechanical properties of Ni-Zr-Nb-Pd bulk metallic glasses", J Mater Res, 23 (2008) 1940.

[268] B. Shen, A. Inoue, A. Takeuchi, "Fabrication, properties and applications of bulk glassy alloys in late transition metal-based systems", Mater Sci Eng A, 441 (2006) 18.

[269] T. Mukai, T.G. Nieh, Y. Kawamura, A. Inoue, K. Higashi, "Effect of strain rate on compressive behavior of a $Pd_{40}Ni_{40}P_{20}$ bulk metallic glass", Intermetallics, 10 (2002) 1071.

[270] L. Li, A. Inoue, Z. Tao, "Formation of bulk Pd-Cu-Si-P glass with good mechanical properties", Mater Trans, 46 (2005) 376.

[271] R. Tarumi, N. Hayama, M. Hirao, Y. Higo, H. Kimura, A. Inoue, "Elastic

properties of Pd-based bulk metallic glasses studied by ultrasouond spectroscopy", Jpn J Appl Phys Part 1-Regul Pap Short Notes Rev Pap, 47 (2008) 3807.
[272] T. Wada, A. Inoue, A.L. Greer, "Mechanical properties of porous bulk glassy alloy prepared in high-pressure hydrogen atmosphere", Mater Sci Eng A, 448-451 (2007) 958.
[273] W.H. Wang, S. Li, R.J. Wang, M.X. Pan, D.Q. Zhao, "Bulk metallic glasses based on heavy rare earth dysprosium", Scripta Mater, 53 (2005) 1489.
[274] W.H. Wang, Y.X. Wei, B. Zhang, R.J. Wang, M.X. Pan, D.Q. Zhao, "Erbium- and cerium-based bulk metallic glasses", Scripta Mater, 54 (2006) 599.
[275] S.J. Poon, A. Zhu, G.J. Shiflet, "Poisson's ratio and intrinsic plasticity of metallic glasses", Appl Phys Lett, 92 (2008) 261902.
[276] W.F. Wu, Y. Li, C.A. Schuh, "Strength, plasticity and brittleness of bulk metallic glasses under compression: statistical and geometric effects", Philos Mag, 88 (2008) 71.
[277] H. Chen, Y. He, G.J. Shiflet, S.J. Poon, "Deformation-induced nanocrystal formation in shear bands of amorphous alloys", Nature, 367 (1994) 541.
[278] T.K. Haxton, A.J. Liu, "Activated dynamics and effective temperature in a steady state sheared glass", Phys Rev Lett, 99 (2007) 195701.
[279] J.B. Puthoff, H.B. Cao, J.E. Jakes, P.M. Voyles, D.S. Stone, MRS Fall Meeting, Materials Research Society, Boston, MA, United states, 2008, pp. 103.
[280] S.G. Mayr, "Activation energy of shear transformation zones: A key for understanding rheology of glasses and liquids", Phys Rev Lett, 97 (2006).
[281] A.S. Argon, L.T. Shi, "Development of visco-plastic deformation in metallic glasses", Acta Metall, 31 (1983) 499.
[282] J.D. Eshelby, "The Determination of the Elastic Field of an Ellipsoidal Inclusion, and Related Problems", Proc R Soc London Ser A, 241 (1957) 376.
[283] G. Kumar, T. Ohkubo, T. Mukai, K. Hono, "Plasticity and microstructure of Zr-Cu-Al bulk metallic glasses", Scripta Mater, 57 (2007) 173.
[284] S.W. Lee, M.Y. Huh, E. Fleury, J.C. Lee, "Crystallization-induced plasticity of Cu-Zr containing bulk amorphous alloys", Acta Mater, 54 (2006) 349.
[285] H. Guo, J. Eckert, W. Loser, L. Schultz, "Novel Ti-base nanostructure-dendrite composite with enhanced plasticity", Nat Mater, 2 (2003) 33.
[286] O.J. Kwon, Y.K. Lee, S.O. Park, J.C. Lee, Y.C. Kim, E. Fleury, "Thermal and mechanical behaviors of Cu-Zr amorphous alloys", Mater Sci Eng A, 448-451 (2007) 169.
[287] H.E. Kissinger, "Variation of peak temperature with heating rate in differential thermal analysis", J Res Natl Bur Stand, 57 (1956) 217.
[288] H.B. Yu, W.H. Wang, H.Y. Bai, Y. Wu, M.W. Chen, "Relating activation of shear transformation zones to beta relaxations in metallic glasses", Phys Rev B, 81 (2010) 220201.
[289] Y.T. Cheng, T.H. Hung, J.C. Huang, J.S.C. Jang, C.Y.A. Tsao, P.Y. Lee, "Effects of partial replacement of Cu and Y by Bin Mg-Cu-Y amorphous alloys", Intermetallics, 14 (2006) 866.
[290] S.V. Madge, A.L. Greer, "Effect of Ag addition on the glass-forming ability and thermal stability of Mg-Cu-Y alloys", Mater Sci Eng A, 375-377 (2004) 759.
[291] Y.D. Sun, Z.Q. Li, J.S. Liu, J.N. Yang, M.Q. Cong, "Crystallization

kinetics of $Mg_{61}Cu_{28}Gd_{11}$ and $(Mg_{61}Cu_{28}Gd_{11})_{99.5}Sb_{0.5}$ bulk metallic glasses", J Alloy Compd, 506 (2010) 302.

[292] L.E. Tanner, R. Ray, "Physical properties of $Ti_{50}Be_{40}Zr_{10}$ glass", Scripta Metall, 11 (1977) 783.

[293] A. Pratap, T.L.S. Rao, K.N. Lad, H.D. Dhurandhar, "Kinetics of crystallization of titanium based binary and ternary amorphous alloys", J Non-Cryst Solids, 353 (2007) 2346.

[294] D.V. Louzguine, A. Inoue, "Crystallization behavior of $Ti_{50}Ni_{25}Cu_{25}$ amorphous alloy", J Mater Sci, 35 (2000) 4159.

[295] X. Guo, D. Louzguine, A. Inoue, "Crystallization kinetics of Ti-Zr-Ni-Cu metallic glasses", Mater Trans, 42 (2001) 2406.

[296] B.Q. Zhang, G.H. Cao, Z.J. Zhan, R.P. Liu, W.K. Wang, "Crystallization kinetics of $Zr_{47}Cu_{44}Al_9$ bulk metallic glass", Trans Mater Heat Treat, 30 (2009) 1.

[297] A.H. Cai, W.K. An, Y. Luo, T.L. Li, X.S. Li, X. Xiong, Y. Liu, "Glass forming ability, non-isothermal crystallization kinetics, and mechanical property of $Zr_{61.5}Al_{10.7}Cu_{13.65}Ni_{14.15}$ metallic glass", J Alloy Compd, 490 (2010) 642.

[298] C.Y. Zhang, K.F. Yao, "Crystallization kinetics of $Cu_{64}Zr_{36}$ amorphous alloys", Rare Metal Mat Eng, 35 (2006) 158.

[299] D.S. Sung, O.J. Kwon, E. Fleury, K.B. Kim, J.C. Lee, D.H. Kim, Y.C. Kim, "Enhancement of the glass forming ability of Cu−Zr−Al alloys by Ag addition", Met Mater Int, 10 (2004) 575.

[300] D.V. Louzguine, A. Inoue, "Evaluation of the thermal stability of a $Cu_{60}Hf_{25}Ti_{15}$ metallic glass", Appl Phys Lett, 81 (2002) 2561.

[301] S.W. Lee, C.M. Lee, J.P. Ahn, Y.C. Kim, J.C. Lee, "A parameter governing the plasticity of Cu-Zr containing bulk metallic glasses", Mater Sci Eng A, 448-451 (2007) 172.

[302] Z.X. Wang, D.Q. Zhao, M.X. Pan, W.H. Wang, T. Okada, W. Utsumi, "Formation and crystallization of CuZrHfTi bulk metallic glass under ambient and high pressures", J Phys Condes. Matter, 15 (2003) 5923.

[303] V.A. Khonik, K. Kitagawa, H. Morii, "On the determination of the crystallization activation energy of metallic glasses", J Appl Phys, 87 (2000) 8440.

[304] Z.P. Lu, Y. Li, C.T. Liu, "Glass-forming tendency of bulk La-Al-Ni-Cu-(Co) metallic glass-forming liquids", J Appl Phys, 93 (2003) 286.

[305] B. Zhang, R.J. Wang, D.Q. Zhao, M.X. Pan, W.H. Wang, "Properties of Ce-based bulk metallic glass-forming alloys", Phys Rev B, 70 (2004) 224208.

[306] Y. Aray, J. Rodriguez, D. Vega, "Topology of the electron density and cohesive energy of the face-centered cubic transition metals", J Phys Chem B, 104 (2000) 4608.

[307] O.N. Senkov, D.B. Miracle, V. Keppens, P.K. Liaw, "Development and characterization of low-density Ca-based bulk metallic glasses: an overview", Metall Mater Trans A, 39 (2008) 1888.

[308] D. Pan, Y. Yokoyama, T. Fujita, Y.H. Liu, S. Kohara, A. Inoue, M.W. Chen, "Correlation between structural relaxation and shear transformation zone volume of a bulk metallic glass", Appl Phys Lett, 95 (2009) 141909.